



THE UNIVERSITY *of* EDINBURGH

This thesis has been submitted in fulfilment of the requirements for a postgraduate degree (e. g. PhD, MPhil, DClinPsychol) at the University of Edinburgh. Please note the following terms and conditions of use:

- This work is protected by copyright and other intellectual property rights, which are retained by the thesis author, unless otherwise stated.
- A copy can be downloaded for personal non-commercial research or study, without prior permission or charge.
- This thesis cannot be reproduced or quoted extensively from without first obtaining permission in writing from the author.
- The content must not be changed in any way or sold commercially in any format or medium without the formal permission of the author.
- When referring to this work, full bibliographic details including the author, title, awarding institution and date of the thesis must be given.

Laser Absorption Spectroscopic Tomography with a Customised Spatial Resolution for Combustion Diagnosis

Rui Zhang



Doctor of Philosophy

THE UNIVERSITY OF EDINBURGH

2023

Abstract

Combustion is a widely used energy conversion technology. However, post-combustion gas emissions have adverse effects on climate change. To address the urgent need for carbon neutrality, efforts are being made to develop cleaner fuels and improve combustion efficiency. Accurate *in situ* measurements of temperature and species concentration are crucial for analysing and diagnosing the combustion process. In industrial applications, probed-based measurement methods are commonly used to detect temperature and species concentration in the combustion, favoured by their simplicity. However, the probe-based techniques are limited in their spatial resolution, as only point-wise measurements can be provided by them. Additionally, their principle often restricts their temporal resolution, which limits their ability to capture the dynamics of the combustion process. To overcome these limitations, researchers are actively working on developing rapid and multi-dimensional *in situ* techniques for temperature and species concentration monitoring.

Laser Absorption Spectroscopy (LAS) has gained significant attention for its non-intrusive nature and fast response in combustion diagnostics. LAS techniques use an emitter-receiver configuration to measure the line-of-sight light intensity absorbed by species in the gaseous medium. By collecting multiple line-of-sight measurements from different angles, LAS enables tomographic measurement of the combustion process. However, implementations of LAS tomography face challenges due to the physical dimensions of the emitter and receiver and the optical access to industrial combustors. These limitations lead to incomplete measurements, which are key factors of ill-posed problems and artefacts in the reconstructed images. The artefacts lead to inaccuracy and unreliability of the diagnostic results.

Increasing physical sampling density is one of the most straightforward ways to alleviate the ill-posed problem caused by inadequate line-of-sight measurements. Improvements in sensors have been demonstrated in previous research, such as optimising laser beam arrangement and reducing the spacing of neighbouring laser beams. In this work, a novel design of a miniature and modular sensor is firstly introduced. It reduces the beam spacing between adjacent laser beams, allowing for

a more precise and detailed reconstruction of temperature and species concentration distributions. Meanwhile, modular design allows for customisation and adaptation to various measurement requirements. This flexibility in deployment reduces the cost of the LAS technique.

The application of small beam spacing in characterising the non-uniformity of the combustion process has also been demonstrated in this thesis. A multi-channel LAS sensor is developed and applied to exhaust measurements of a commercial auxiliary power unit. The results show that the small beam spacing allows a detailed understanding of the exhaust plume at the mixing zone between the exhaust gas and surrounding air. This spatial information can be used to improve the accuracy of temperature and species concentration measurements.

On the other hand, prior knowledge, such as smoothness and sparsity of the measurement target and beam arrangement of the LAS tomographic sensor is used to provide extra physical information to the ill-posed inverse problem. To incorporate the beam arrangement information into the reconstruction process, a new meshing scheme is proposed in this thesis. The scheme dynamically allocates smaller meshes in the beam-dense regions and coarser meshes in the beam-loose regions. This adaptive meshing scheme ensures a finer resolution in detailing the combustion zone where the beams are closely spaced while maintaining the integrity of the physical model by using less resolved reconstruction in the bypass flows or regions where the beams are further apart. As a result, the proposed meshing scheme improves the reconstruction accuracy of the combustion zone.

Overall, this PhD project designed and developed LAS tomographic sensors and methods that enable accurate and fast measurement of gas temperature and species concentration in combustion processes with a customised spatial resolution. The main contributions of this thesis include the design and prototyping of a miniature and modular optical sensor for flexible LAS tomography; the development of a multi-channel LAS sensor for simultaneously monitoring exhaust gas temperature and water vapour concentration in gas turbine engines; and the development of a size-adaptive hybrid meshing scheme to improve the reconstruction of target flow fields.

Lay Summary

Nowadays researchers are developing cleaner fuels and improving their burning efficiency to reduce the harm of post-combustion products on climates. Accurate measurements of the temperature and concentration of these post-combustion products like water vapour and carbon dioxide, are crucial for evaluating the quality of clean fuels and the reliability of the combustor. Inserting probes is a common method used in industry for measuring temperature and concentration due to its simplicity. However, this kind of method only gives slow and point-wise measurements. To overcome those limitations, sensors based on the light principle are used. Laser Absorption Spectroscopy (LAS) is a technique based on measuring the reduction of light intensity when the light beam passes through a region with some gas. LAS has gained attention because the light does not affect the burning process. It also provides accurate and fast measurements. When applying multiple laser beams for measurement across a region, LAS enables a measurement of the distributions of temperature and concentration. The process of retrieving the cross-section image of the flame is called tomography. However, challenges arise due to the physical dimensions of sensors and obstruction by industrial equipment. It is impossible to place enough beams to measure the target, resulting in errors in the reconstructed image.

To improve accuracy in tomographic measurements, one intuitive approach is to maximise the number of beams for measurement. This thesis demonstrates a novel modular design of sensors, which allows flexible sensor arrangement and small spacing of the adjacent beam with 1 cm. To further increase the number of measurements in a small area, a multichannel LAS sensor with 6.3 mm adjacent beam spacing is developed and tested on the exhaust of an aircraft's engine. The results show good accuracy in temperature and concentration measurements. These measurements enhance the understanding of the combustion process of this engine.

Furthermore, information on beam arrangement can be used to improve the quality of tomographic images. A new scheme to smartly mesh the region of measurement is proposed in this thesis. The scheme allocates smaller grids in beam-dense regions and coarser grids in beam-loose regions. It improves the reconstruction accuracy by incorporating the beam arrangement information via different mesh sizes.

Acknowledgements

I would like to express my heartfelt thanks to my supervisor, Dr. Chang Liu, for his invaluable guidance, support, and patience throughout my doctoral journey. Despite his demanding schedule, he consistently made time to give my paper a thorough reading, providing meticulous comments and suggestions. His expertise and supervision have played a pivotal role in shaping my research and academic growth. Special thanks to Dr. Brian Peterson, Dr. Javier Escudero Rodriguez and Prof. Ben Williams for their valuable suggestions on my PhD and viva.

I am also grateful for the valuable guidance and opportunities imparted by Prof. Hugh McCann, which have enriched my understanding of the research field. His belief in the potential of young researchers like myself has instilled confidence and inspired me to pursue excellence in my work.

This thesis owes a debt to my research group. I want to thank Prof. Jingjing Si, Dr. Jinyi Li, Dr. Yong Bao, Dr. Godwin Enemali, Dr. Yuan Chen, Jiangnang Xia, Yalei Fu, and Minqiu Zhou for their continuous support in coding and experimentation.

I feel proud to be involved in the LITECS project and to work with Dr. Michael Lengden, Dr. Ian Armstrong, Dr. Abhishek Upadhyay, Stuart Clark, and Andrew Gough from the University of Strathclyde; Ihab Ahmed from the University of Sheffield, and Dr. Paul Wright from the University of Manchester. The collaborative environment and collective knowledge and expertise have supported me in numerous test campaigns.

Appreciation also goes to my friends in the Agile Tomography group, Dr. Zhou Chen, Dr. Delin Hu, Dr. Hancong Wu, Dr. Zhixi Zhang, Yinghao Li, Zhe Liu, Wei Han and Hao Yu, whose willingness to share their experiences and insights has enriched my research as well as my life. Special thanks go to my good friend Chaonan Lei for her encouragement and continuous urging me to graduate on time.

Lastly, but most importantly, my cordial thanks go to my parents, who love and care for me and whom I love and care about.

求学十载，得良师益友相助，何其幸运。

科学无穷，巧心劳力造器物，乐在其中。

Declaration

I declare that this thesis was composed by myself, that the work contained herein is my own except where explicitly stated otherwise in the text, and that this work has not been submitted for any other degree or professional qualification except as specified.

Rui Zhang

Publication list

Journal Papers

1. **R. Zhang**, J. Xia, I. Ahmed, A. Gough, I. Armstrong, A. Upadhyay, Y. Fu, G. Enemali, M. Lengden, W. Johnstone, P. Wright, K. Ozanyan, M Pourkashanian, H. McCann, C. Liu, "A fast sensor for non-intrusive measurement of concentration and temperature in turbine exhaust," *Sensors and Actuators B: Chemical*, doi: 10.1016/j.snb.2023.134500.
2. **R. Zhang**, J. Si, G. Enemali, Y. Bao, and C. Liu, "Spatially Driven Chemical Species Tomography With Size-Adaptive Hybrid Meshing Scheme," *IEEE Sensors Journal*, vol. 22, 2022
3. G. Enemali, **R. Zhang**, H. McCann and C. Liu, "Cost-Effective Quasi-Parallel Sensing Instrumentation for Industrial Chemical Species Tomography," *IEEE Transactions on Industrial Electronics*, vol. 69, 2022
4. Y. Bao, **R. Zhang**, G. Enemali, Z. Cao, B. Zhou, H. McCann, and C. Liu, "Relative Entropy Regularized TDLAS Tomography for Robust Temperature Imaging," *IEEE Transactions on Instrumentation and Measurement*, vol. 70, 2021
5. Y. Jiang, J. Si, **R. Zhang**, G. Enemali, B. Zhou, H. McCann, and C. Liu, "CST-Net: A Dual-Branch Convolutional Neural Network for Imaging of Reactive Flows Using Chemical Species Tomography," *IEEE Transactions on Neural Networks and Learning Systems*, doi: 10.1109/TNNLS.2022.3157689.
6. J. Xia, G. Enemali, **R. Zhang**, Y. Fu, H. McCann, B. Zhou, and C. Liu, "FPGA-Accelerated Distributed Sensing System for Real-Time Industrial Laser Absorption Spectroscopy Tomography at Kilo-Hertz," *IEEE Transactions on Industrial Informatics*, doi: 10.1109/TII.2023.3292971.
7. A. Upadhyay, M. Lengden, G. Enemali, G. Stewart, W. Johnstone, D. Wilson, G. Humphries, T. Benoy, J. Black, A. Chighine, E. Fisher, **R. Zhang**, C. Liu, N. Polydorides, A. Tsekenis, P. Wright, J. Kliment, J. Nilsson, Y. Feng, V. Archilla, J. Rodríguez-Carmona, J. Sánchez-Valdepeñas, M. Beltran, V. Polo, I. Armstrong, I. Mauchline, D. Walsh, M. Johnson, J. Bauldreay, and H. McCann, "Tomographic imaging of carbon dioxide in the exhaust plume of large commercial aero-engines," *Applied Optics* 61, 8540-8552 (2022)

8. J. Si, G. Li, Y. Cheng, **R. Zhang**, G. Enemali and C. Liu, "Hierarchical Temperature Imaging Using Pseudoinversed Convolutional Neural Network Aided TDLAS Tomography," *IEEE Transactions on Instrumentation and Measurement*, vol. 70, 2021
9. J. Si, G. Fu, Y. Cheng, **R. Zhang**, G. Enemali and C. Liu, "A Quality-Hierarchical Temperature Imaging Network for TDLAS Tomography," *IEEE Transactions on Instrumentation and Measurement*, vol. 71, 2022
10. J. Si, G. Fu, X. Liu, Y. Cheng, **R. Zhang**, J. Xia, Y. Fu, G. Enemali, and C. Liu, "A Spatially Progressive Neural Network for Locally/Globally Prioritized TDLAS Tomography," *IEEE Transactions on Industrial Informatics*, doi: 10.1109/TII.2023.3240733.

Conference Papers

1. **R. Zhang**, J. Xia, H. McCann, I. Ahmed, M. Pourkashanian, A. Gough, I. Armstrong, M. Lengden, W. Johnstone C. Liu, "Miniature Modular Sensor for Chemical Species Tomography with Enhanced Spatial Resolution in Laser Absorption Spectroscopy Tomography," *2023 IEEE International Conference on Imaging Systems and Techniques (IST2023)*, Copenhagen, Denmark, 2023. Submitted.
2. **R. Zhang**, G. Enemali, Y. Fu, H. McCann, I. Armstrong, A. Upadhyay, A. Gough, M. Lendgen, W. Johnstone, I. Ahmed, M. Pourkashanian, C. Liu, "Non-Intrusive Optical Sensor Design for Chemical Species Tomography with Millimetre-Level Spatial Resolution," *7th Field Laser Applications in Industry and Research (FLAIR)*, Aix-les-Bains, France, 2022
3. **R. Zhang**, J. Si, G. Enemali, Y. Bao, and C. Liu, "Chemical Species Tomography with Hybrid Meshing Technique," in *Global 10th World Congress on Industrial Process Tomography (WCIPT)*, Online, 2021.
4. Y. Fu, **R. Zhang**, G. Enemali, A. Upadhyay, M. Lengden and C. Liu, "Convolutional Neural Network Aided Chemical Species Tomography for Dynamic Temperature Imaging," *2022 IEEE International Instrumentation and Measurement Technology Conference (I2MTC)*, Ottawa, Canada, 2022
5. J. Xia, G. Enemali, **R. Zhang** and C. Liu, "Cascade integrator comb filter-aided calibration-free Wavelength Modulation Spectroscopy Tomography," *2022 IEEE International Instrumentation and Measurement Technology Conference (I2MTC)*, Ottawa, Canada, 2022

6. W. Zhang, **R. Zhang**, Y. Fu, G. Enemali, J. Si and C. Liu, "Machine Learning Based Wavelength Modulation Spectroscopy for Rapid Gas Sensing," *2021 IEEE International Instrumentation and Measurement Technology Conference (I2MTC)*, Glasgow, United Kingdom, 2021
7. J. Si, G. Fu, **R. Zhang** and C. Liu, "A quality-hierarchical temperature imaging network for TDLAS tomography," *2021 IEEE International Instrumentation and Measurement Technology Conference (I2MTC)*, Glasgow, United Kingdom, 2021

Contents

Abstract	ii
Lay Summary	iv
Acknowledgements	v
Declaration	vi
Publication list	vii
Journal Papers	vii
Conference Papers	viii
Figures and Tables	xiii
Nomenclature	xvii
1 Introduction	1
1.1 Background and Motivation	1
1.2 Aims and Objectives	3
1.3 Main Contributions	4
1.4 Thesis Outline	5
2 Literature review	7
2.1 Introduction	7
2.2 Beer-Lambert Law	8
2.3 Lineshape Function	9
2.3.1 Gaussian Lineshape Function	9
2.3.2 Lorentzian Lineshape Function	10
2.3.3 Voigt Lineshape Function	11
2.4 Laser Absorption Spectroscopy Techniques	13
2.4.1 Direct Absorption Spectroscopy	13
2.4.2 Wavelength Modulation Spectroscopy	15
2.4.3 Ratio Thermometry	19
2.5 LAS Tomography	22

CONTENTS	xi
2.5.1 Beam Arrangement	23
2.5.2 Ill-posed Inverse Problem of LAS Tomography	27
2.6 Image Reconstruction Algorithms	28
2.6.1 Filtered Back-Projection	29
2.6.2 Iterative Algorithms	30
2.6.3 Regularisation	32
2.6.4 Data Driven Methods	34
2.7 Summary	37
3 Modular LAS Tomographic Sensor	38
3.1 Introduction	38
3.2 Architecture of LAS Tomographic System	39
3.3 Evaluation of the Lab-scale Tomographic System	45
3.3.1 Test Results and Analysis	48
3.4 Modular Sensor Configuration	50
3.4.1 Emitter	50
3.4.2 Receiver	53
3.4.3 Functional Test	55
3.5 128-Channel LAS Tomographic System for Industrial Application . . .	58
3.6 Summary	59
4 A Multi-channel Sensor for Turbine Exhaust Measurement	61
4.1 Introduction	61
4.2 APU	63
4.3 Sensor Design	64
4.3.1 Absorption Line Selection	64
4.3.2 Sensor Configuration	65
4.4 Validation on APU	68
4.4.1 Non-Uniformity Distribution	69
4.4.2 Dynamic Test	73
4.5 Summary	76
5 Size-Adaptive Hybrid Meshing Scheme	77
5.1 Introduction	77
5.2 Size-Adaptive Hybrid Meshing Scheme	79
5.3 Numerical Validation	86
5.3.1 Reconstruction Algorithm	86

CONTENTS	xii
5.3.2 Simulation Setup	87
5.3.3 Metrics for Image Quality Quantification	87
5.3.4 Simulation Results and Discussion	88
5.4 Experimental Validation	91
5.5 Summary	94
6 Conclusion and Future Work	96
6.1 Conclusion	96
6.2 Future Work	98
Appendices	
A Reconstruction of FDS-Simulated Water Vapour	100

Figures and Tables

Figures

2.1	Beer-Lambert law.	8
2.2	Schematic of a typical DAS implementation: (a) Example experiment setup. (b) Baseline fitting of the DAS signal. (C) Laser characterisation.	13
2.3	Typical schematic of WMS measurement.	15
2.4	Schematic of lock-in signal process.	17
2.5	Laser characterisation of TDL's WMS output.	18
2.6	Demonstration of fitting the CF-WMS- $2f/1f$ to extract path-integrated absorption.	20
2.7	Demonstration of two linestrengths with different temperature dependency and resulting ratio.	21
2.8	Geometric description of a line-of-sight measurement in LAS tomography.	22
2.9	Illustration of the central slice theorem and the FBP algorithm. The left panel defines the Radon transform and the right panel shows the sinogram in the Fourier space.	29
3.1	Block diagram of LAS tomographic system.	39
3.2	32-channel lab-scale LAS tomographic system prototype.	40
3.3	Breakdown view of the emitter.	42
3.4	Circuit diagram of TIA.	43
3.5	Breakdown view of the receiver.	44
3.6	Example of PD's sensitivity to light intensity.	47
3.7	PD's characteristics adopted from data sheet.	48
3.8	Experimental reconstruction of the 2D H ₂ O distributions with two experimental phantoms on the left and the reconstructed distributions on the right.	49
3.9	Diagram of the (a) emitter, (b) receiver and (c) laser path.	51
3.10	Diagram of C lens used for collimation.	52
3.11	Spot size validation for two C lenses from the same batch. (a) Spot size at different working distances (b) Combine beams at 80 cm with 4 mm diameter lens dictator.	53

3.12	Simulation bandwidth with gains at 500, 1k, 2k, 3k, 4k and 5k, respectively.	54
3.13	PCB layout of the TIA in modular receiver.	54
3.14	Example test setup and the three prototypes for testing.	55
3.15	Allan deviation analysis at 1 atm and room temperature. The red line proportional to $\sqrt{\tau}$ indicates the theoretically expected behaviour of the system dominated by white noise.	57
3.16	128-channel LAS tomographic sensor with octagon shape frame.	58
3.17	Example beam arrangement with large beam count.	58
4.1	Honeywell 131-9A in service with Airbus A320.	63
4.2	Absorbance spectra at 21°C and 400°C for the selected H ₂ O lines assuming $L = 50$ cm, $\chi = 5\%$ and $P = 1$ atm.	64
4.3	Schematic diagram of the developed 8-channel system.	65
4.4	Optical layout of (a) a single-beam measurement and (b) 7 laser beams located at the plume edge.	66
4.5	<i>In situ</i> experimental system. (a) and (b) show the picture and the schematic layout of the APU and the sensor.	68
4.6	Non-uniformity characterisation at APU plume edge using scanned extractive gas sampling and TC.	69
4.7	Point-wise measurement of temperature and H ₂ O concentration along the scan and their LAS-equivalent values under steady full-load conditions. The equivalent values for the whole plume path length are calculated via HITRAN.	70
4.8	Beam layout of the multi-channel sensor at the APU exit.	70
4.9	left: $WMS-2f/1f$ obtained for each of the 7 beams at the plume edge. Right: the comparison between the non-uniform profile retrieved using the LAS sensor and benchmarks.	71
4.10	Comparison of dynamic H ₂ O and EGT obtained using the developed sensor and the TC under varying turbine speed for a 120-second APU experiment.	73
4.11	Dynamically sampled H ₂ O and EGT using the developed sensor under different APU operating conditions, i.e., (a) transient states for ignition and acceleration; (b) The transition period from no-load to the full-load steady-state condition.	74

5.1	Flow chart of the proposed 5-step size-adaptive hybrid meshing scheme. (a) Sensing region and beam arrangement; (b) process of N_m determination; (c) demonstration of the edge spread function; (d) meshing with given d_{in} ; (e) finally discretised hybrid-size meshes.	80
5.2	An example 128-way LAS tomographic sensor with RoI in the beam-dense region.	82
5.3	Discretised RoS with (a) hybrid-size meshes and (b) uniform-size meshes.	84
5.4	Comparison between the singular values of the sensing matrices obtained using the hybrid-size meshing scheme with 628 pixels and the uniform-size meshing scheme with 592 pixels.	86
5.5	Simulated phantoms of 2D distributions of H_2O concentration with (a) one homogeneity (b) three homogeneities, respectively.	88
5.6	Dependence of IE on ε in the RoI for the uniform-size and hybrid-size meshing schemes.	89
5.7	Reconstructions of the phantoms in Figure 5.5 using (a, b) the proposed size-adaptive hybrid meshing scheme and (c, d) uniform-size meshing scheme.	90
5.8	Comparison of (a) IE in RoI (b) DLC (c) CVE with uniform-size and hybrid-size meshing schemes at different measurement SNRs.	90
5.9	Reconstruction of (a, d) two experimental H_2O phantoms simulated via FDS using the (b, e) hybrid-size and (c, f) uniform-size meshing schemes.	92
A.1	Snapshots for Media 1.	101
A.2	Snapshots for Media 2.	102

Tables

2.1	Summary of notable systems of LAS tomography for combustion analysis.	26
2.2	Summary and comparison between algorithms used for LAS tomography.	36
3.1	Bandwidth of components in example LAS tomographic system.	46
3.2	Compare the test results of temperature and H_2O concentration from Three sensor prototypes with humanity sensor.	56

4.1	Spectral parameters of the selected H ₂ O lines at $T = 400^{\circ}\text{C}$, $P = 1$ atm (HITRAN database).	64
4.2	Laser driving parameters of the three DFBs used in the sensor.	67
4.3	<i>In situ</i> measured H ₂ O and EGT at the APU full-load condition.	73
5.1	η_{sector} values in the 38 selected sectors.	83
5.2	Simulation parameters of the two phantoms in Figure 5.6.	87
5.3	Simulation parameters of the two scenarios.	93
5.4	Quantitative comparison between the hybrid-size and uniform-size meshing schemes for two scenarios.	93

Nomenclature

Acronyms

ADC	Analogue-to-Digital Converter
APU	Auxiliary Power Unit
ART	Algebraic Reconstruction Technique
CF-WMS	Calibration-Free Wavelength Modulation Spectroscopy
CFD	Computational Flow Dynamics
CNN	Convolutional Neural Network
CVE	Centroid Value Error
DAS	Direct Absorption Spectroscopy
DFB	DistriButed-feedback
DL	Dictionary Learning
DLC	DisLoCation
DNS	Direct Numerical Simulation
ECU	Engine Control Unit
EGT	Exhaust Gas Temperature
ELM	Extreme Learning Machine
ESF	Edge Spread Function
FBP	Filtered Back-Projection
FDM	Frequency Division Multiplexing
FDS	Fire Dynamic Simulator
FM	Frequency Modulation
FSR	Free Spectral Range
FTIR	Fourier-Transform Infrared Spectroscopy
FWHM	Full Width at Half Maximum
GTE	Gas Turbine Engine
HWHM	Half-Width at Half Maximum
IE	Image Error
IM	Intensity Modulation
LAS	Laser Absorption Spectroscopy

LES	Large Eddy Simulation
LPF	Low Pass Filter
LSTM	Long Short-term Memory
PD	PhotoDiode
PINN	Physical Informed Neural Network
PNR	Point of No Return
RETRO	Relative Entropy Tomographic RecOnstruction
RoI	Region of Interest
RoS	Region of Sensing
RP	Red Pitaya
SAF	Sustainable Aviation Fuel
SC	Signal Condition board
SNR	Signal-to-Noise Ratio
STD	Standard Deviation
SVD	Singular Value Decomposition
TC	ThermoCouple
TDFA	Thulium-Doped Fibre Amplifier
TDL	Tunable Diode Laser
TIA	TransImpedance Amplifier
TV	Total Variation
WMS	Wavelength Modulation Spectroscopy

Symbols

χ	Mole fraction of species/concentration of species
ν	laser wavenumber
Φ	Lineshape function
A	Absorbance
B	Path-integrated absorption
c	Speed of light
e	Natural constant
E''	Lower-state energy
h	Planck constant
k	Boltzmann's constant

L	Optical path length
M	Molecular weight
P	Total pressure
S	Linestrength
T	Temperature
v	Speed

Chapter 1

Introduction

1.1 Background and Motivation

Combustion is a widely employed energy conversion technology that serves as a powerful energy source for industrial applications. However, the large amount of gas emissions has raised concerns due to their negative impact on climate change. With the urgent need to achieve carbon neutrality, significant efforts are being made to reduce emissions by developing cleaner fuel to eliminate the generation of CO_x , NO_x and SO_x as well as updating combustors to improve combustion efficiency [1; 2]. Temperature and species concentration are two important combustion parameters. Accurate *in situ* measurements of them are crucial for analysing and diagnosing the combustion process. In industrial applications, *in situ* measurements are often challenging due to flow turbulence, multiple sources of noise, and harsh environments. Therefore, it is highly desired to develop accurate, fast, and robust sensors for combustion diagnosis.

Most of the traditional measurement techniques are probe-based, such as the ThermoCouple (TC) for temperature measurement [3] and the extractive gas sampling probe with gas analysis methods like Fourier-Transform Infrared Spectroscopy (FTIR) [4] and gas chromatography [5] for species concentration measurement. They are usually regarded as benchmark techniques for combustion diagnosis due to their long application history and widespread use. Nevertheless, those techniques suffer from point-wised measurement and low temporal resolution, e.g. typically respond at a level of a few seconds, which limits their application on the plane or volumetric temperature and species concentration retrieval. Hence they are unsatisfied with the requirements for validating Computational Flow Dynamics (CFD) models of complex and dynamic reactive flows [6].

Optical techniques for combustion diagnosis attract significant attention due to their non-intrusive nature and fast response in investigating the combustion process. Based on the difference in the light source measured, these techniques fall into two categories: passive and active. Radiation imaging is a typical passive measurement technique. It captures the self-emitted incandescent light of particles during combustion to infer particles' temperature and density. Pictures of incandescent light emission with high spatial resolution can be obtained by camera devices. However, the contamination from the environmental light limits the accuracy of measurement [7]. Active techniques refer to optical techniques that require external light sources. For example, Nd: YAG is a kind of high-power laser source commonly employed as pump lasers in techniques that require high power to excite the gas targets such as laser Rayleigh scattering [8], coherent anti-strokes Raman scatter [9], and laser-induced fluorescence [10]. However, high-power lasers typically have strict cooling and vibration requirements that restrict their usage in harsh industrial environments.

Benefiting from the compactness and resilience of modern diode laser devices, Laser Absorption Spectroscopy (LAS) is one of the most widely utilised active optical techniques in industrial settings. This technique measures the light intensity absorbed by the species at a specific wavenumber of light when the laser beam penetrates the target. By incorporating techniques for light signal generation and acquisition, LAS enables real-time assessment of the dynamic combustion process. A common implementation of LAS employs an emitter-receiver configuration for the measurement of each laser beam, which measures the integration of the gas properties along the light path, the so-called line-of-sight measurement. In practical scenarios, the gas properties along the light path are not uniformly distributed. Single line-of-sight measurement is insufficient to capture the non-uniform distribution along the light path. To achieve a more precise reconstruction of the distribution of gas properties, additional measurements from different angles, i.e. tomographic implementations, are required to provide more spatial information. Tomographic imaging is crucial in this context as it enables the reconstruction of distributions of gas properties by incorporating multiple line-of-sight LAS measurements. This approach allows for a more accurate representation of gas properties at specific points. It also facilitates adaptation to industrial applications [11].

The implementation of tomographic techniques using LAS, named LAS tomography hereafter, requires the strategic deployment of numerous measurement beams on the detection plane to optimise the accuracy of the reconstruction. However, the utilisation of mechanical scanning to increase the number of sampling is not viable in terms of capturing the transient characteristics of highly dynamic flames [12]. In this case, it is necessary to deploy a large number of emitting and receiving sensors around the target, allowing for simultaneous measurements. Fibre optics are commonly utilised to emit and collect thin laser beams, allowing relatively small and discontinuous optical windows around the perimeter of the detect plane [11]. Nevertheless, the physical dimensions of the sensor still limited the number of beams that can be deployed within the detection range. Due to insufficient sampling, state-of-the-art LAS tomographic reconstruction often encounters difficulties in dealing with ill-posed problems and artefacts. Techniques such as iterative reconstruction [13] and regularisation [14] have been developed to mitigate ill-posed problems. However, these algorithms cannot provide physical information to the reconstruction and thus limit their improvement to the reconstruction with penetrating spatial resolution. There has been a growing interest in data-driven reconstruction methods in recent years, primarily driven by their ability to achieve good temporal and spatial resolution. Methods such as Extreme Learning Machine (ELM) [15], and mixed-scale dense Convolutional Neural Networks (CNNs) [16] have been effectively adapted as potential solutions to the tomographic inverse problem. However, these approaches still necessitate a significant amount of prior information regarding the target object to facilitate training and learning.

1.2 Aims and Objectives

The primary goal of this PhD project is to design and develop a LAS tomographic sensor that fulfils specific requirements for accurate and fast measurements of gas temperature and concentration in combustion processes with a customised spatial resolution. The project aims to address the following objectives:

1. Improve spatial resolution and reconfigurability of tomographic system: The sensor should be designed to have smaller spacing between neighbouring laser beams, enhancing the ability to capture detailed spatial information of the gas distribution. Additionally, reconfigurable beam arrangements are required in the design to adapt to different measurement requirements.

2. Ensure robustness and accuracy for *in situ* testing on engine exhaust: The sensor should be capable of operating in challenging environments, such as engine exhaust, where harsh test conditions, such as high temperature, acoustic noise, and mechanical vibration exist. The sensor should also provide reliable measurements of gas properties in real-time, enabling effective monitoring and control of combustion processes.
3. Provide flexibility for customising spatial resolution: The sensor should allow for the adjustment of spatial resolution according to specific applications, providing versatility in capturing different levels of details in the gas properties' distributions.

1.3 Main Contributions

The main contributions of this thesis are summarised as follows:

1. A compact and modular LAS sensor has been developed to enhance the re-configurability of LAS tomographic systems. This sensor design introduces a modular approach for each emitting and receiving sensor, allowing for a significant reduction of neighbouring beam spacing to 1 cm. This reduction in spacing improves the system's ability to capture fine-scale details in the gas distribution. Moreover, the modular design offers advantages in terms of transportation, assembly, maintenance, and replacement of the tomographic sensor, making it suitable for challenging environments. Additionally, the use of off-the-shelf components in the sensor design significantly reduces its cost, increasing its practicality and accessibility for a wide range of applications.
2. A multi-channel LAS sensor has been designed to simultaneously and rapidly monitor the Exhaust Gas Temperature (EGT) and water vapour (H_2O) concentration of Gas Turbine Engines (GTEs). A Distributed-FeedBack (DFB) laser emitted seven beams at 5000.2 cm^{-1} , revealing a trapezoidal absorption distribution at the plume edge with a spatial resolution of 6.3 mm. The sensor's accuracy was validated against extractive gas sampling and TC measurements on a commercial Auxiliary Power Unit (APU), showing a molar fraction difference of 0.02% and a temperature difference of 3°C . The sensor's temporal resolution of 4 ms provides additional insights into GTE's dynamic behaviours, such as EGT and H_2O concentrations variations during engine ignition and fuel injection, facilitating next-generation real-time GTE control towards low emissions.

3. A size-adaptive hybrid meshing scheme has been proposed to improve the reconstruction of target flow fields in terms of image quality and computational efficiency. Based on the required spatial resolution, The five steps in the scheme quantitatively customise the mesh size in and out of the Region of Interest (RoI). This customisation reduces rank deficiency in the LAS tomographic inverse problem, resulting in improvements in reconstruction accuracy. Numerical results show that the size-adaptive hybrid meshing scheme outperforms the traditionally uniform-size meshing scheme, with lower image error, reduced dislocation, and more accurate peak values. Experimental validation confirms the scheme's superiority, revealing finer details, clearer boundaries, and more accurate concentration in the reconstructed flow fields.

1.4 Thesis Outline

The thesis is composed of 6 chapters and the remaining parts are structured as follows. Following the introductory part of this chapter, Chapter 2 presents the literature review of LAS tomography. This includes the fundamentals of LAS measurement techniques, the basics of LAS tomography, the existing LAS tomographic sensor for imaging gas properties and the state-of-the-art LAS tomography reconstruction algorithms.

Chapter 3 of the thesis provides an overview of the LAS tomographic system, in the context of hardware implementation, followed by a lab-scale system demonstrated as an example. Additionally, the design of modular emitters and receivers is introduced. The feasibility of the prototype is verified through experiments. Application scenarios are also presented to showcase the system's capabilities when implemented using the modular design.

Moving to Chapter 4, the focus shifts to a practical experiment involving the detection of exhaust gas from a commercial APU. The chapter will discuss the selection of spectral lines for measurement, the design of a new multi-channel sensor, the experimental procedure and the analysis of test results. This experiment highlights the value of multi-channel systems in detecting the properties of gas with non-uniform distribution.

In Chapter 5, a new meshing method is introduced that incorporates the information about beam arrangement into the reconstruction process. The chapter explains the underlying principle of the method and presents its numerical validation. Furthermore, the effectiveness of this method in improving the reconstruction of gas properties is demonstrated through experimental validation involving complex gas distributions.

Finally, Chapter 6 summarises the scientific contributions of the thesis and discusses the potential work in the future with an emphasis on the further development of LAS tomographic sensors.

Chapter 2

Literature review

2.1 Introduction

Following the introduction of the current-injection laser in the late 1960s, diode lasers emerged as a viable option for detecting pollutant emissions in combustion processes [17]. LAS techniques were first introduced in the late 1970s as a means to measure the concentration of infrared-reactive species such as CO, NO, C₂H₄ and H₂O [18; 19]. With the rapid advancements in semiconductor laser technology during the 1990s, the range of available laser wavelengths expanded significantly. This extension in wavelength range opened up opportunities to probe and detect a broader range of species using LAS [?]. Within a few decades, LAS technologies demonstrated their advantages in terms of accuracy, sensitivity, and applicability. It becomes one of the most powerful gas sensing techniques in monitoring a variety of gas parameters related to the combustion process, such as temperature, pressure, velocity and species concentration [20]. Furthermore, the increasing need to monitor complex and asymmetric combustion fields has driven the development of LAS tomographic techniques for reconstructing distribution of gas properties. However, the inherent ill-posed problem of the LAS tomographic inverse problem hinders enhancing spatial resolution. Therefore, considerable efforts have been devoted to the investigation and alleviation of the ill-posed problems.

This chapter will commence with a concise overview of the fundamental physical principles underlying LAS, encompassing Beer-Lambert law and broadening mechanisms. Subsequently, the fundamentals of LAS techniques will be introduced, with a comprehensive exposition of the Calibration-Free Wavelength Modulation Spectroscopy (CF-WMS) technique and its fitting process. The fundamentals of LAS tomography are reviewed, followed by a review of notable implementations of LAS tomo-

graphic sensors. In order to facilitate the demonstration of the ill-posed problems, the basics of Singular Value Decomposition (SVD) will be briefly introduced. Lastly, an overview of the state-of-the-art reconstruction algorithms for mitigating ill-posed problems in LAS tomography will be presented.

2.2 Beer-Lambert Law

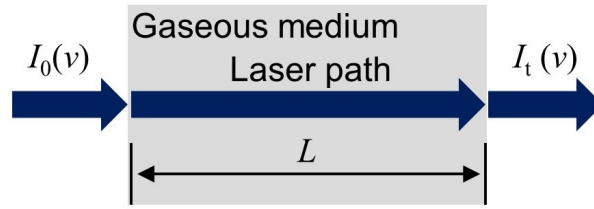


Figure 2.1: Beer-Lambert law.

The principle underlying LAS is described by Beer-Lambert law: the attenuation of light passing through an absorbing medium is directly related to the properties of the medium. In the case of LAS, when a laser beam at wavenumber ν [cm^{-1}], viz. reciprocal of wavelength, passes through a uniform gaseous medium, as Figure 2.1 shows, the relationship between the transmitted light intensity, notes $I_t(\nu)$, and incident light intensity, notes $I_0(\nu)$, can be described by the equation:

$$I_t(\nu) = I_0(\nu) \times e^{-A(\nu)}, \quad (2.1)$$

where A is defined as absorbance which relates to gas properties. If only one transition of a species is considered, the A can be expressed as

$$A(\nu) = LP\chi S(T)\Phi(\nu, P, \chi, T), \quad (2.2)$$

where L [cm] is the path length. P [atm] is the total pressure. T [K] is the temperature. χ is the mole fraction of species. S [$\text{cm}^{-2} \text{ atm}^{-1}$] and Φ [cm] are the linestrength and lineshape of a particular transition of the species. As the area underneath lineshape function Φ is normalised to unity,

$$\int_{-\infty}^{+\infty} \Phi d\nu \equiv 1. \quad (2.3)$$

The path-integrated absorption, noted as B in this thesis, is defined by the integration of A over the wavenumber:

$$B = \int_{-\infty}^{+\infty} A(\nu) d\nu = LP\chi S(T). \quad (2.4)$$

2.3 Lineshape Function

The broadening of an absorption feature in LAS is a result of physical processes occurring within the medium, which perturbs the energy levels of the transition or the interaction between individual atoms or molecules and the incident light. This broadening phenomenon is influenced by various parameters, including temperature, pressure, and gas concentration, as represented by Equation 2.2. The broadening can be classified into two categories: inhomogeneous and homogeneous. In the case of inhomogeneous broadening, the distinct classes or subgroups within the species lead to variations in the interaction, resulting in non-uniform broadening. On the other hand, homogeneous broadening occurs when all atoms or molecules of the species experience the same interaction, resulting in a uniform broadening effect [21].

In the following section, we will discuss three commonly used lineshape functions that describe the broadening effects in LAS: Gaussian, Lorentzian, and Voigt.

2.3.1 Gaussian Lineshape Function

The random thermal motion of the absorbing molecules leads to the inhomogeneous Doppler broadening effect [22]. According to statistical mechanics, the distribution of molecular speeds within a dilute gas follows the Maxwellian distribution [23]. Consequently, the Doppler lineshape is characterised by a classical bell-shaped Gaussian curve at the linecentre wavenumber ν_0 [cm^{-1}]:

$$\Phi_D(\nu) = \frac{2}{\Delta\nu_D} \sqrt{\frac{\ln 2}{\pi}} \exp \left\{ -4 \ln 2 \left(\frac{\nu - \nu_0}{\Delta\nu_D} \right)^2 \right\}, \quad (2.5)$$

where $\Delta\nu_D$ is the Full Width at Half Maximum (FWHM) of the lineshape, called the Doppler width. It can be calculated using:

$$\Delta\nu_D = \nu_0 \sqrt{\frac{8kT \ln 2}{Mc^2}} = 7.1623 \times 10^{-7} \nu_0 \sqrt{\frac{T}{M}}, \quad (2.6)$$

where M [a.m.u] is the molecular weight of the absorbing species.

In Equation 2.6, the Doppler width is primarily determined by the temperature of the gas. A higher gas temperature leads to a larger Doppler width, resulting in a broader spectral line. In cases where temperature variations dominate the behaviour of the absorbing molecule, the Gaussian lineshape is appropriate to describe the observed spectral profile.

The peak height of the Gaussian lineshape function is

$$\Phi_D(\nu_0) = \frac{2}{\Delta\nu_D} \sqrt{\frac{\ln 2}{\pi}}. \quad (2.7)$$

2.3.2 Lorentzian Lineshape Function

As discussed above, inhomogeneous Doppler broadening is the dominant factor influencing the absorption lineshape in low-pressure conditions, which is described by a Gaussian lineshape function. However, in high-pressure environments, the influence of homogeneous broadening becomes more prominent, leading to a Lorentzian lineshape. Homogeneous broadening is primarily influenced by two mechanisms: natural lifetime broadening and collisional broadening [21].

Natural broadening arises from the inherent uncertainty in the energy of states involved in the absorption transition, which have finite lifetimes. When the absorption line is solely influenced by the natural lifetime of the energy states, it is referred to as "natural" broadening. However, in many cases, natural broadening can be disregarded due to the long lifetimes of the energy states [20].

Another important uniform broadening mechanism is collisional broadening. It is generated by collisions of the emitting or absorbing particle with other particles. Based on two key assumptions: First, collisions are binary. Second, collision duration is negligible. Collisional broadening takes the form of a Lorentzian profile,

$$\Phi_c(\nu) = \frac{1}{\pi} \frac{\frac{\Delta\nu_c}{2}}{(\nu - \nu_0)^2 + \left(\frac{\Delta\nu_c}{2}\right)^2}, \quad (2.8)$$

where $\Delta\nu_c$ [cm^{-1}] is the collisional FWHM.

The collision also occurs between different species. The total collision width in a multi-species environment can be expressed by

$$\Delta\nu_c = P \sum_j (\chi_j 2\gamma_j), \quad (2.9)$$

where χ_j is the mole fraction of j^{th} component, and γ_j [$\text{cm}^{-2}\text{atm}^{-1}$] is the collisional broadening coefficient due to perturbation by the j^{th} component. Meanwhile, γ_j is the Half-Width at Half Maximum (HWHM) per atm of the pressure of the partner j , and the temperature dependence of γ_j can be expressed as:

$$\gamma_j(T) = \gamma_j(T_0) \left(\frac{T_0}{T} \right)^{n_j}, \quad (2.10)$$

where T_0 is the reference temperature and $T_0 = 296$ K. n_j represents the corresponding coefficient of temperature dependence. It is clear that pressure has a significant influence on the lineshape. Usually, when the pressure is higher than 0.1 atm, Lorentz lineshape must be considered.

The peak height of the Lorentzian lineshape function is

$$\Phi_c(\nu_0) = \frac{2}{\Delta\nu_c\pi}. \quad (2.11)$$

2.3.3 Voigt Lineshape Function

In reality, the absorption lineshape is a combination of Gaussian and Lorentzian components, resulting in a Voigt lineshape function. The Voigt lineshape function is obtained through the convolution of the Gaussian lineshape and the Lorentzian lineshape [24]. When the broadening mechanisms are independent, the Voigt lineshape can be described as

$$\Phi_V(\nu) = \int_{-\infty}^{+\infty} \Phi_D(\nu) \Phi_c(\nu - u) du. \quad (2.12)$$

To establish the relationship between Doppler broadening and collision broadening, the Voigt " α " parameter can be defined as follows:

$$\alpha = \frac{\sqrt{\ln 2} \Delta\nu_c}{\Delta\nu_D}, \quad (2.13)$$

with the non-dimensional line position w as

$$w = \frac{2\sqrt{\ln 2}(v - v_0)}{\Delta v_D}, \quad (2.14)$$

and the integral variable y as

$$y = \frac{2\sqrt{\ln 2}u}{\Delta v_D}. \quad (2.15)$$

Then the Voigt lineshape function becomes

$$\Phi_V(v) = \frac{2}{\Delta v_D} \sqrt{\frac{\ln 2}{\pi}} \frac{\alpha}{\pi} \int_{-\infty}^{+\infty} \frac{\exp(-y^2)}{\alpha^2 + (w - y)^2} dy = \Phi_D(v_0) \frac{\alpha}{\pi} \int_{-\infty}^{+\infty} \frac{\exp(-y^2)}{\alpha^2 + (w - y)^2} dy. \quad (2.16)$$

It is important to note that the parameter α in the Voigt lineshape function reflects the correlation between the Gaussian and Lorentzian components. When the value of $\alpha \rightarrow 0$, the Voigt lineshape function resembles a pure Gaussian lineshape. Conversely, as the value of $\alpha \rightarrow \infty$, the Voigt lineshape function transforms into a pure Lorentzian lineshape.

From Equation 2.16, the Voigt function is a result of convolution. A simple analytic form is not available. Olivero [25] and Mayinger [26] gave experimental solutions to estimate the linewidth, i.e. FWHM, and peak height, respectively.

The FWHM of the Voigt lineshape can be estimated using

$$\Delta v_V = 0.5346 \Delta v_c + \sqrt{(0.2166 \Delta v_c^2 + \Delta v_D^2)}. \quad (2.17)$$

The peak height of the Voigt lineshape function can be described as

$$\Phi_V(v_0) = \left[\left(\frac{\beta}{\gamma_{ED} \sqrt{\pi}} \right) + \left(\frac{1 - \beta}{\pi \cdot \gamma_c} \right) \right], \quad (2.18)$$

with

$$\beta = \frac{\gamma_{ED}}{(\gamma_c + \gamma_{ED})}, \quad (2.19)$$

and

$$\gamma_{ED} = \frac{\gamma_D}{\sqrt{\ln 2}}, \quad (2.20)$$

where γ_D and γ_c are HWHM of the Gaussian and Lorentzian shapes, respectively.

2.4 Laser Absorption Spectroscopy Techniques

The advent of reliable, room temperature, and narrow-linewidth Tunable Diode Lasers (TDLs) has facilitated the development and application of numerous LAS measurement technologies. Direct Absorption Spectroscopy (DAS) and Wavelength Modulation Spectroscopy (WMS) are the two most common implementations for LAS sensing.

2.4.1 Direct Absorption Spectroscopy

Based on Beer-Lambert law and broadening effects mentioned in Section 2.3, an absorption feature can be retrieved from a transmitted light signal with wavenumber scanning near the centre wavenumber of linestrength, which enables DAS techniques [17; 27; 28; 29].

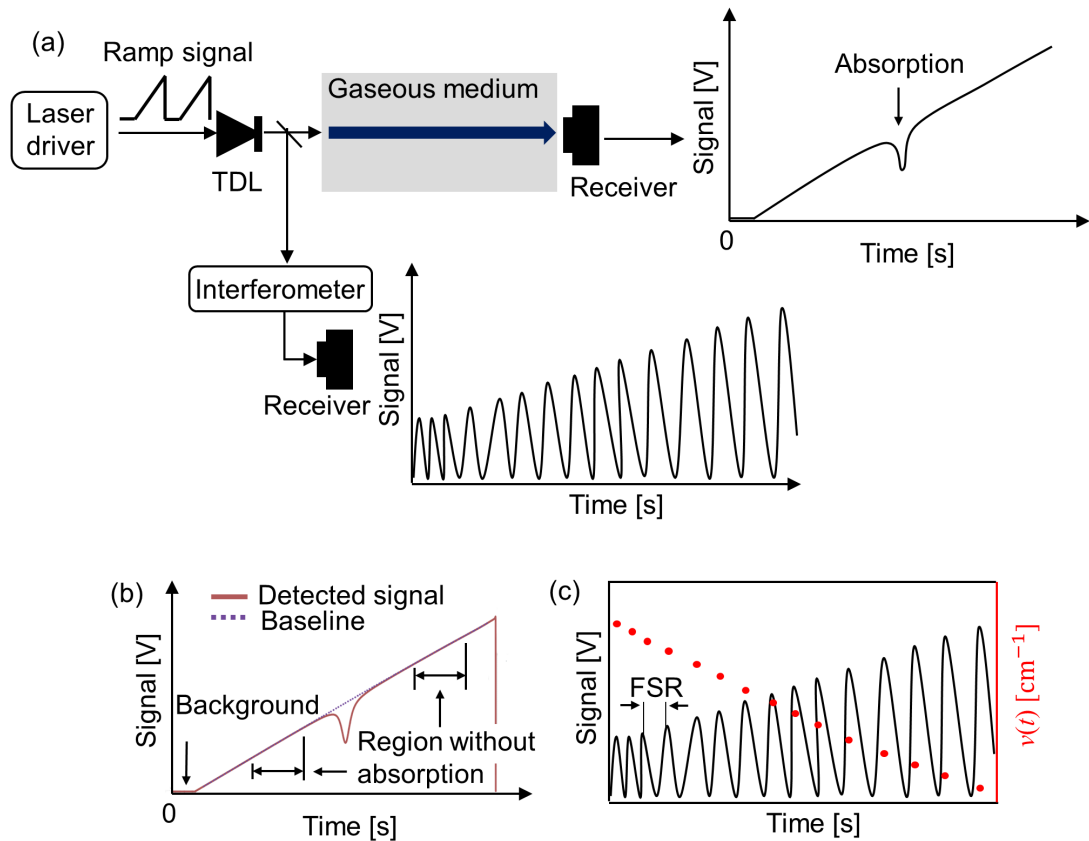


Figure 2.2: Schematic of a typical DAS implementation: (a) Example experiment setup. (b) Baseline fitting of the DAS signal. (c) Laser characterisation.

A typical DAS implementation is shown in Figure 2.2. In (a), the laser diode is turned on to generate an offset signal followed by a ramp signal. The laser is split into two channels. One passes through the gaseous medium and is received by the receiver giving an absorption detection. The other one passes through the interferometer resulting oscillated output signal. The (b) demonstrated the post-process of the DAS signal. The non-absorption transmission baseline is derived via those regions without absorption. Then, the absorption feature is extrapolated simply by subtracting transmitted intensity from the baseline.

In practice, the injected current tunes the laser intensity and wavenumber simultaneously. However, the wavenumber tuning is not linear. In order to convert the attenuation of light intensity in the time domain into the absorption feature in the wavenumber domain for analysing the gas properties, laser characterisation is necessary. It is conducted as a part of the experiment to quantify the temporal changes in the wavenumber. Devices such as ring resonator, Fabry–Pérot interferometer (known as etalon) and Mach–Zehnder interferometer [30] with known Free Spectral Range (FSR) are used to characterise the time-varied wavenumber change, note as $\nu(t)$. As (c) shows, the wavenumber difference between the two peaks in the obtained signal equals to a fixed FSR. Hence the relationship can be derived by plotting the wavenumber value according to time.

DAS techniques offer two primary advantages due to their simple mechanism:

1. The calculation based on the fitting of the absorption feature can cover the broadening effects and infer gas properties.
2. For applications where non-absorption measurement is not accessible, the baseline can be obtained by fitting the non-absorption region.

However, the disadvantages are also concerning in industrial applications:

1. In industrial applications where high pressures are present, there is a notable increase in spectral line broadening. This can pose challenges, especially when using TDLs, as the spectral line broadening may exceed the coverage range of these lasers. As a result, the accuracy of the measurements may be compromised.
2. In environments characterised by high turbulence, such as combustion processes, the detected signals can be severely distorted by the dynamic thermal conditions within the laser path. This makes it difficult to establish a stable and reliable baseline for absorption measurements. Consequently, the extraction of accurate absorption information becomes challenging [28].

2.4.2 Wavelength Modulation Spectroscopy

The accuracy of DAS may be compromised in situations involving high pressure, low absorption, or high noise conditions. These situations introduce significant distortion to the baseline and absorption features. However, in WMS, the driving current of the laser diode is a superposition of a high-frequency sinusoidal modulation f_m [Hz] with a low-frequency scan f_s [Hz]. Unlike DAS, whose analysis is based on fitting the absorption feature, WMS analyses the harmonic components of the detected signal. This allows for significant mitigation of interference in low frequency such as room light, flame emission, and noise, ultimately ensuring a higher Signal-to-Noise Ratio (SNR) [31].

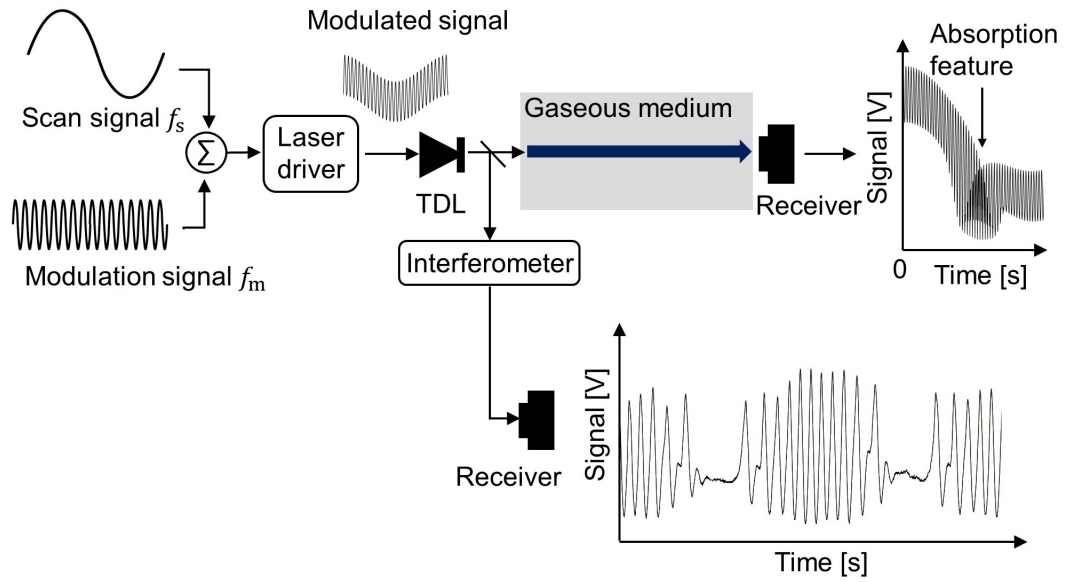


Figure 2.3: Typical schematic of WMS measurement.

A typical WMS implementation is shown in Figure 2.3. The laser driver feeds a modulated signal to the TDL. As a result, the TDL's output intensity and wavenumber are modulated accordingly. While the scan signal can take the form of either step, ramp or sinusoid [32], the latter is demonstrated here due to its smooth transition, which reduces susceptibility to the response time of capacitive devices. The modulated inject current tunes the output wavenumber of the TDL, which can be formulated as:

$$\nu(t) = \nu_s(t) + a_{m1} \cos(2\pi f_m t), \quad (2.21)$$

where $\nu_s(t)$ [cm^{-1}] is the scan wavenumber. a_{m1} [cm^{-1}] is the modulation amplitude.

The TDL's output intensity I_0 can be described as:

$$I_0(t) = I_s(t)[1 + i_1 \cos(2\pi f_m t + \varphi_1) + i_2 \cos(4\pi f_m t + \varphi_2)], \quad (2.22)$$

where $I_s(t)$ is the scanning laser intensity without modulation. i_1 is the amplitude of linear Intensity Modulation (IM). φ_1 is the phase shift between the Frequency Modulation (FM) and the IM. i_2 is the amplitude of non-linear IM and φ_2 is its phase shift.

Then the laser output is split into two channels. One passes through the gaseous medium and is detected by the receiver. To better demonstrate the relationship between the absorbance and the harmonics components of the transmitted signal, transmission coefficient $\tau(\nu)$ is introduced here based on Beer-Lambert law.

$$\tau(\nu) = \frac{I_t}{I_0} = e^{-A(\nu)}, \quad (2.23)$$

and the transmission coefficient can be expanded in Fourier cosine series,

$$\tau(\bar{\nu} + a \cos(2\pi f_m t)) = \sum_{n=0}^{n=+\infty} H_n(\bar{\nu}, a) \cos(n2\pi f_m t), \quad (2.24)$$

where $H_n(\bar{\nu}, a)$ is the n^{th} Fourier coefficient of the transmission coefficient. They are given by

$$H_0(\bar{\nu}, a) = \frac{1}{2\pi} \int_{-\pi}^{+\pi} \tau(\bar{\nu} + a \cos \theta) d\theta, \quad (2.25)$$

and

$$H_n(\bar{\nu}, a) = \frac{1}{\pi} \int_{-\pi}^{+\pi} \tau(\bar{\nu} + a \cos \theta) \cdot \cos(n\theta) d\theta. \quad (2.26)$$

Represent the Equation 2.23 with the Fourier series derived in Equation 2.24. Then the transmitted intensity with the presence of the absorption can be written as:

$$I_t(t) = I_s(t) \left[1 + \sum_{n=1}^{\infty} i_n \cos(n2\pi f_m t + \varphi_n) \right] \times \left[\sum_{n=0}^{\infty} H_n \cos(n2\pi f_m t) \right], \quad (2.27)$$

where i_n is the n^{th} Fourier coefficient of the incident intensity. φ_n is the phase shift of its n^{th} harmonics.

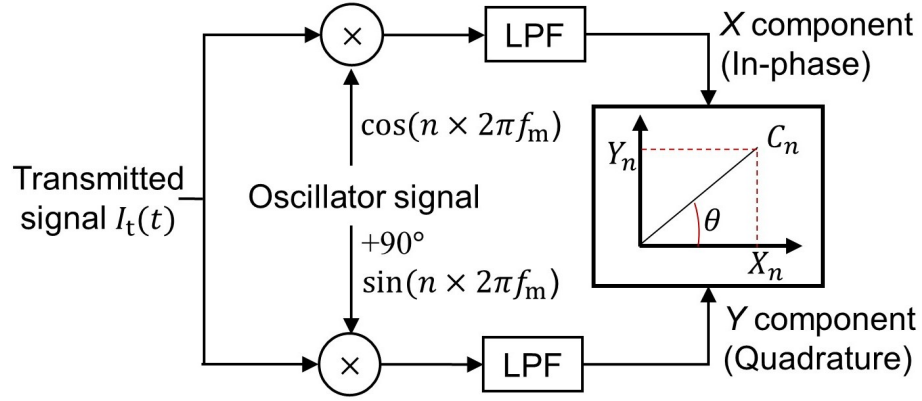


Figure 2.4: Schematic of lock-in signal process.

The digital Lock-in amplifier and Low Pass Filter (LPF) are commonly used to extract the harmonic signals from the detected transmitted signal. This process is illustrated in Figure 2.4. To demodulate the n^{th} harmonic signal, I_t will multiply by in-phase and quadrature oscillated signals with the frequency of the n^{th} harmonic, respectively. Then the products of them are filtered by the LPF, giving in-phase X and quadrature Y components of the n^{th} harmonic signal. The magnitude C_n and phase θ_n is giving by:

$$C_n = \sqrt{X_n^2 + Y_n^2} \quad (2.28)$$

and

$$\theta_n = \tan^{-1} \frac{Y_n}{X_n}. \quad (2.29)$$

Considering the fact that the magnitude of the n^{th} harmonics, noted as nf , decreases as the harmonics frequency increases, the first and second harmonics signals, noted as $1f$ and $2f$ are often prioritised for sensing the gas properties due to high signal intensity. If the non-linear intensity response is insignificant, the output X and Y components of $1f$ and $2f$ can be approximated as:

$$X_1 \approx \frac{G\bar{I}}{2} [H_1 + i_1(H_0 + \frac{H_2}{2}) \cos \phi_1 + \frac{i_2}{2}(H_1 + H_3) \cos \phi_2]; \quad (2.30)$$

$$Y_1 \approx -\frac{G\bar{I}}{2} [i_1(H_0 - \frac{H_2}{2}) \sin \phi_1 + \frac{i_2}{2}(H_1 - H_3) \sin \phi_2]; \quad (2.31)$$

$$X_2 \approx \frac{G\bar{I}}{2} [H_2 + \frac{i_1}{2}(H_1 + H_3) \cos \phi_1 + i_2(H_0 + \frac{H_4}{2}) \cos \phi_2]; \quad (2.32)$$

$$Y_2 \approx -\frac{G\bar{I}}{2} [\frac{i_1}{2}(H_1 - H_3) \sin \phi_1 + i_2(H_0 - \frac{H_4}{2}) \sin \phi_2], \quad (2.33)$$

where \bar{I} is the average intensity of the scanning intensity signal. G is the electro-optical gains of the detection system. The magnitude of $1f$ and $2f$ harmonics signals C_1 and C_2 are calculated via Equation 2.28.

To avoid calibrating the electro-optical gains and eliminating the influence of the background, the $1f$ signal and the non-absorption measurements are used to normalise the $2f$ signal. This technique is called CF-WMS- $2f/1f$ [33].

$$\text{CF-WMS-}2f/1f = \sqrt{\left(\frac{X_2}{C_1} - \frac{X_2^0}{C_1^0}\right)^2 + \left(\frac{Y_2}{C_1} - \frac{Y_2^0}{C_1^0}\right)^2}, \quad (2.34)$$

where $(\cdot)^0$ denotes the signal measured in the absence of absorption, i.e. background.

Similar to DAS, the other channel of the TDL's output is fed to an interferometer. Consequently, the receiver captures a signal characterised by high oscillations. The separation between peaks in the etalon trace is constant and always matches the FSR. Furthermore, the wavenumber change shows the opposite monotonicity to the variation in light intensity. The wavenumber is determined by plotting the positions of these peaks, which correspond to the increase and decrease in the number of FSRs. As shown by Figure 2.5, the according wavenumber and time relationships are indicated by the red dots.

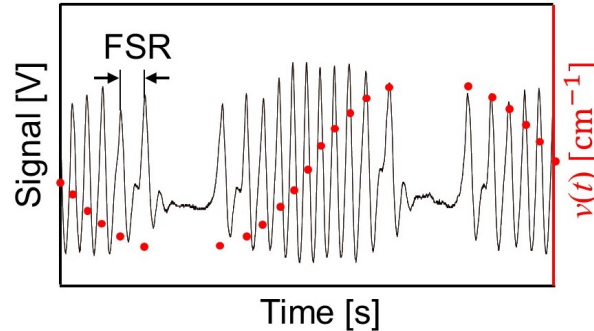


Figure 2.5: Laser characterisation of TDL's WMS output.

Equation 2.21 formulates the wavenumber modulation in an ideal case. In practice, the discontinued wavenumber value is fitted by

$$\begin{aligned} v(t) = & v_0 + a_{s1} \cos(2\pi f_s t + \psi_{s1}) + a_{s2} \cos(4\pi f_s t + \psi_{s2}) + \\ & [a_{n1} + a_{n1} \cos(2\pi f_s t + \psi_{n1})] \cos(2\pi f_m t + \psi_{m1}) + a_{m2} \cos(4\pi f_m t + \psi_{m2}), \end{aligned} \quad (2.35)$$

where ν_0 is the centre wavenumber of the laser. a_{s1} and a_{s2} are the scan amplitude of linear and nonlinear components, respectively. ψ_{s1} and ψ_{s2} are the phase shift to inject current scan of linear and nonlinear components, respectively. $a_{n1} + a_{n1} \cos(2\pi f_s t + \psi_{n1})$ uses an offset a_{n1} with a sinusoid to present the nonlinearity of the modulation amplitude on the first harmonics, a_{m2} denotes the modulation amplitude of the second harmonics components. ψ_{m1} and ψ_{m2} are the phase shift to inject current modulation of linear and nonlinear components, respectively.

Fitting of Calibration-Free WMS

Many methods have been mentioned in previous research to extract gas properties from the transmitted WMS signal. The fitting of CF-WMS technique is one of the most representative methods enabling good accuracy [34].

When absorption B is extracted via fitting measured CF-WMS $2f/1f$ signal with a simulated one, four parameters, centre wavenumber of the linestrength ν_0 , path-integrated absorption B , Gaussian linewidth $\Delta\nu_D$, and Lorentz linewidth $\Delta\nu_c$ are set as variables for fitting. The least-square error method is commonly used to retrieve these parameters. The schematic of this technique is shown in Figure 2.6.

2.4.3 Ratio Thermometry

From Equation 2.4, the path-integrated absorption B is determined by path length L , total pressure P , species concentration χ , and the temperature dependence linestrength $S(T)$. Normally the optical path length can be easily measured, while the pressure is assumed to be a known constant along the measurement path. Then χ and $S(T)$ are left unknown. It is not possible to calculate two unknowns from a single measured value, as it would lead to an underdetermined system. Hence multiple measurements on the same gas sample at different transitions are required.

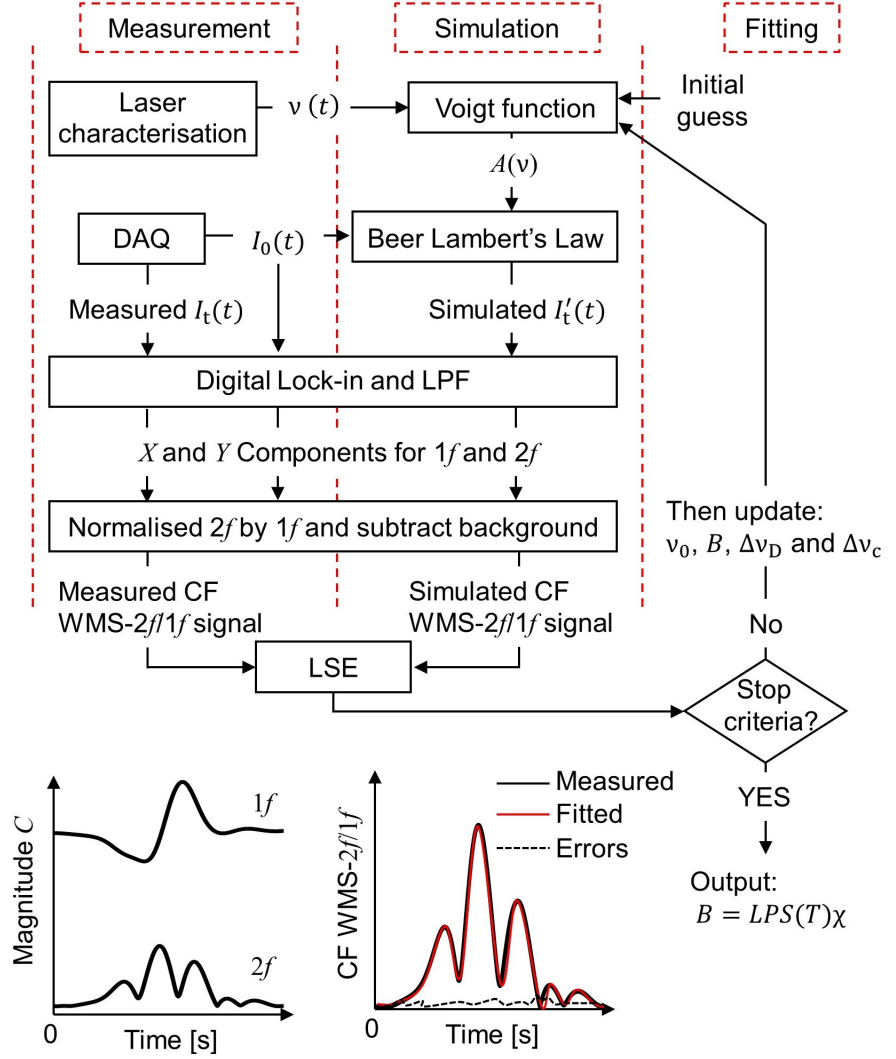


Figure 2.6: Demonstration of fitting the CF-WMS-2f/1f to extract path-integrated absorption.

Ratio thermometry is the most widely used method for WMS temperature measurement [35; 36]. The gas temperature can be determined by comparing the linestrengths of two different transitions, each exhibiting a distinct temperature dependence and derived by

$$S(T) = S(T_0) \frac{Q(T_0)}{Q(T)} \left(\frac{T_0}{T} \right) \times \exp \left[-\frac{hcE''}{kT} \left(\frac{1}{T} - \frac{1}{T_0} \right) \right] \left[1 - \exp \left(-\frac{hc\nu_0}{kT} \right) \right] \left[1 - \exp \left(-\frac{hc\nu_0}{kT_0} \right) \right]^{-1}, \quad (2.36)$$

where $S(T_0)$ is the known linestrength for a transition at reference temperature $T_0 = 296$ K from HITRAN database [37]. $Q(T)$ is the molecular partition function. h [J·s] is Planck constant. c [cm/s] is the speed of light. k [J/K] is Boltzmann's constant. And E'' [cm^{-1}] is the lower-state energy.

The temperature-dependence partition function can be approximated by the following polynomial:

$$Q(T) = a_1 + a_2T + a_3T^2 + a_4T^4, \quad (2.37)$$

where coefficients a_1 , a_2 , a_3 and a_4 can be found in HITRAN/HITEMP databases [38].

Then the temperature can be derived by taking the ratio of the path-integrated absorption of two transitions. If the centre frequency of the two transactions is close to each other, the ratio is described as

$$R(T) = \frac{B_1}{B_2} = \frac{\int PL\Phi_1 S_1(T) d\nu}{\int PL\Phi_2 S_2(T) d\nu} = \frac{S_1(T)}{S_2(T)} = \frac{S_1(T_0)}{S_2(T_0)} \exp\left[-\frac{hc}{k}(E_1'' - E_2'')\left(\frac{1}{T} - \frac{1}{T_0}\right)\right], \quad (2.38)$$

where $(\cdot)_n$ denotes different transitions.

In addition to cancelling out the unknown concentration term, taking the ratio of two linestrengths offers the advantage of increasing the sensing range of temperature [36]. Figure 2.7 illustrates an example of two linestrengths with different temperature dependencies. The resulting ratio of the two line strengths exhibits a monotonic behaviour, providing a reliable and extended range for temperature measurements.

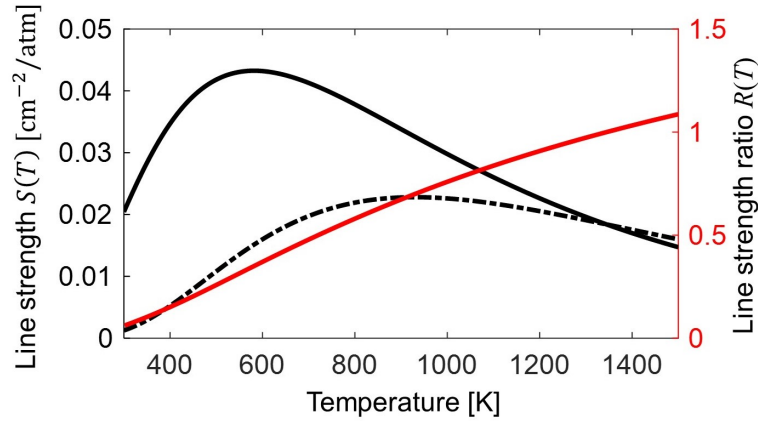


Figure 2.7: Demonstration of two linestrengths with different temperature dependency and resulting ratio.

If the centre frequency of the two linestrengths for implementing ratio thermometry is close to each other, then the temperature along the laser path can be expressed as

$$T = \frac{\frac{hc}{k}(E_2'' - E_1'')}{\ln \frac{B_1}{B_2} + \ln \frac{S_2(T_0)}{S_1(T_0)} + \frac{hc}{k} \frac{E_2'' - E_1''}{T_0}}. \quad (2.39)$$

Based on the known temperature, the gas concentration along the laser path can be calculated with either transition via

$$\chi = \frac{B}{PLS(T)}. \quad (2.40)$$

2.5 LAS Tomography

LAS tomography is a technique used to measure gas properties within a specific plane, where the reconstructed images provide two-dimensional distribution of gas properties. This technique typically involves the use of multiple laser beams passing through the same plane at different angles to sample the information within the plane.

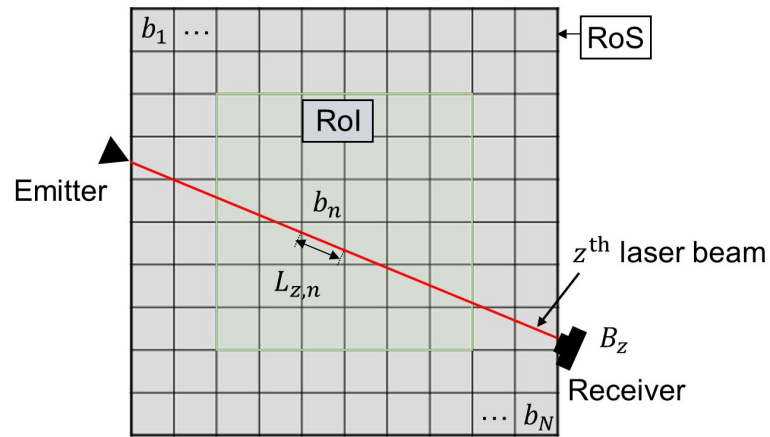


Figure 2.8: Geometric description of a line-of-sight measurement in LAS tomography.

A typical LAS tomography technique is modelled based on linear discretisation of the line-of-sight measurement. As shown in Figure 2.8, the laser sensing area that covers the entire optical path from emitters to receivers is named the Region of Sensing (RoS). It is divided into two parts: RoI which contains the targets, i.e. flame in this thesis, and the out-of-RoI region that reflects the background. The majority of

research efforts have been directed toward the reconstruction of the RoI. However, in this study, the RoS is taken into consideration to ensure physical integrity. Given that the RoS is discretised into N pixels, the absorbing species' temperature, pressure, and mole fraction, i.e. concentration, are assumed to be uniform in each pixel. According to Equation 2.4, the path-integrated absorption B_z of the z^{th} laser beam for the target species is given by

$$B_z = \sum_{n=1}^N L_{z,n} b_n, \quad (2.41)$$

where $L_{z,n}$ represents the chord length of the z^{th} beam within the n^{th} pixel. b_n is the absorption density of the n^{th} pixel at the selected absorption transition [16]. b_n is defined by

$$b_n = P_n \chi_n S(T_n), \quad (2.42)$$

where P_n [atm] the pressure, χ_n the mole fraction of the absorbing species, T_n [K] the temperature, and $S(T_n)$ [$\text{cm}^{-2} \cdot \text{atm}^{-1}$] the linestrength of the transition in the n^{th} pixel.

For a tomographic system with Z laser beams, Equation 2.41 can be formulated as a linear equation

$$\mathbf{L}\mathbf{b} = \mathbf{B}, \quad (2.43)$$

where $\mathbf{L} \in \mathbb{R}^{Z \times N}$ is the sensing matrix. $\mathbf{b} \in \mathbb{R}^{1 \times N}$ is the column vector of pixel-wised absorption density b_n ($n = 1, 2, \dots, N$) to be solved in the inverse problem. $\mathbf{B} \in \mathbb{R}^{Z \times 1}$ is the measured path-integrated absorption.

2.5.1 Beam Arrangement

In the context of practical application, the limited optical access poses difficulty in the beam arrangement and system hardware. Three kinds of sensor implementations: parallel, fan, and irregular, based on their patterns of beam arrangements, have been studied in previous literature.

Parallel Beam

Parallel beam arrangement draws significant attention due to the benefits of isolated beam path and uniform sampling in the sensing region. In 2005, Wright *et al.* [39] demonstrated a system with 32 parallel beams in 4 equiangular projections of 8 beams for hydrocarbon vapour imaging in the premix chamber of a multi-cylinder automotive engine. 8k Hz temporal resolution with dual-wavelength measurement

was achieved. Deguchi *et al.* [40] and Wang *et al.* [41] also demonstrated the effectiveness of parallel beam arrangements in measuring gas properties in power plant reactors. These examples highlight the capability of LAS techniques with parallel beam arrangement to provide valuable insights into combustion processes and facilitate efficient energy generation. In contrast to systems that typically have beam spacing in the range of a few centimetres, a compact sensor was designed by Wang *et al.* [42] with 24 channels and an approximate beam spacing of 1 cm. Subsequent reports on parallel systems have not shown significant reductions in this spacing. On the contrary of small and compact systems, more recently, Upadhyay *et al.* [30] measured the CO distribution in the exhaust of a large-scale commercial aero-propulsion engine. 126 pairs of emitters and receivers were positioned around the exhaust plume, forming 6 equiangular projections with a 7 m optical path length between them. The successful demonstration of the CO distribution map in industrial scenarios further emphasises the advantages of increasing the number of beams for capturing spatial information.

Fan Beam

Unlike isolated emitters that produce individual beams for typical parallel beam arrangement, laser emitting for fan beam arrangement is obtained by transforming a single beam into a fan-shaped beam using simple optics. One advantage of utilising a fan beam arrangement is the ability to overcome the limitations imposed by the size of the fibre optic on the emitting side. Therefore a higher number of beams can be achieved, providing enhanced spatial resolution and coverage. For instance, Xu's group presented a 60-beam system with fan beam arrangement [43; 44; 45; 46]. The fan-beam illumination is produced using an anamorphic prism pair and a cylindrical lens, resulting in a span angle of 24°. The illumination is then sampled by a multi-photodiode array consisting of 12 photodiodes that are equally spaced. By employing this configuration, the system is capable of collecting 60 beams that cover the RoI with a diameter of 6 cm. In comparison to systems utilising a parallel beam arrangement, the fan-beam system demonstrates a higher beam density in the RoI. However, the ill-posed problem is still concerning due to the limited angular dimensions.

Irrgular Beam

In certain applications, optical access to the target is obstructed. In such cases, neither parallel nor fan beam arrangements are practical. Hence alternative irregular beam arrangements are considered. For example, Wright *et al.* [47] implemented a 32-beam sensor with an irregular beam arrangement integrated into the flue premix cylinder. In even harsh environments, Stritzke *et al.* [48] measured Ammonia concentration distribution in the exhaust of heavy-duty diesel engine with only 8 beams in irregular beam arrangement.

In general, the parallel beam arrangement has the advantage of uniformly distributing sampling deficiencies across the RoI. This characteristic is particularly beneficial when there is no or limited prior information about the target. However, it is important to note that in certain situations, fan and irregular beam arrangements may be preferred if they can provide specific advantages or address unique challenges associated with the measurement application. Nonetheless, the parallel beam arrangement remains a common and effective choice for LAS tomographic sensor [49].

Table 2.1 gives a summary of mentioned LAS tomographic sensors. Those good practices show the flexibility of LAS tomographic sensors for a variety of applications.

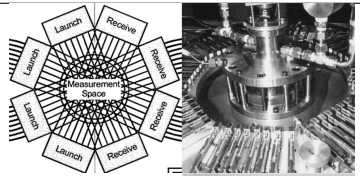
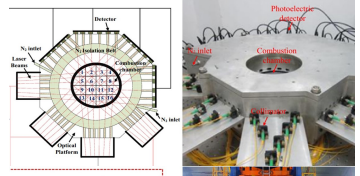
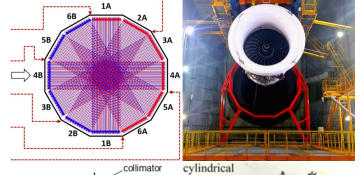
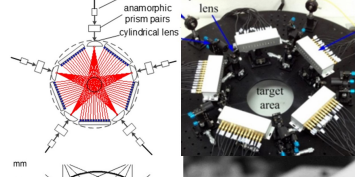
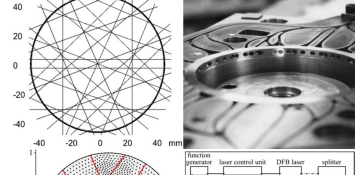
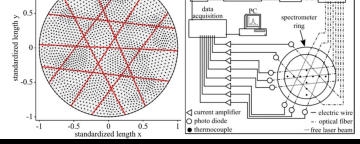
Beam pattern	Reference study	Year	Beam arrangement	Beam spacing (mm)	Application	Working wavelength (nm)	Frame rate (Hz)	System snapshot
Parallel	Wright <i>et al.</i> [39]	2005	32 beams. 4 projections, 8 beams / projection	~35	Multi-cylinder automotive engine	Near 1700 and 1550	8k	
Approx. parallel	Wang <i>et al.</i> [42]	2015	24 beams. 4 projections, 6 beams / projection	~10	Lab burner	Near 1398	1k	
Parallel	Upadhyay <i>et al.</i> [30]	2022	126 beams. 6 projections, 21 beams / projection	~72	Aero-engine	Near 1999	1.25	
Fan	Xu <i>et al.</i> [43]	2016	60 beams. 5 projections, 12 beams / projection		Lab burner	Near 1343 and 1391		
Irregular	Wright <i>et al.</i> [47]	2010	32 beams irregular		Multi-cylinder automotive engine	Near 1700 and 1550	4k	
Irregular	Stritzke <i>et al.</i> [48]	2017	8 beams irregular	~110	Diesel engine	Near 2200.5	1	

Table 2.1: Summary of notable systems of LAS tomography for combustion analysis.

2.5.2 Ill-posed Inverse Problem of LAS Tomography

Deployment of beams around the measurement target is limited by various factors, including the physical dimensions of the collimators and receivers, as well as the constraints imposed by the optical access to the measurement target. These limitations restrict the number of beams that can be effectively utilised for measurements. Additionally, the dynamic nature of flame places requirements on the temporal resolution of measurements and renders methods with slow mechanical beam scanning impractical. Hence the number of path-integrated absorption measurements is usually less than the number of unknowns, resulting in under-sampling and inherent ill-posed problem in the inverse problem described in Equation 2.43. Previous studies have adopted a mathematical approach, specifically SVD, to analyse the ill-posed problem in LAS tomography [50; 51]. A brief review is provided here for convenience.

The sensing matrix \mathbf{L} can be illustrated through SVD as:

$$\mathbf{L} = \mathbf{U}\delta\mathbf{V}^T, \quad (2.44)$$

where $\mathbf{U} \in \mathbb{R}^{Z \times Z}$ and $\mathbf{V} \in \mathbb{R}^{N \times N}$ are orthonormal matrices and $\delta \in \mathbb{R}^{Z \times N}$ a diagonal matrix containing the singular values in descending order.

In principle, the inverse problem aims at finding a unique solution, $\mathbf{b}^{\text{LS}} \in \mathbb{R}^{1 \times N}$ to minimise the least-square error, that is, $\mathbf{b}^{\text{LS}} = \arg \min(\|\mathbf{L}\mathbf{b} - \mathbf{B}\|_2^2)$. When $Z > N$, this solution can be calculated by

$$\mathbf{b}^{\text{LS}} = \sum_{n=1}^N \frac{\mathbf{u}_n^T \mathbf{B}}{\sigma_n} \mathbf{v}_n, \quad (2.45)$$

where \mathbf{u}_n and \mathbf{v}_n are the n^{th} column vectors of \mathbf{U} and \mathbf{V} , respectively. σ_n is the n^{th} singular value in the diagonal δ .

As mentioned previously, the number of laser beams Z is limited by optical access to the combustors, resulting in $Z < N$. In this case, \mathbf{b}^{LS} in Equation 2.45 should be separated into two parts, described in Equation 2.46: the unique solution $\mathbf{b}^{\text{unique}} \in \mathbb{R}^{1 \times N}$ that gives the minimised value of $\|\mathbf{L}\mathbf{b} - \mathbf{B}\|_2^2$ satisfying $\mathbf{L}\mathbf{b} = \mathbf{B}$, and the non-unique solution $\mathbf{b}^{\text{null}} \in \mathbb{R}^{1 \times (N-Z)}$ from solving $\mathbf{L}\mathbf{b} = 0$.

$$\mathbf{b}^{\text{LS}} = \mathbf{b}^{\text{unique}} + \mathbf{b}^{\text{null}}. \quad (2.46)$$

Considering the practical measurements \mathbf{B} is a superposition of noise-free data, \mathbf{B}^{true} , and the noise, $\mathbf{B}^{\text{noise}}$, hence $\mathbf{b}^{\text{unique}}$ can be expressed by

$$\mathbf{b}^{\text{unique}} = \sum_{n=1}^Z \frac{\mathbf{u}_n^T \mathbf{B}^{\text{true}}}{\sigma_n} \mathbf{v}_n + \sum_{n=1}^Z \frac{\mathbf{u}_n^T \mathbf{B}^{\text{noise}}}{\sigma_n} \mathbf{v}_n. \quad (2.47)$$

Since \mathbf{B} is rank-deficient, the lack of $N - Z$ measurements causes nontrivial null-space in \mathbf{L} , thus leading to $N - Z$ undetermined values in \mathbf{b}^{null} . Hence, Equation 2.45 can be further expanded as:

$$\mathbf{b}^{\text{LS}} = \sum_{n=1}^Z \frac{\mathbf{u}_n^T \mathbf{B}^{\text{true}}}{\sigma_n} \mathbf{v}_n + \sum_{n=1}^Z \frac{\mathbf{u}_n^T \mathbf{B}^{\text{noise}}}{\sigma_n} \mathbf{v}_n + \sum_{n=Z+1}^N c_n \mathbf{v}_n, \quad (2.48)$$

where $\mathbf{c} \in \mathbb{R}^{1 \times (N-Z)}$, with the n^{th} element c_n , is a set of undetermined scalars to describe \mathbf{b}^{null} .

Equation 2.48 mainly suffers from:

- (a) Noise susceptible. As indicated by the second term in Equation 2.48, $\mathbf{B}^{\text{noise}}$ can be significantly magnified with relatively small singular values σ_n , worsening the quality of the reconstructed images.
- (b) Solution underdetermined. In the case of $Z < N$, the singular value does not exist for $n > Z$. The third term in Equation 2.48 is the indicator of undetermined solutions. The larger the $N - Z$ is, the more severely undetermined solution.

2.6 Image Reconstruction Algorithms

To address the ill-posed problem discussed earlier, a wide range of algorithms have been developed and thoroughly investigated in previous literature. Detailed reviews of these algorithms are also available in the existing literature [11; 52; 53]. In this section, a concise overview of these algorithms will be provided. The summary of them is shown in Table 2.2.

2.6.1 Filtered Back-Projection

The Filtered Back-Projection (FBP) is a widely used algorithm in tomographic reconstruction. Due to its non-iterative nature, the FBP algorithm offers the advantage of fast calculation for solving the inverse problem. However, the practical implementation of LAS tomography presents challenges in obtaining sufficient number of projections with equiangular and complete sampling, which is a requirement for the successful implementation of the FBP algorithm. As a result, the FBP algorithm is often utilised to provide an initial estimation for the subsequent stages of the calculation, rather than obtaining the reconstruction results.

FBP algorithm is based on the central slice theorem, which is also the fundamental of linear tomography. As illustrated in Figure 2.9 [54], it states that the Fourier transform of a projection at a specific angle is equivalent to a single slice of the 2D Fourier transform of the object at that same angle. In the context of LAS tomography, the projections of the object to be reconstructed are obtained by the Radon transform:

$$P_{\vartheta}(g) = \int_{L_z} f(x,y) dL_z, \quad (2.49)$$

where $P_{\vartheta}(g)$ is the projection taken at angle ϑ and located at a distance g from the origin. The distribution being reconstructed is represented by $f(x,y)$. $P_{\vartheta}(g)$ is calculated via integration along the light path L_z .

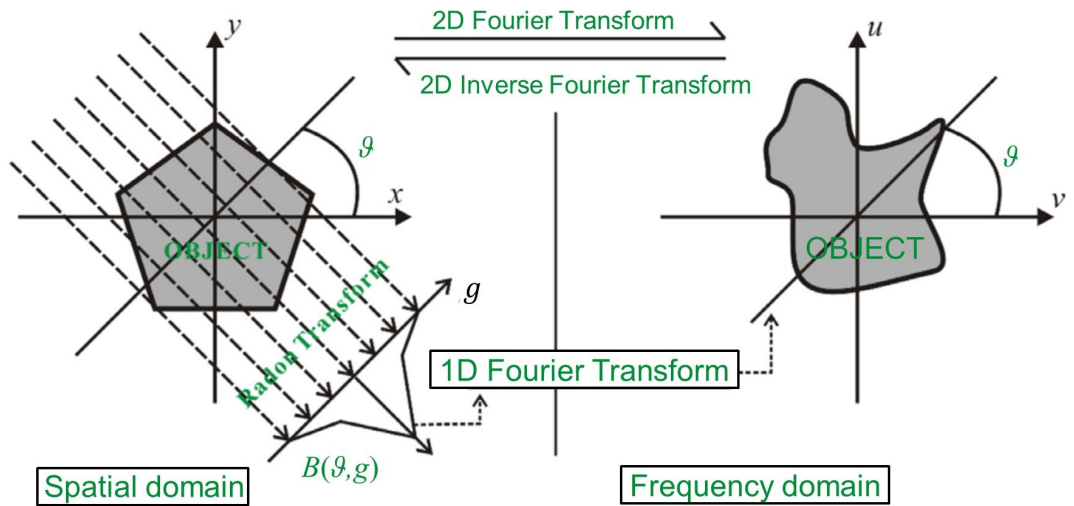


Figure 2.9: Illustration of the central slice theorem and the FBP algorithm. The left panel defines the Radon transform and the right panel shows the sinogram in the Fourier space.

Then the representation of the object in the frequency domain is obtained by taking the Fourier transform of each projection sequentially and organising the results into a 2D map. Then the reconstruction is conducted simply via inverse Fourier transform of the 2D map in the frequency domain. However, there is a constraint in capturing the full-frequency information with finite line-of-sight measurements, resulting in the amplification of low-frequency components during the inverse Fourier transformation. This amplification leads to image blur, even in the absence of noise in the measured projections. To overcome this challenge and enhance the quality of the reconstruction, additional filtering is incorporated. The process can be expressed mathematically as follows:

$$f(x, y) = \underbrace{\int_0^\pi \underbrace{\int_{-\infty}^{+\infty} \underbrace{P_\vartheta(g) e^{-i2\pi\omega t}}_{\text{FT of a projection}} dg}_{\text{inverse FT}} |w_{\text{filter}}| e^{i2\pi\omega t} d\omega d\vartheta}_{\text{back-projection}}, \quad (2.50)$$

where ω is a real number, defined in the frequency domain after Fourier transform, $t = x \cos \vartheta + y \sin \vartheta$. w_{filter} the ramp filter used to remove blurring.

2.6.2 Iterative Algorithms

The inverse problem of the LAS tomography stated in Equation 2.43 can be formulated as a simple least-square problem as follows:

$$\arg \min_{\mathbf{b}} \|\mathbf{B} - \mathbf{Lb}\|_2^2. \quad (2.51)$$

The optimal solution of \mathbf{b} can be approached iteratively. Two of the most commonly used algorithms Algebraic Reconstruction Technique (ART) and Landweber algorithm are detailed reviewed in this section.

Algebraic Reconstruction Technique

The ART is widely recognised for its ability to address the ill-posed nature of tomographic problems encountered in combustion applications. This algorithm offers several advantages, including:

1. Robust to noise
2. Reconstruction from limited measurements, which is particularly beneficial in scenarios where obtaining a large number of projections is challenging

3. Accommodate projections with varying geometries and less projection angle.

A mathematical expression of the ART algorithm can be given by

$$\mathbf{b}_{i+1} = \mathbf{b}_i + \lambda_{\text{ART}} \rho_z \frac{B_z - \langle \rho_z, \mathbf{b}_i \rangle}{\langle \rho_z, \rho_z \rangle}, \quad (2.52)$$

where \mathbf{b}_i is the estimated solution at the i^{th} iteration. λ_{ART} is a relaxation factor that controls the convergence rate. $\langle \cdot, \cdot \rangle$ denotes the inner product operation. B_z is the measured path-integrated absorption of the z^{th} beam. ρ_z the z^{th} row of the sensing matrix $\mathbf{L}_{z,n}$.

Several variants of the ART algorithm have been developed, including multiplicative algebraic reconstruction technique, simultaneous algebraic reconstruction technique, and simultaneous iterative reconstruction technique. Those variants modify the update scheme at each iteration, resulting in different properties and benefits in increasing iteration speed and noise resistance. A detailed comparison is given by Jeon *et al.* [55].

Landweber Algorithm

The Landweber algorithm is also commonly used in LAS tomography. As this algorithm enables the constraint from external operators to reinforce the reconstruction, it is suitable in scenarios with few available line-of-sight measurements and challenging environments [56]. However, similar to the ART algorithm, it is prone to semi-convergence. This issue can be addressed by establishing suitable termination criteria to improve convergence.

The mathematical expression is given by:

$$\mathbf{b}_{i+1} = \Theta[\mathbf{b}_i + \lambda_L \mathbf{L}^T (\mathbf{B} - \mathbf{L} \mathbf{b}_i)], \quad (2.53)$$

where the subscript i indicates the index of the current iteration. λ_L is the relaxation factor to control the convergence rate. and Θ is an operator that enforces additional constraints, such as the non-negativity of the pixel values.

The initial guess \mathbf{b}_0 can be obtained via the linear back-projection operation, i.e. $\mathbf{b}_0 = \mathbf{L}^{-1} \mathbf{B}$. Considering the sensing matrix is rank deficient for LAS tomography, the transpose of the sensing matrix, \mathbf{L}^T , is used to approximate the \mathbf{L}^{-1} .

2.6.3 Regularisation

Another approach to solving the ill-posed and underdetermined inverse problem is to add a regularisation to the least-square problem in Equation 2.51. The cost function in LAS tomography typically comprises two components: the data fidelity term, which quantifies the discrepancy between the path-integrated absorption measurements \mathbf{B} ; and the back-projected image $\mathbf{L}\mathbf{b}$, and the regularisation term, which penalises solutions that exhibit undesirable properties:

$$\arg \min_{\mathbf{b}} \|\mathbf{B} - \mathbf{L}\mathbf{b}\|_2^2 + \epsilon \mathbf{W}(b), \quad (2.54)$$

where $\mathbf{W}(b)$ is the regularisation term built based on the prior knowledge for the unknown distribution \mathbf{b} . ϵ is the regularisation weight.

Regularisation is used for two reasons:

1. The regularisation term plays a crucial role in enforcing regularity in the reconstruction process, effectively suppressing unwanted noise components and making the resulting image less sensitive to noise.
2. The regularisation term incorporates prior knowledge about the distribution being reconstructed, which can enhance spatial resolution and reduce reconstruction errors by guiding the algorithm toward a more accurate solution.

Some commonly used regularisation methods are reviewed in this section.

Smoothness

Considering the distribution of the gas property is continuous in reality, the smoothness can be posted as prior knowledge to regularise the reconstruction of the inverse problem [57]. This can be formulated as

$$\mathbf{W} = \|\mathbf{F}\mathbf{b}\|_2^2, \quad (2.55)$$

where the matrix \mathbf{F} can be an identity matrix that gives the standard (0^{th} order) Tikhonov regularisation. It can also be a differential operator to enforce the smoothness of the reconstructed image which is also known as l_2 regularisation.

Sparsity

Sparsity of the distribution means that even though a total of N values are required to fully represent the field, some of the values are essentially zeros or very small. Hence a reduced number of values are sufficient to describe the field [58]. An application of this is on reconstructing uniform temperature distribution with a specific shape. For instance, in flame generated by a flat flame burner, the temperature distribution exhibits an almost negligible gradient. In this case, l_1 regularisation or Total variation (TV) is used. For l_1 the regularisation term is

$$\mathbf{W} = \|\mathbf{F}\mathbf{b}\|_1, \quad (2.56)$$

where the regularisation matrix \mathbf{F} is the identity matrix with prior knowledge of the target distribution.

TV regularisation is define as

$$\mathbf{W} = \sum_{x=1}^{N_x} \sum_{y=1}^{N_y} \sqrt{(b_{x,y} - b_{x+1,y})^2 + (b_{x,y} - b_{x,y+1})^2}, \quad (2.57)$$

where N_x and N_y are side lengths in pixels for the x and y axis, respectively. (x,y) denotes the coordinate of the pixel. $b_{x,y}$ is the unknown to be solved in that pixel.

Relative Entropy Tomographic Reconstruction

Introduced in Section 2.4.3, temperature retrieval requires the measurements of two spectral features. Solving two linear inverse problems for the absorption distribution for each spectral feature is inevitable. Noise in the retrieved absorption distributions, particularly in the denominator of the Equation 2.38, propagates into the ratio $R(t)$ and generates spike noise in the temperature image. The Relative Entropy Tomographic RecOnstruction (RETRO) can balance penalty on a wide range of ratios while maintaining convex to guarantee a unique solution [59]. The regularisation term is given by

$$\mathbf{W}(b_{v_1}, b_{v_2}) = \begin{cases} (b_{v_2} + b_{v_1}) \bullet \log(1 + b_{v_2}/b_{v_1}) & \text{if } b_{v_2}, b_{v_1} > 0 \\ 0 & \text{if } b_{v_1} = 0 \text{ or } b_{v_2} = 0 \\ +\infty & \text{otherwise} \end{cases}, \quad (2.58)$$

where v_1 and v_2 in subscript denote the two transitions used to perform ratio thermometry.

2.6.4 Data Driven Methods

Advancements in machine learning and neural networks have indeed facilitated the development of data-driven methods for LAS tomographic reconstruction. These methods leverage extensive training data to learn patterns and relationships within the data, allowing for improved reconstruction quality. The incorporation of prior knowledge into the reconstruction process helps address the ill-posed nature of the tomographic reconstruction.

In the context of LAS tomographic reconstruction, there are various approaches based on data-driven methods. Some of these approaches rely on the assumption of a Gaussian distribution for the gas properties. Yu *et al.* and Huang *et al.* demonstrated the use of ELM and CNN models, respectively. Their models were trained on data with a Gaussian assumption to reconstruct distributions of temperature and species concentration. These approaches have shown promising results in terms of reconstruction accuracy. Recently, more complex architectures, such as dual-branch auto-encoders, named Y-net [60] and transformers [61], have been introduced to address non-linear LAS tomographic problems. These models have achieved improved reconstruction accuracy compared to conventional methods. These advancements highlight the potential of using more sophisticated models to capture the non-linearities in gas properties' distributions.

While the Gaussian assumption has been widely used due to its simplicity, it cannot fully capture the complexity of gas properties' distributions in practical combustion scenarios. To address this limitation, researchers have explored alternative approaches, including using CFD methods to generate training datasets that better approximate the distributions of gas properties in reality. For example, Si *et al.* [62] trained a Long Short-term Memory (LSTM) model using training datasets generated by Large Eddy Simulation (LES). This approach allows for a more realistic representation of the gas properties' distributions in combustion scenarios. The authors validated the reconstruction performance of their model using measurements from a lab-scale circular burner, demonstrating the effectiveness of the approach in capturing complex

distribution features. Similarly, Molnar *et al.* [63] implemented a Physical Informed Neural Network (PINN) based on Direct Numerical Simulation (DNS) data. By leveraging the detailed information provided by DNS, their network achieved convincing results in capturing complex features of gas properties.

Training data based on experimental measurements also plays a significant role in data-driven methods for LAS tomographic reconstruction. Shui *et al.* [64] applied Dictionary Learning (DL) to measurements of diesel engine exhaust. This approach utilised experimental measurements to reconstruct the gas properties' distributions, providing insights into real-world combustion diagnosis.

It is worth mentioning that the current data-driven method is limited in generalisation due to lacking ground truth for training. Researchers continue to explore and develop new techniques and methods for LAS tomographic reconstruction, aiming to improve the accuracy and reliability of reconstructing gas properties' distributions in complex combustion processes.

Category	Methods	Example reference	Year	Merits	Limitation
Non-iterative	FBP	Ulrich <i>et al.</i> [65]	2016	<ul style="list-style-type: none"> • Incorporated filter • Faster than iterative 	<ul style="list-style-type: none"> • Require Large number of projections • Require equiangular projections
Iterative	ART	Sun <i>et al.</i> [66]	2017	<ul style="list-style-type: none"> • Robust to noise • Require less beams 	<ul style="list-style-type: none"> • Semi-convergent • Slow
	Landweber	Liu <i>et al.</i> [56]	2015	<ul style="list-style-type: none"> • Initial from back-projection • Flexible 	<ul style="list-style-type: none"> • Semi-convergent • Slow
Regularisation	Smoothness	Niu <i>et al.</i> [57]	2022	<ul style="list-style-type: none"> • Physical nature • Robust to noise 	<ul style="list-style-type: none"> • Trade-off precision
	Sparsity	Cai <i>et al.</i> [58]	2013	<ul style="list-style-type: none"> • Considering sparsity • Reduce unknowns 	<ul style="list-style-type: none"> • Difficult to model • Require prior heavily
	RETRO	Bao <i>et al.</i> [59]	2020	<ul style="list-style-type: none"> • Mitigate overshoot 	<ul style="list-style-type: none"> • Require two laser transition
Category	Main models	Example reference	Year	Training dataset	Application
Data-driven	ELM	Yu <i>et al.</i> [15]	2018	Gaussian phantoms	Gaussian phantoms
	CNN	Huang <i>et al.</i> [67]	2018	Gaussian phantoms	Gaussian phantoms
	Y-net	Wang <i>et al.</i> [60]	2022	Gaussian phantoms	Gaussian phantoms
	Transformer	Si <i>et al.</i> [61]	2022	Gaussian phantoms	Gaussian phantoms
	U-net	Chen <i>et al.</i> [60]	2022	Gaussian phantoms	Explosive fireball simulator
	LSTM	Si <i>et al.</i> [62]	2023	LES simulation	Circular burner
	PINN	Molnar <i>et al.</i> [63]	2022	DNS simulation	DNS simulation
	DL	Shui <i>et al.</i> [64]	2021	Experiment data	Diesel engine exhaust

Table 2.2: Summary and comparison between algorithms used for LAS tomography.

2.7 Summary

This chapter offered a concise overview of the physical principles underlying LAS, including Beer-Lambert law and broadening mechanisms. The typical LAS techniques such as DAS, WMS and their fitting process were demonstrated. Compared to DAS, WMS diminishes the influence of low-frequency noise on measured absorption signals through the utilisation of signal modulation and demodulation techniques. Consequently, it is better suited for applications in environments with high levels of noise. The fundamentals of LAS tomography and notable LAS tomographic sensors were then introduced. The existing sensors grapple with considerable spacing between their adjacent beams, which in turn constrains the number of measurements accessible for reconstruction. The lack of measurement results in ill-posed problems during the reconstruction and artefacts in the results. To understand the ill-posed problem, the basics of SVD were briefly explained. Finally, an overview of reconstruction algorithms aimed at mitigating ill-posed problems in LAS tomography was presented.

Chapter 3

Modular LAS Tomographic Sensor

3.1 Introduction

Chapter 2 has discussed the advantages of the parallel beam arrangement in LAS tomographic systems. The uniform sampling of the RoI can minimise the effect of under-sampling and data gaps which result in reconstruction artefacts. This characteristic is particularly valuable when there is limited knowledge about the target's specific features or characteristics.

Previous research has reported the effective implementation of sensors that employ a parallel beam arrangement, achieving a beam spacing of only a few centimetres. However, the further reduction in beam spacing is hindered by the physical dimensions of fibre optics and PhotoDiode (PD), therefore, limiting the potential improvement in the spatial resolution of the tomographic system. Another challenge lies in the specialised nature of existing implementations, which are often customised for specific applications. This customisation incurs significant costs related to the adaptation of optical mechanics, making it difficult to commercialise LAS tomographic sensors for diverse combustion systems.

To address these issues, this chapter presents a miniature and modular design for both the emitter and receiver in the LAS tomographic system. This design enhances spatial resolution and improves the versatility of LAS tomographic sensors. The key contributions of the proposed design can be summarised as follows:

1. **Flexibility:** The modular design increases the system's flexibility with 1 cm beam spacing, enabling its utilisation in various research and application scenarios.
2. **Robustness:** The modular design facilitates easy transportation, assembly, maintenance, and replacement of the tomographic system, making it well-suited for challenging environments.

3. Cost-effectiveness: By utilising off-the-shelf components, the sensor's cost is significantly reduced, enhancing its practicality and accessibility.

3.2 Architecture of LAS Tomographic System

The structure of a tomographic system can be summarised by the block diagram depicted in Figure 3.1.

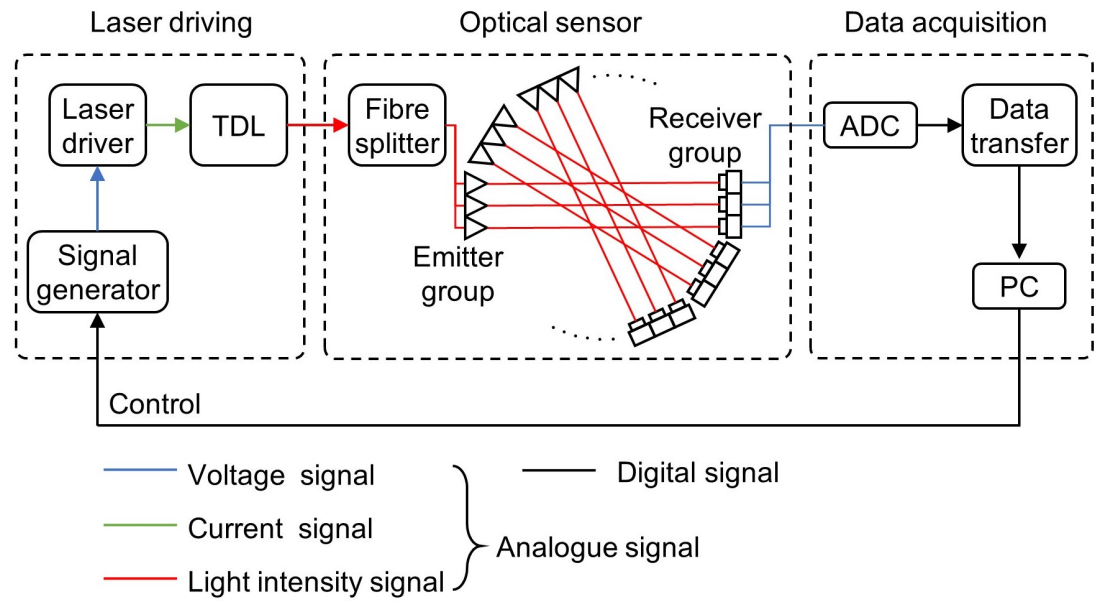


Figure 3.1: Block diagram of LAS tomographic system.

Generally, a LAS tomographic system comprises three essential parts: laser driving, optical sensor, and data acquisition. This section will systematically introduce these components and elucidate how the signal is transmitted between them. Utilising this structure, an initial venture into modular sensor design has led to the development of a 32-channel lab-scale LAS tomographic system. This system incorporates a parallel beam arrangement and is specifically designed to measure temperature and H_2O concentration. Figure 3.2 visually outlines this system. Subsequently, this system is utilised as a case study for detailed explanations.

Laser Driving

Laser driving plays a crucial role in generating laser light at a specific wavenumber range that encompasses the absorption feature of interest. The system comprises three key elements: the signal generator, the laser driver, and the TDL.

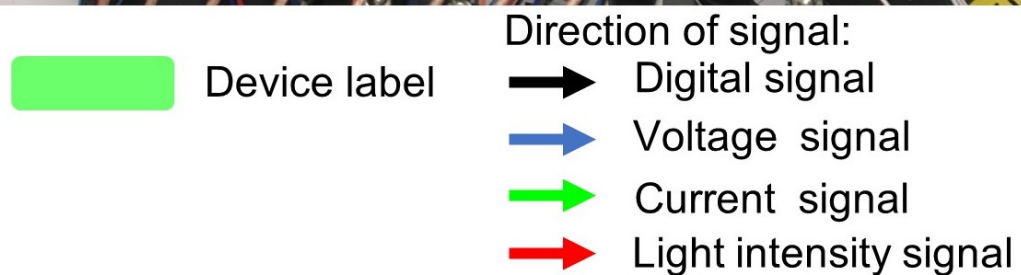
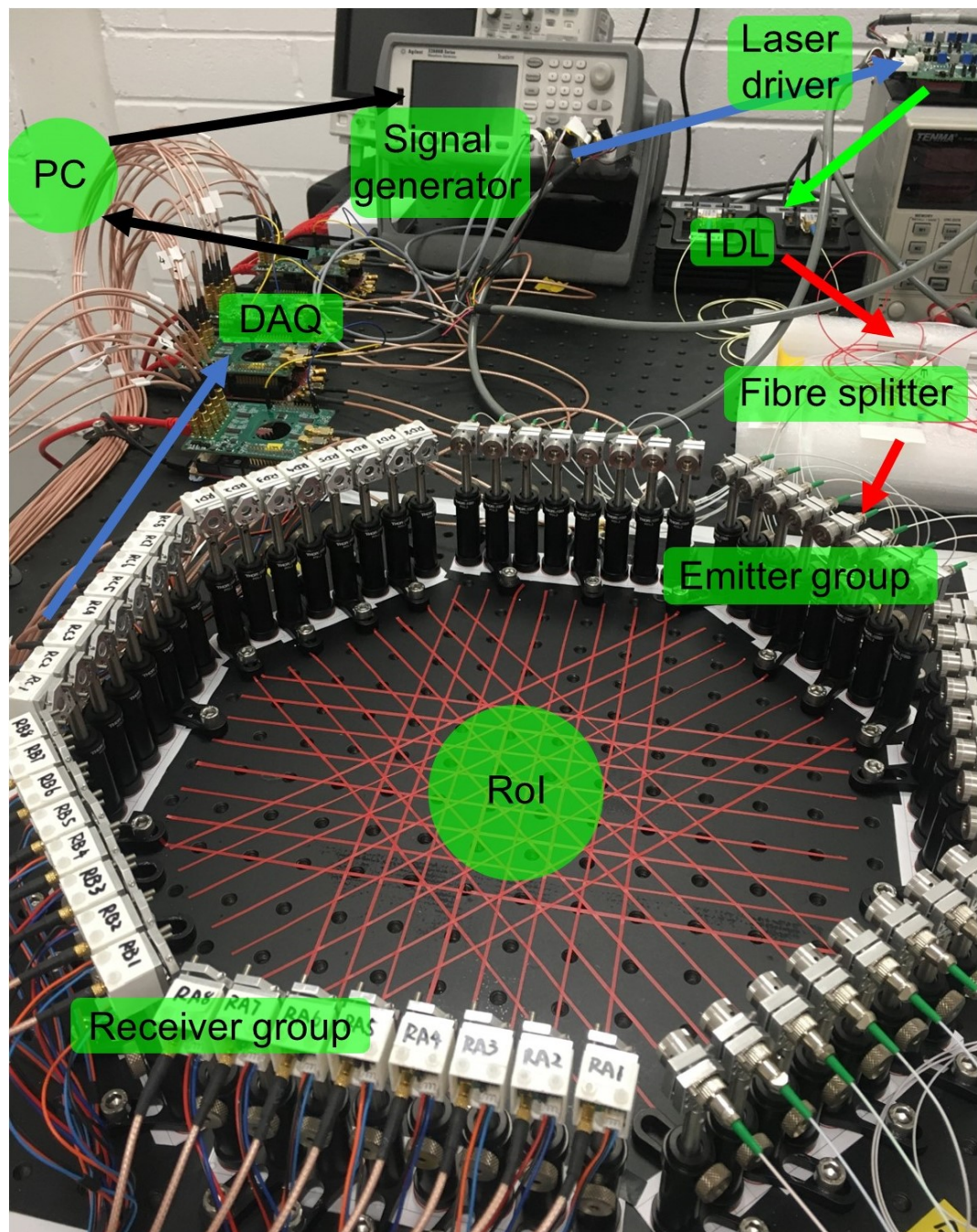


Figure 3.2: 32-channel lab-scale LAS tomographic system prototype.

As shown in Figure 3.1, the signal generator generates a high-frequency voltage signal based on the control signal provided by the computer. This voltage signal serves as the input for the laser driver. The laser driver, in turn, converts the voltage signal into a current signal with modulation that is suitable for driving the TDL. In the context of implementing WMS, laser drivers ensure that TDLs operate with the desired modulation and rapid tuning capability [68]. The TDL is the core component of laser driving. It is driven by the modulated current from the laser driver, resulting in the emission of laser light with the desired wavenumber tuning. The intensity of the incident light produced by the TDL is determined by the power of the TDL itself. This power level significantly influences the overall performance and effectiveness of the LAS tomographic system.

In Figure 3.2, to implement the laser driving, the control signals with different modulation frequencies are generated by the Keysight 33522B signal generator [69] and fed to two Wavelength Electronics LDTC 2-2 E laser controllers [70], respectively. The NEL NLK1E5EAAA and NLK1E5GAAA DFB laser diodes [71; 72], receive the drive current and generate two lasers for scanning the line pair of H_2O at 7185 cm^{-1} and 7444 cm^{-1} , respectively. The different modulation frequencies facilitate the Frequency Division Multiplexing (FDM) [46]. The FDM light is then passed to the optical sensor.

Optical sensor

Optical sensors are designed with the purpose of conducting multi-channel line-of-sight measurements. Laser beams are carefully positioned to ensure coverage of the designated area where the target is situated. This system can be further dissected into three key components: light distribution, emitters, and receivers.

When performing measurements with multiple wavenumbers, the light distribution involves the use of a fibre coupler before the splitter to merge the light intensity from various TDL's outputs. Then, the combined intensity signal is divided into multiple beams by the fibre splitter to facilitate multi-channel detection. However, the emitted beam from the optical fibre typically exhibits a large divergence angle, which poses challenges for long-distance transmission. To overcome this limitation, a collimator is installed after the beam splitter output to collimate the light and improve its transmission characteristics.

As shown in Figure 3.2, to implement the 32-channel optical path layout, the laser outputs from the diodes are combined using a fibre coupler (Opneti Single Mode Standard Coupler [73]) and then split into 32 channels using a fibre splitter (Opneti 1x N PLC Splitter [74]). Each fibre output is collimated using a Thorlabs CFC5-C Adjustable Aspheric Collimator [75]. A customised optomechanical mount is designed to hold the collimator and to provide some adjustment flexibility.

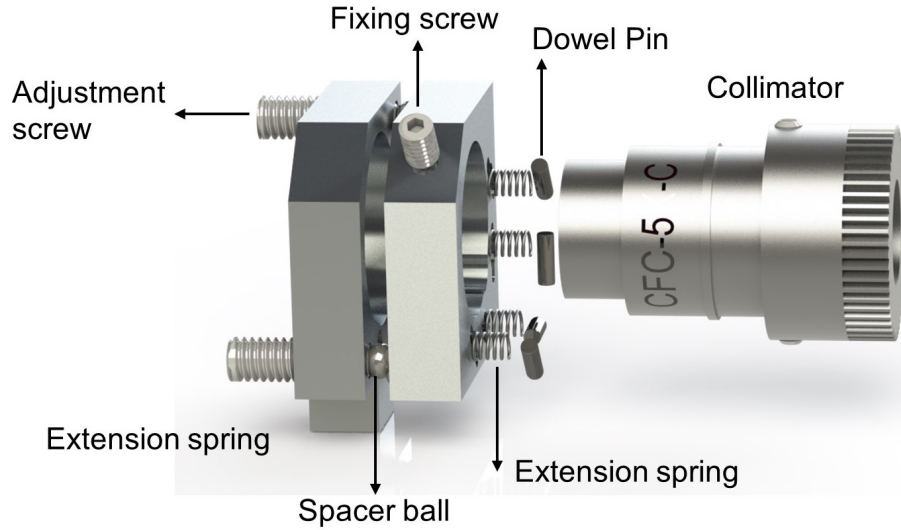


Figure 3.3: Breakdown view of the emitter.

A model view of the collimator and mount is given in Figure 3.3. The Thorlabs CFC5-C is fixed via a screw on the front plate. Then the front plate is attached to the back plate via spring extension force. A 2 mm diameter stainless steel ball is placed between two plates as a spacer. By adjusting the screw at the back plate, the gap between the two plates varied, creating a change in the direction of the emitted laser beam.

Once the light passes through the RoS, the resulting transmitted intensity signal is captured by a photodetector board. The board consists of a photosensitive component, such as a PD, which generates current upon absorbing photons. However, the current produced by the PD is usually too weak to be directly detected by the data acquisition. To overcome this limitation, TransImpedance Amplifiers (TIA) are commonly employed. These amplifiers serve a dual purpose by converting the weak current signals from the PD into corresponding voltage signals and amplifying the signals to enhance their strength. The amplification provided by the TIA improves the signal's resistance to noise. The circuit diagram of a typical TIA circuit is depicted in Figure 3.4

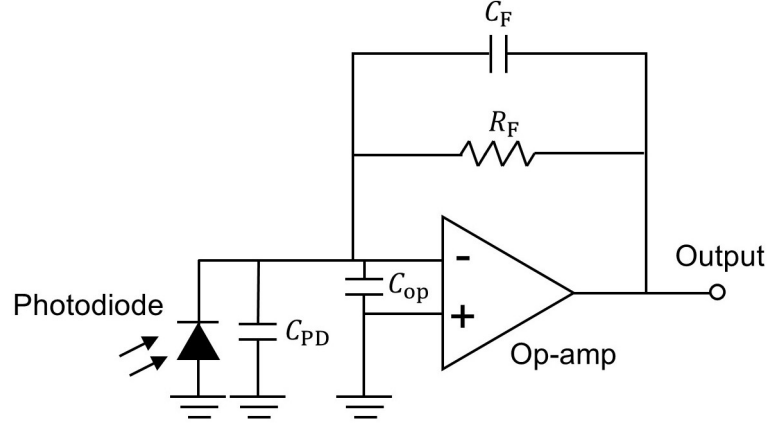


Figure 3.4: Circuit diagram of TIA.

Where C_{PD} is the PD's capacitance. C_{op} is the input capacitance of the operational amplifier (op-amp). R_F is the amplifying resistance deciding the voltage gain and C_F is the compensating capacitance.

In Figure 3.2, the photodetector uses Hamamatsu G12182 PD [76] to convert the light intensity to the current signal. The PD's current output is then converted to a voltage signal and amplified by a customised TIA circuit that utilises the AD8065 op-amp [77]. The TIA circuit includes an adjustable gain resistor to accommodate various amplification requirements and a 10pf capacitor for compensating. A 4mm focus lens is applied in front of the PD to maximise the light recipient. The receiver mount and the TIA circuit are shown in Figure 3.5. Similar to the adjustment mechanism on the emitting side, two set screws are used to adjust the angle of the focus lens. The circuit is fixed and protected by the PCB shell.

The 32 modular emitter-receiver pairs are arranged to project from four equiangular directions, with a beam spacing of 1.6 cm. It is worth noting that, the physical dimensions of the collimators and photodetector are key factors in determining the beam spacing for systems employing parallel beam arrangements. Meanwhile, the size of the photodetector cannot be arbitrarily reduced or modified beyond certain dimensions, because it is constrained by the standard packages available for both the op-amp chip and the PD.

Data acquisition

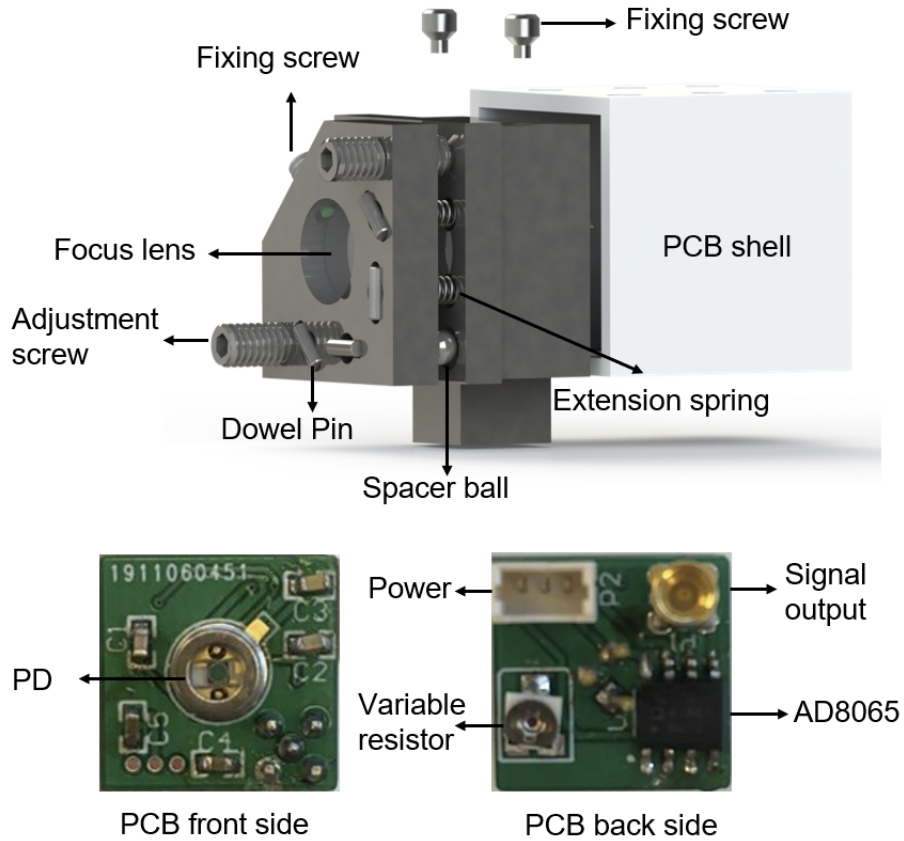


Figure 3.5: Breakdown view of the receiver.

The data acquisition converts the analogue signal output from the photodetector into a digital signal that can be processed by computers. The quality of the signal collected by the data acquisition is influenced by two key factors: the sampling rate and quantisation level of the Analogue-to-Digital Converter (ADC).

The sampling rate of the ADC determines how frequently the analogue signal is sampled and converted into a digital value. The insufficient sampling rate may cause the system to miss rapid variations in the analogue signal, including high-frequency components, resulting in a loss of information and a reduction in the SNR. On the other hand, selecting a high sampling rate also increases the data load during the data transfer, which may not always be desirable.

Quantisation levels decide how fine the digital system digitises the analogue signal at each sample within the range starting from the lowest possible sample value up to the highest. A higher quantisation level allows for a more accurate representation of the analogue signal, enhancing both the SNR and the measurement accuracy [78]. However, higher quantisation levels also give rise to a larger data load, which can present difficulties during the subsequent data transfer.

In realizing the data acquisition for the system depicted in Figure 3.2, a Signal Conditioning (SC) board [79] is employed alongside the commercially accessible Red Pitaya (RP) lab-on-chip system [80]. This system incorporates a quantisation level of 2^{14} and allows a sampling rate of up to 125 Mega samples per second. Such an arrangement facilitates near-parallel acquisition of WMS signals from the 32 channels and rapid data transfer through an ethernet cable.

3.3 Evaluation of the Lab-scale Tomographic System

As the system comprises various subsystems, attention must be given to their collaboration. To ensure that the LAS tomographic system collects reliable and processable signals, it is necessary to consider two important indicators, namely bandwidth and linearity, during the design.

Bandwidth

In this context, bandwidth refers to the upper threshold at which electronic devices can respond to high-frequency components without experiencing notable attenuation. Typically, when a device exhibits a -3dB amplitude reduction at a particular frequency, that frequency is identified as the -3dB bandwidth (f_{-3dB}) of the device. For off-the-shelf devices, the bandwidth specifications are available in their datasheets. However, for custom circuits, the bandwidth can be determined through either calculation or testing.

For example, the f_{-3dB} bandwidth of the TIA circuit shown in Figure 3.4 can be estimated via Equation 3.1 [81]:

$$f_{-3dB} = \sqrt{\frac{GBW}{2\pi(C_{PD} + C_{op})R_F}}, \quad (3.1)$$

where GBW the gain bandwidth of the op-amp.

Different stages of the LAS tomographic system have varying bandwidth requirements. In laser driving, the WMS technique involves generating an incident light signal with high-frequency modulation. To maintain the amplitude of the high-frequency modulation, the input and output bandwidth of each subsystem in the laser driving should exceed the modulation frequency. Considering the WMS technique's focus on analysing the high-frequency components of the laser absorption signal, the bandwidth requirement on the receiving and acquisition side is determined by the target frequency components. As higher-frequency components typically have smaller amplitudes, an inadequate bandwidth in the photodetector and ADC can diminish the amplitude of the high-frequency component, making the high-frequency absorption signal more susceptible to noise [82].

For example, the rated bandwidths of equipment in Figure 3.2 are depicted in Table 3.1.

Devise	Signal generator	Laser driver	Laser diode	Photodetector	ADC
Bandwidth	30 MHz	1.6 MHz	10 MHz	3 MHz	50 MHz

Table 3.1: Bandwidth of components in example LAS tomographic system.

Concerning laser driving, the maximum modulation frequency is constrained by the minimum bandwidth among the signal generator, laser driver, and TDL, which stands at 1.6 MHz. On the detection front, the bandwidth is capped at 3 MHz by the TIA circuit. When contemplating the incorporation of $2f/1f$ -WMS, a 1.6 MHz modulation signal from the laser driving results in a $2f$ frequency of 3.2 MHz. The bandwidth of the TIA falls short of the intended $2f$, thereby necessitating a reduction in the modulation frequency.

Linearity

The nonlinear response of the diode device in the LAS tomographic system can introduce distortion in the measured absorption signal, directly impacting the accuracy of measurement. As the quantitative characterisation of that nonlinear response is challenging, it is essential to design the system operating predominantly in the linear region to minimise nonlinearity. Chapter 2 provides a comprehensive discussion on

the calibration of the wavenumber-time relationship using an interferometer, which addresses the nonlinearity caused by current modulation and wavenumber modulation to TDLs. In the present chapter, the emphasis shifts towards the evaluation of the linearity of the PD.

Ideally, maximising the incident light intensity is desirable as it reduces the percentage of ambient light, thermal radiation, and noise when photodetectors receive laser light. Moreover, a stronger light intensity elicits a more robust current response in the PD, thereby improving the overall SNR. However, the sensitivity of the PD to light intensity is not uniformly consistent. Figure 3.6 illustrates this non-uniform sensitivity.

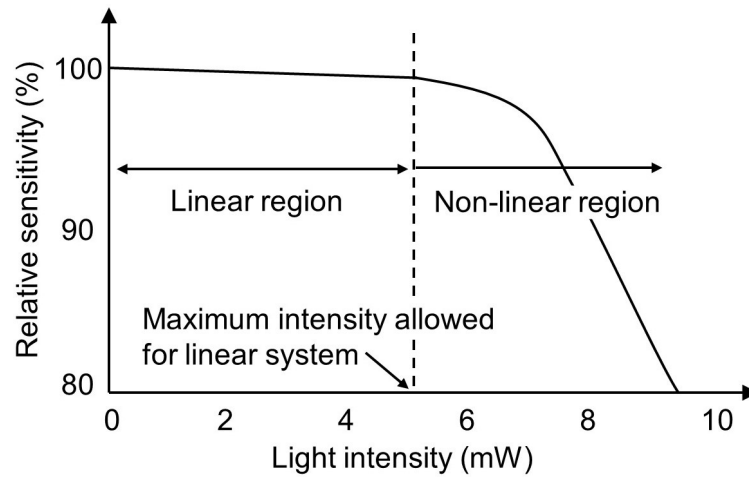


Figure 3.6: Example of PD's sensitivity to light intensity.

At low light intensities, the PD exhibits minimal changes in response to variations in the light intensity signal, remaining close to 100%. Hence, it can be regarded as a linear conversion of the light intensity signal into an electrical signal. However, when the light intensity surpasses a certain threshold, the PD's response to strong light intensity begins to unevenly decline. At this stage, the nonlinearity significantly affects the magnitude of the current signal converted by the PD [83]. Hence the maximum intensity to maintain linearity is constrained by the characteristics of PD.

To ensure the PD in the system illustrated in Figure 3.2 operates within its linear operational range, it is imperative to evaluate the light intensity reaching the PD. Considering that the two TDLs provide optical powers of 10 mW and 20 mW respectively, their combined effect yields a maximum light intensity of 30 mW. After distributing

this combined laser beam into 32 channels, the light intensity signal for each channel should not surpass 0.9 mW. The datasheet of the selected PD in Figure 3.7 contains relevant linearity data, affirming that the light intensity for each channel falls within the PD's linear operational range, ensuring a linear response in the received signal.

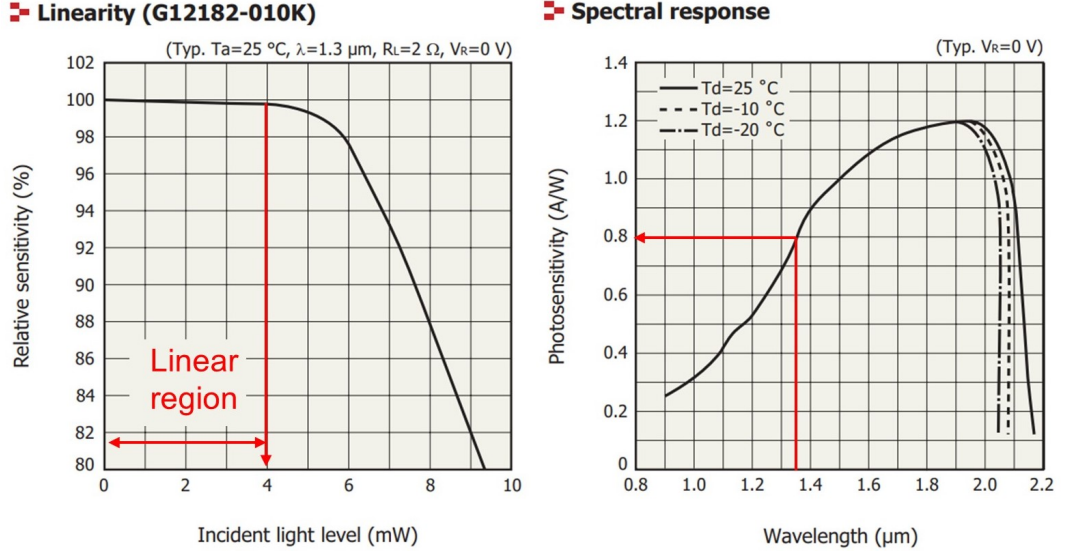


Figure 3.7: PD's characteristics adopted from data sheet.

Moreover, the PD is capable of converting a light intensity of 0.9 mW into a current signal of 0.72 mA around $1.35\text{ }\mu\text{m}$. With the amplification of up to 5,000 times, the signal output reaches 3.5 V, which is sufficient to ensure a good SNR in the subsequent data acquisition. When the amplification resistance is set to $5\text{ k}\Omega$, the bandwidth of the TIA circuit is calculated using Equation 3.1, yielding a value of 3 MHz. This indicates that the system can theoretically support a maximum modulation frequency of 1.5 MHz.

3.3.1 Test Results and Analysis

A lab-scale experiment has been conducted to validate the 32-channel sensor. In the experiment, each 2D distribution of H_2O concentration was generated by H_2O evaporation from a container filled with water at 60°C . In the first case shown in Figure 3.8, a larger container with 14 cm diameter was placed at the centre of the RoI. The second phantom was generated by placing a smaller container 8 cm in diameter both vertically and horizontally 2.1 cm away from the centre of the RoI. The cross-section of H_2O measurement was set 1 cm above the water surface. The temperature in the RoI was assumed to be uniform and was read from a thermal sensor [84] as

25°C for both cases. The square region at the centre of the sensing region with a side length of 12.8 cm was selected as the RoI to be reconstructed. The RoI was discretised into 12×12 pixels. The ART algorithm described in Section 2.6.2 was used for image reconstruction. Meanwhile, smoothness regularisation is also involved in the reconstruction to mitigate the ill-posed problems.

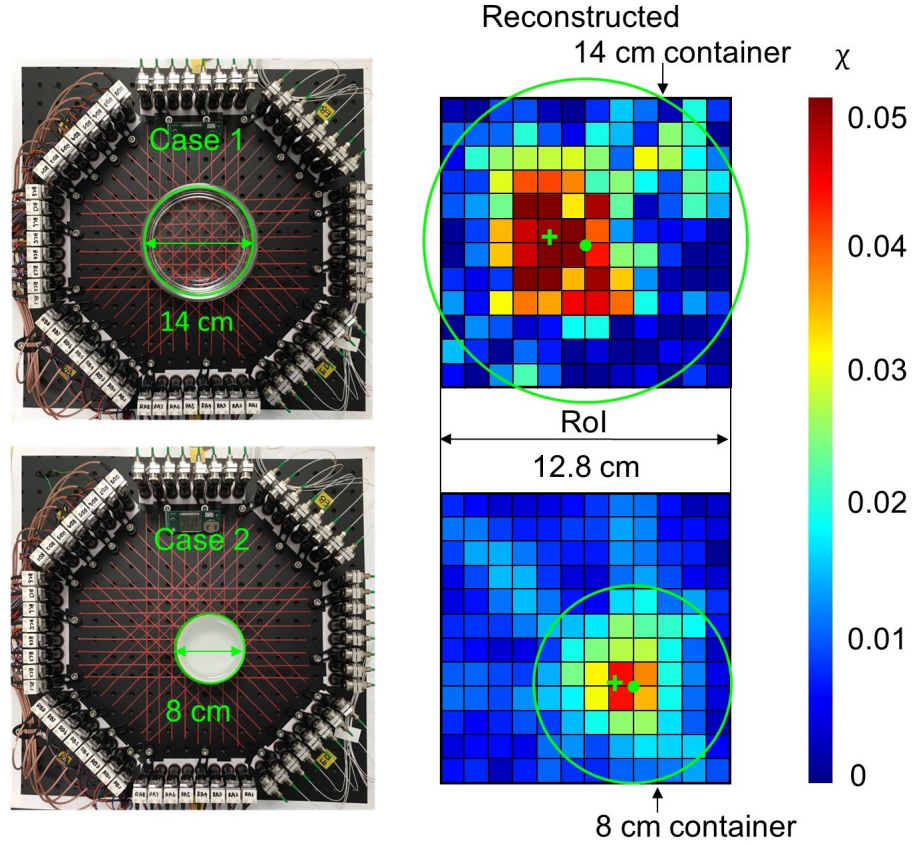


Figure 3.8: Experimental reconstruction of the 2D H_2O distributions with two experimental phantoms on the left and the reconstructed distributions on the right.

As shown in Figure 3.8, the reconstructed image for Case 1 effectively displays the distribution of H_2O during transpiration, exhibiting a high concentration at the centre and an irregular pattern throughout. The green cross, representing the centroid of the reconstructed water plume, is 3.4 mm vertically and 15.4 mm horizontally away from the container's centre marked by the green dot. This showcases a near match in positioning between the target and the reconstruction outcomes. However, it is challenging to identify any small-scale H_2O inhomogeneities, which are potentially introduced by transpiration. In case 2, the reconstructed images effectively depict the smaller-scale H_2O distribution with an accurate localisation, only 1.3 mm vertically

and 6.1 mm horizontally away from the centre of the container. However, the presence of severe blurring in the inhomogeneity is observed, which can be attributed to the smoothness regularisation applied during the reconstruction for mitigating ill-posed problems.

The reconstruction image exhibits low resolution overall, primarily as a result of the limited number of measurements acquired in each projection [85]. In the present system, only 8 measurements are obtained per projection. To address this limitation, one possible solution is to enhance the density of the measurement beam. This can be accomplished by reducing the size of the sensor, thereby enabling a closer arrangement of measurement beams. By increasing the density of measurements, a greater number of data points are available for the tomographic reconstruction, offering the potential to enhance the resolution.

3.4 Modular Sensor Configuration

Based on the insights gained from the initial exploration into modular design, the size of the collimator and photodetector is the primary factor that limits the beam spacing. To achieve a further reduction in beam spacing and increase the amount of sampled data for reconstruction, one approach is to decrease the size of each emitting and receiving sensor. This allows for more beams to pass through the detection area. Additionally, considering a long light path of up to 1 m, it is important to provide some flexibility for beam adjustment. Taking these factors into account, this section introduces a miniature and modular design for the emitter and receiver. The model view of the emitter and receiver and the diagram of the laser path are shown in Figure 3.9.

3.4.1 Emitter

As shown in Figure 3.9 (a), The emitter with a dimension of 30 mm × 30 mm × 9 mm is mainly composed of three parts: the collimator, the adjusting mirror, and the supporting frame.

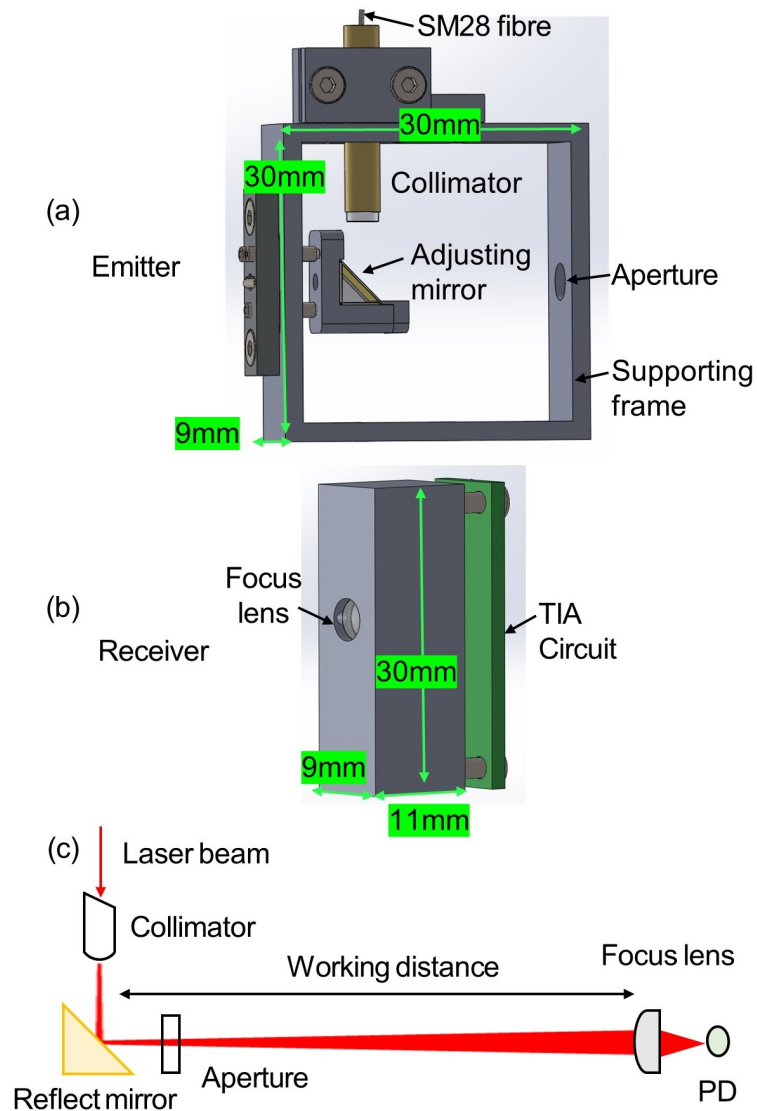


Figure 3.9: Diagram of the (a) emitter, (b) receiver and (c) laser path.

To compensate for the large divergence angle of the laser emitted from the optical fibre, a fibre collimator is used to collimate the laser beam and ensure sufficient light intensity received after propagating through the detection path. Ball lens, GRIN lens and C lens are three kinds of single optics commonly used for the collimation of fibre output. The C lens, illustrated in Figure 3.10, stands out due to its extended working distance relative to GRIN lenses and its economical pricing compared to the available ball and GRIN lenses.

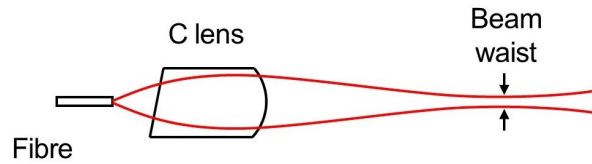


Figure 3.10: Diagram of C lens used for collimation.

As the direction of light's propagation is influenced by temperature gradients [28], in practical applications, temperature turbulence within the target can lead to beam steering. When the beam is thin, a significant temperature gradient affects a large part of the beam's propagation direction, heightening the risk of detection failure. Nevertheless, only a small fraction of the beam is influenced by the temperature gradient if the beam is wide. Therefore, it is advisable to avoid placing the beam waist, the thinnest part of the beam, in areas with temperature turbulence. Additionally, due to manufacturing tolerances, each C lens may have a slightly different beam profile.

To ensure that severe beam steering is minimised, the diameters of the beam spot along propagation are measured. The measurement process involves fixing the photodetector on the optical path and using a mechanical arm with 0.1 mm precision to hold the collimator. The centre of the focal point corresponds to where the PD registers the highest signal intensity. By performing scan movement from the centre of the spot with 0.1 mm displacements in the plane perpendicular to the optical, the PD captured different intensities at different positions of the collimator. The spot's size is identified by the intensity map. The spot's radius is characterised by the distance from the centre of the spot to the position with 1% of the maximum signal intensity. Figure 3.11 shows the test results for two C lenses in the same batch, illustrating the variations in the beam profiles at different working distances.

Instead of directly aligning the collimator with the detection path, an alternative approach is employed, where the collimator is positioned perpendicular to the optical path. In this configuration, a right-angle prism is utilised to redirect the collimated laser beam toward the desired detection path. A customised aluminium mount is employed to securely hold the right-angle prism in place. This mount is connected to the supporting frame through the use of a spring, which provides stability and allows for flexibility in tilting the mirror. Additionally, three screws are utilised to introduce

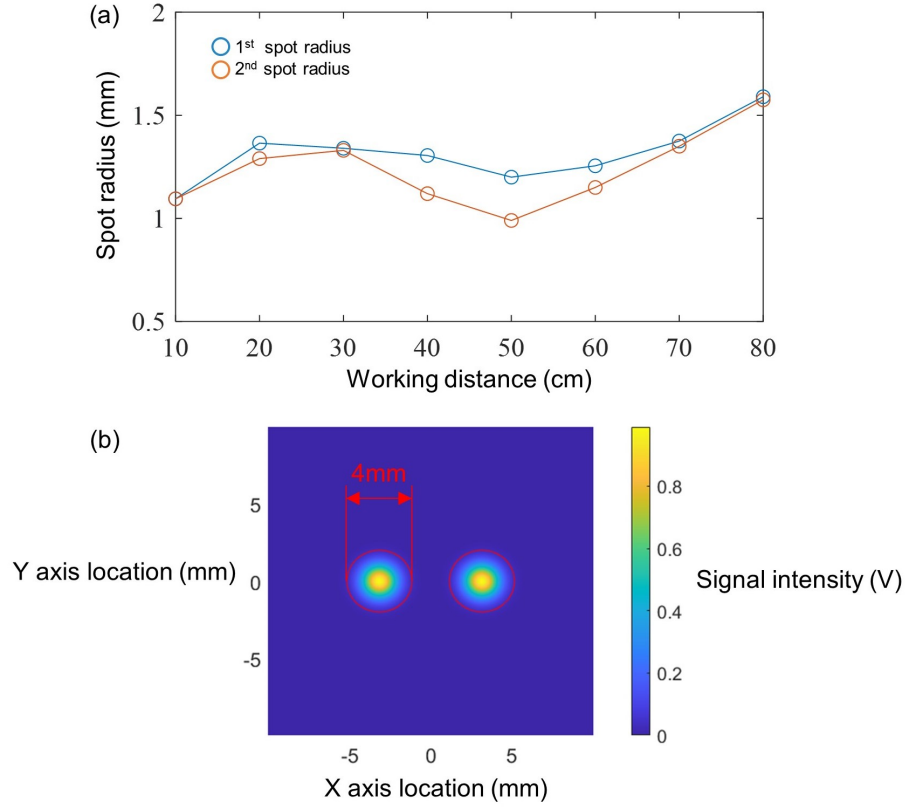


Figure 3.11: Spot size validation for two C lenses from the same batch. (a) Spot size at different working distances (b) Combine beams at 80 cm with 4 mm diameter lens dictator.

extension force to the spring and adjust the position of the mirror, enabling precise alignment and fine-tuning of the beam direction. Taking the distance between the reflective mirror and the 4 mm aperture on the supporting frame into consideration, the collimated laser beam at the emitting side is adjusted within a range of 5 degrees.

3.4.2 Receiver

The receiver unit, depicted in Figure 3.9 (b), incorporates rectangular optomechanics to mount the plano-convex lens and the photodetector circuit. The purpose of the focus lens is to ensure maximum reception of the laser beam by the PD, compensating manufacturing tolerances and beam steering. By positioning the PD's photosensitive surface at the focal length of the plano-convex lens, optimal laser reception is achieved.

The PD and op-amp used in this photodetector design are the same as those employed in the lab-scale system. However, instead of using a variable amplifying resistor, a fixed-value resistor is used to avoid any potential instability. To evaluate the bandwidth of the photodetector circuit at different resistance values, a numerical simulation was conducted using the Multisim software. The simulation results, depicted in Figure 3.12, illustrate the bandwidth for gains of 500, 1k, 2k, 3k, 4k, and 5k, respectively.

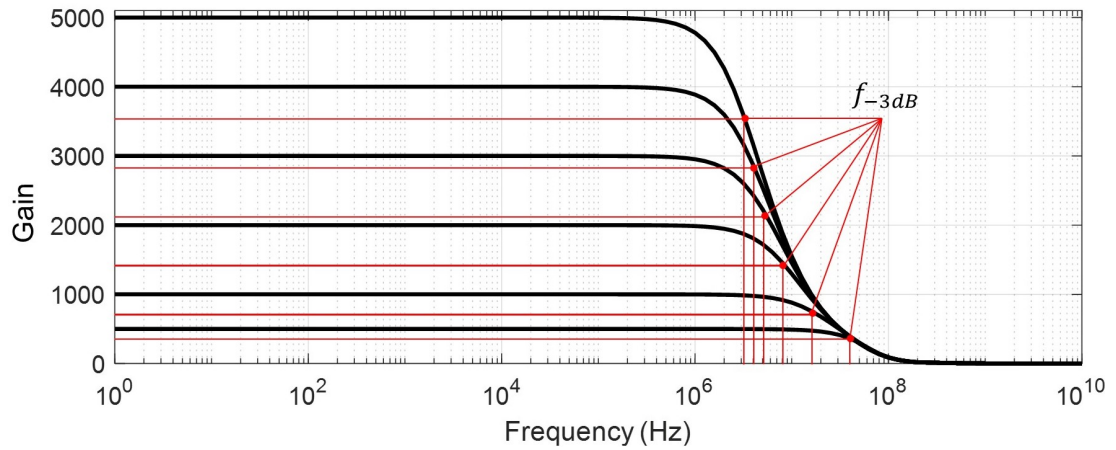


Figure 3.12: Simulation bandwidth with gains at 500, 1k, 2k, 3k, 4k and 5k, respectively.

To accommodate the constraints imposed by the TO-18 packaging diameter of the PD (5.6 mm) and the width of the SOIC packaging of the op-amp (5 mm), the circuit layout was rearranged, resulting in a narrow PCB board with width of 9 mm. This compact design allows for efficient utilisation of the available space, as shown in Figure 3.13.

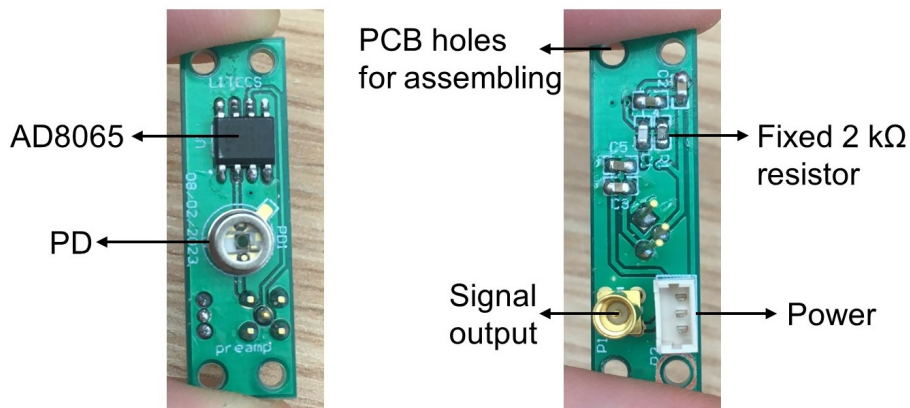


Figure 3.13: PCB layout of the TIA in modular receiver.

In practical applications, there are several factors that limit the further reduction of beam spacing in the LAS tomographic system:

1. Beam steering: Turbulence in the flow can cause the laser beam to deflect slightly, resulting in beam steering. Smaller beam spacing increases the risk of crosstalk between adjacent beams, compromising the accuracy of the measurement.
2. Processing tolerances: Variations in the dimensions of optical components, spot sizes of lenses at working distances, and the actual position of the photosensitive surface are influenced by processing tolerances. Finer structures are more susceptible to these variations, which can impact the performance of the system.
3. Response of photosensitive surface: Smaller PDs have smaller photosensitive surfaces, which presents challenges in aligning the incident light accurately onto the photosensitive area. In addition, smaller photosensitive surfaces can be more prone to overexcitation, where the light intensity exceeds the linear operating range of the PD. This non-linear response can introduce distortions and compromise the signal quality, challenging subsequent signal processing.

Taking these factors into account, resilience stands out as a vital factor in sensor design. Decreasing the spacing of adjacent beams to below 1 mm can heighten susceptibility to noise and crosstalk in combustion scenarios.

3.4.3 Functional Test

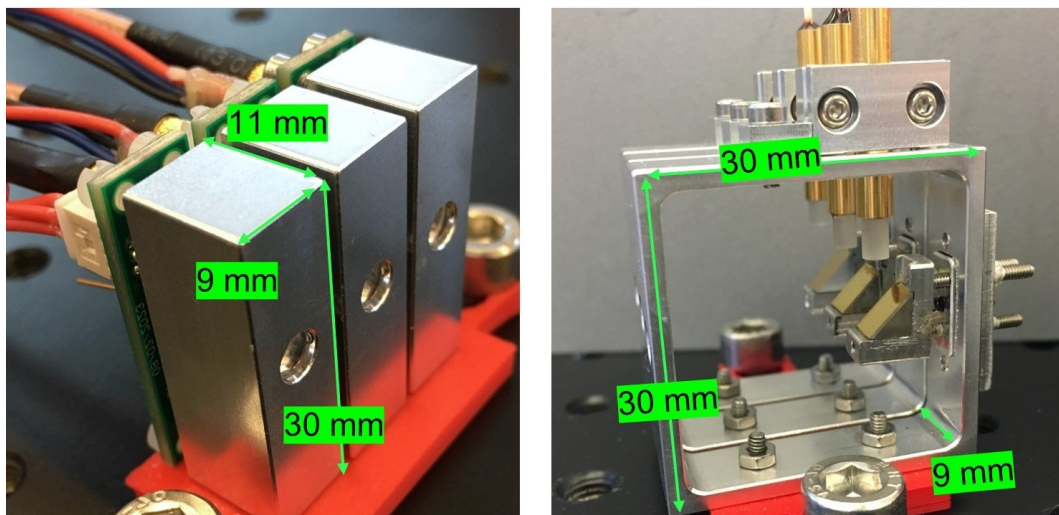


Figure 3.14: Example test setup and the three prototypes for testing.

A validation test was performed to compare the measurement results of room temperature and ambient H_2O concentration obtained from three adjacent channels of the modular prototype, as depicted in Figure 3.14, with the readings of a humidity sensor (Sensirion, SHT31 [84]). Both two kinds of sensors and the 50 cm light path for detection were sealed in a box to mitigate interference. The test adopts laser driving and data acquisition from the lab-scale system. Both the lasers at 7185 cm^{-1} and 7444 cm^{-1} were tuned by 1 kHz sinusoid and modulated with 100 kHz and 130 kHz sinusoid, respectively. This enables a temporal resolution of the measurement to be 1 kHz. Continuous measurement of the temperature and H_2O concentration was carried out for 5 minutes. The light was coupled and split into 32 channels, three of the 32 were connected to the emitters. The detected signals were then digitised by a RP-based DAQ [79] and sent to the desktop for post-processing. The measurement results of mean and Standard Deviation (STD) are given in Table 3.2.

Metrics Sensors	H_2O concentration		Temperature ($^{\circ}\text{C}$)	
	Mean	STD	Mean	STD
SHT31	0.0079	15.6%	21.89	2%
Modular channel 1	0.0082	4.2%	20.32	8.1%
Modular channel 2	0.0082	4.0%	20.35	7.6%
Modular channel 3	0.0081	4.5%	20.39	8.1%

Table 3.2: Compare the test results of temperature and H_2O concentration from Three sensor prototypes with humanity sensor.

The STDs of the reference humidity sensor are estimated via its datasheet. This sensor has $\pm 0.2\%$ $^{\circ}\text{C}$ and $\pm 2\%$ RH typical tolerance. This brings 15.6% uncertainty of the molar fraction and 2% uncertainty of the temperature measurement when the average temperature and molar fraction are $20\text{ }^{\circ}\text{C}$ and 0.0079, respectively

Overall, the three optic sensors showed similar test results, but the LAS sensors recorded slightly higher H_2O concentration than the humidity sensor. The fluctuations in H_2O concentration over a 5-minute period were approximately 4.2%, which is lower than the 15.6% of the reference. On the other hand, the LAS sensors consistently provided lower temperature measurements compared to the reference values. The temperature fluctuations are twice the fluctuations of concentration. This difference can be attributed to the weaker linestrength at 7444 cm^{-1} at room temperature, which

is only one-fifth of that at 7185 cm^{-1} . Additionally, when calculating the temperature ratio, the inclusion of the 7444 cm^{-1} line introduces its own fluctuations into the computation, resulting in an overall lower calculated temperature value. It is noteworthy that temperature measurements are more susceptible to noise interference in this setup.

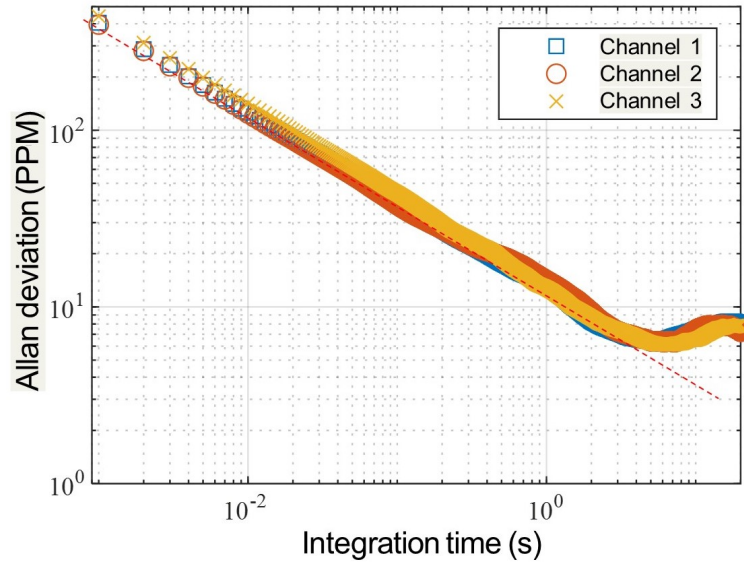


Figure 3.15: Allan deviation analysis at 1 atm and room temperature. The red line proportional to $\sqrt{\tau}$ indicates the theoretically expected behaviour of the system dominated by white noise.

To analyse the noise in the measurements, an Allan deviation analysis was conducted to assess the stability of the H_2O measurement. As depicted in Figure 3.15, the three measurements overlap with each other and closely follow the $1/\sqrt{\tau}$ trend. This indicates that the three sensors exhibit similar noise performance and that their measurements are primarily influenced by white noise.

3.5 128-Channel LAS Tomographic System for Industrial Application

The modular sensor mentioned above can be conveniently attached to frames of different shapes using screws for tomographic applications. Figure 3.16 presents an application example, demonstrating the fixation of 32 closely arranged emitting and receiving sensors on each side of an octagonal frame, enabling LAS measurements with a 1 cm adjacent beam spacing in RoI. By modifying the frame shape and adjusting the number of sensors, the beam arrangement can be easily customised to adapt to different applications, as depicted in Figure 3.17.

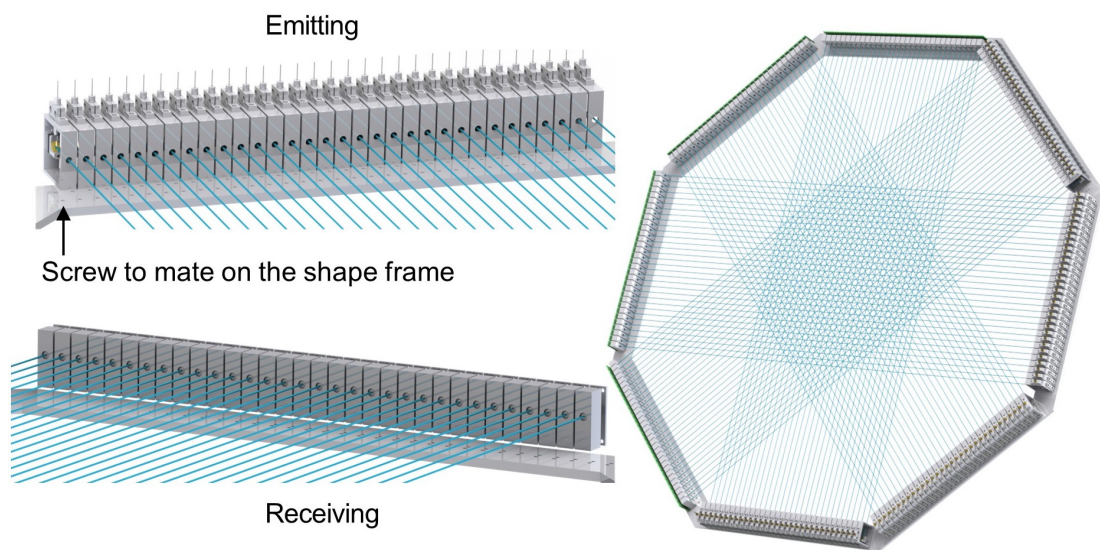


Figure 3.16: 128-channel LAS tomographic sensor with octagon shape frame.

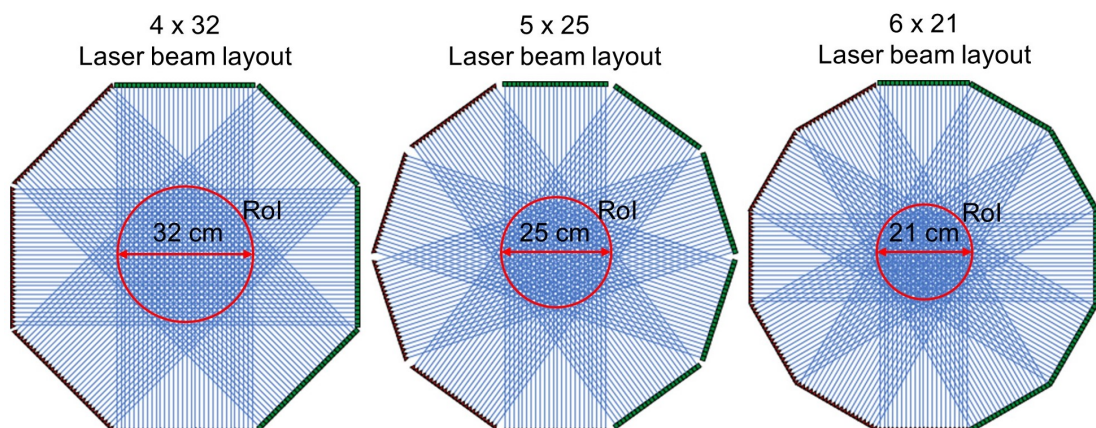


Figure 3.17: Example beam arrangement with large beam count.

As the number of beams increases in the LAS tomographic system, it becomes crucial to ensure sufficient light intensity signals and address the challenges associated with data acquisition.

To maintain an adequate light intensity signal for each path, two approaches can be considered. Firstly, more powerful lasers should be employed at the emitter side to compensate for the diminishing light signal due to increased beam splitting. Alternatively, light-intensity power amplifiers like Thulium-Doped Fiber Amplifiers (TDFAs) are used after the laser to boost the signal strength [30].

The increase in the number of optical paths also results in a significant growth in the amount of collected data. However, the data transmission rate is limited by the network cable and the data rate of the computer's network port in ethernet transmission. Therefore, it becomes necessary to implement hardware solutions that preserve the acquired information while reducing the amount of data to be transmitted. Techniques such as multiplexing [79] and downsampling [86], should be employed for this purpose. Multiplexing allows multiple data signals to be combined and transmitted over a single channel, reducing the number of data transmission paths required. Downsampling involves reducing the sampling rate of the acquired data while preserving important information, thereby reducing the overall data size without significant loss of critical details.

3.6 Summary

The chapter begins by introducing the architecture of LAS tomographic systems. It uses a 32-channel lab-scale system as a representative example, showcasing the exploration into modular sensor design and emphasising the design considerations. In order to further enhance the spatial resolution and reconfigurability of LAS tomographic systems, a miniature and modular sensor was designed. This innovative design advances the lower limit of adjacent beam spacing beyond the capabilities of the current state-of-the-art LAS tomographic system, ultimately enhancing the flexibility of sensor deployment.

The design primarily focused on reducing the size of the emitter and receiver, resulting in dimensions of 30 mm × 30 mm × 9 mm and 11 mm × 30 mm × 9 mm, respectively. This compact design enabled a flexible beam arrangement with a beam spacing of 1 cm and a temporal resolution of 1 kHz. A prototype of the sensor was manufac-

tured and subjected to laboratory testing. The sensor's performance was evaluated by measuring room temperature and ambient H₂O concentration. The results were compared against the reference. Experimental findings revealed a close correlation between the measurements obtained using the developed sensor and the reference values, with a 4% fluctuation attributed to the presence of white noise. This demonstrated the reliability and accuracy of the proposed sensor design. Lastly, tomographic systems with high beam counts using the modular design were presented. Extra design considerations of laser driving and data acquisition for industrial applications were discussed.

Chapter 4

A Multi-channel Sensor for Turbine Exhaust Measurement

4.1 Introduction

Based on the modular sensor designed in Chapter 3, this chapter develops a new application for monitoring the exhaust of a GTE with a multi-channel sensor. GTEs are widely used in various industrial sectors including propulsion, power generation and chemical engineering. With the urgent need to achieve carbon neutrality, many improvements in GTE technology are currently underway for accepting environmentally compatible fuels whilst maintaining the safety of GTE operation [1; 2].

The exhaust gas composition and EGT are key indicators of GTE combustion efficiency, emissions and health condition [87]. Sustainable Aviation Fuels (SAFs), for example, are low-carbon alternatives for aviation GTEs, that typically contain a higher ratio of iso-paraffins and lower ratios of aromatics and cycloparaffin [88]. Therefore, SAFs generally have higher hydrogen content, resulting in high levels of H_2O in the combustion products. Measurements of H_2O become increasingly popular for analysing the chemical reaction using SAFs for GTE [89]. In addition, EGT reflects physicochemical properties relevant to combustion efficiency [90] and more crucially, to predict potential engine failures [91]. Due to the high velocity and turbulent nature of the GTE exhaust plume, as well as the harsh sensing environment, it has been a longstanding challenge to develop *in situ* and robust sensors to monitor H_2O and EGT simultaneously, rapidly, and accurately.

Traditional H_2O and EGT sensors utilising extractive gas sampling and TCs suffer from intrusiveness and slow responses. To be specific, H_2O sensors, based on FTIR, require an extractive sampling from the plume to the analytical instruments using heated transportation lines. This system is susceptible to cold spots which results

in fluctuation in the measured H_2O concentration and potential loss of water due to condensation. Furthermore, gas sampling and analysis introduce sampling residence time, limiting their real-time response when indicating the dynamic changes of the H_2O . Similarly, TCs are most commonly used for EGT measurement. It also suffers from slow responses due to its sensing principle, which is based on the heat transfer dynamics, and the thermal capacity [3]. Efforts have been directed towards the development of EGT sensors that utilise acoustic and optical modalities to achieve swift measurement capabilities. However, acoustic sensors rely on the measurement of temperature-dependent time of flight of sound waves to achieve fast EGT measurement [92], and the sound waves are easily perturbed by the high-speed exhaust gas, leading to potential measurement errors. Optical radiation thermometers infer EGT from the heat radiation emitted from reflectors, for example, metals, however, they are less quantitative since the measured radiation is contaminated by that in the environment [7].

In this chapter, an eight-beam LAS sensor has been designed and implemented for *in situ*, simultaneous, accurate and rapid measurements of both H_2O and EGT. The main contributions are as follows:

1. A robust multi-beam LAS sensor with 6.3 mm beam spacing has been designed to quantify the edge effects of the plume that generate non-uniform gas concentrations and temperature at the plume edge. This edge compensation technique is then used to correct the line-of-sight LAS measurement through the plume centerline. Such sensing capability enables more accurate measurement of both H_2O and EGT at any dynamic GTE working conditions.
2. The developed sensor enables real-time measurement of the physicochemical parameters in the GTE plume with a temporal resolution of 4 milliseconds. Such a fast response reveals the hidden dynamic behaviours of the GTEs that are unable to be observed by traditional methods.
3. An in-situ experiment is carried out to test and validate the developed sensor on a commercial APU gas turbine. The experimental results agree with the traditional benchmarks at APU steady-state conditions and provide a rapid indication of APU control performance at the transient-state conditions.

4.2 APU

This chapter focuses on the monitoring of EGT and exhaust H_2O in a commercial APU (Honeywell, 131-9A) [93], which exemplifies a typical application of GTE in propulsion and power generation. The APU, depicted in Figure 4.1, is typically positioned at the aircraft's tail, providing airflow and supplementary power for various systems, such as air conditioning systems and aircraft control systems.



Figure 4.1: Honeywell 131-9A in service with Airbus A320.

4.3 Sensor Design

4.3.1 Absorption Line Selection

Table 4.1 shows the spectral parameters of the three H₂O absorption lines utilised by the sensor described here. Their central wavenumbers are $\nu_1 = 5000.2 \text{ cm}^{-1}$, $\nu_2 = 7185.6 \text{ cm}^{-1}$ and $\nu_3 = 7444.4 \text{ cm}^{-1}$. Figure 4.2 illustrates H₂O absorbance spectra at room temperature, 21°C, and typical EGT, 400°C, when $L = 50 \text{ cm}$, $P = 1 \text{ atm}$ and typical H₂O molar fraction in the exhaust as 5%, with black and red curves, respectively. At EGT-similar temperatures, all primary absorption lines provide 0.2 and above peak absorbance, enabling a good SNR of the measured WMS- $2f/1f$ signal.

Line	ν_1	ν_2			ν_3	
Parameter	t1	t2	t3	t4	t5	t6
$\nu_0 \text{ (cm}^{-1}\text{)}$	5000.223	7185.596	7185.597	7444.351	7444.368	7444.371
$S \text{ (cm}^{-2}\text{atm}^{-1}\text{)}$	5.124^{-3}	1.033^{-2}	3.098^{-2}	8.742^{-3}	2.721^{-3}	8.168^{-3}
$E'' \text{ (cm}^{-1}\text{)}$	2358.302	1045.058	1045.057	1774.750	1806.670	1806.669
HWHM (cm ⁻¹)	0.0323	0.0655	0.0711	0.0523	0.0503	0.0467

Table 4.1: Spectral parameters of the selected H₂O lines at $T = 400^\circ\text{C}$, $P = 1 \text{ atm}$ (HITRAN database).

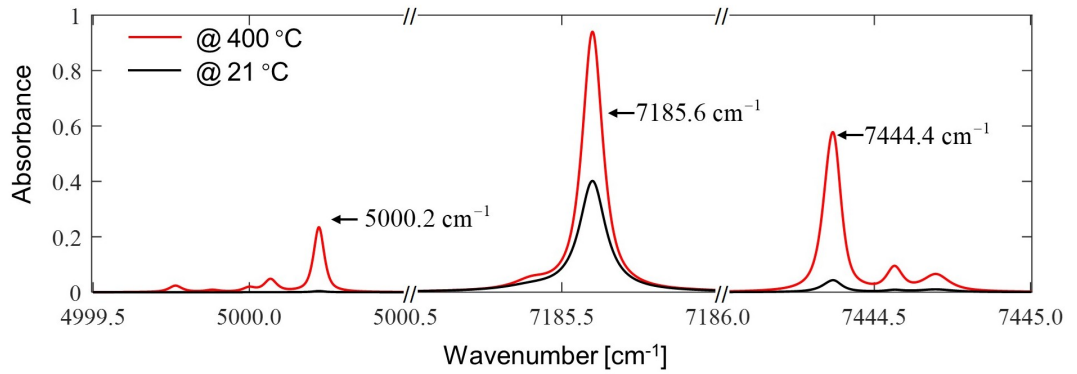


Figure 4.2: Absorbance spectra at 21°C and 400°C for the selected H₂O lines assuming $L = 50 \text{ cm}$, $\chi = 5\%$ and $P = 1 \text{ atm}$.

The absorption feature at ν_1 (t1 in Table 4.1) is composed of a single spectral transition. In the sensor designed here, ν_1 is utilised to characterise the non-uniformity at the plume edge as the probability of absorption at room temperature is more than 50 times lower than the assumed absorption of the plume, therefore ensuring minimal optical absorption due to ambient H_2O outside the plume. In addition, ν_1 falls in a frequency range where the optical power can be amplified using a TDFA [30]. This ensures the optical power on each receiver is sufficient to provide the highest SNR.

The absorption features at ν_2 and ν_3 are used for temperature and H_2O concentration measurement. These features have been widely used in ratio thermometry with proven sensitivity in the temperature range of 21°C to 800°C [46], which covers the EGT range at different engine loads. ν_2 is comprised of two adjacent transitions (t2, t3 in Table 1) with a stronger absorption at ambient temperature, while ν_3 is a high-temperature feature comprising of three adjacent transitions (t4, t5, t6 in Table 1).

4.3.2 Sensor Configuration

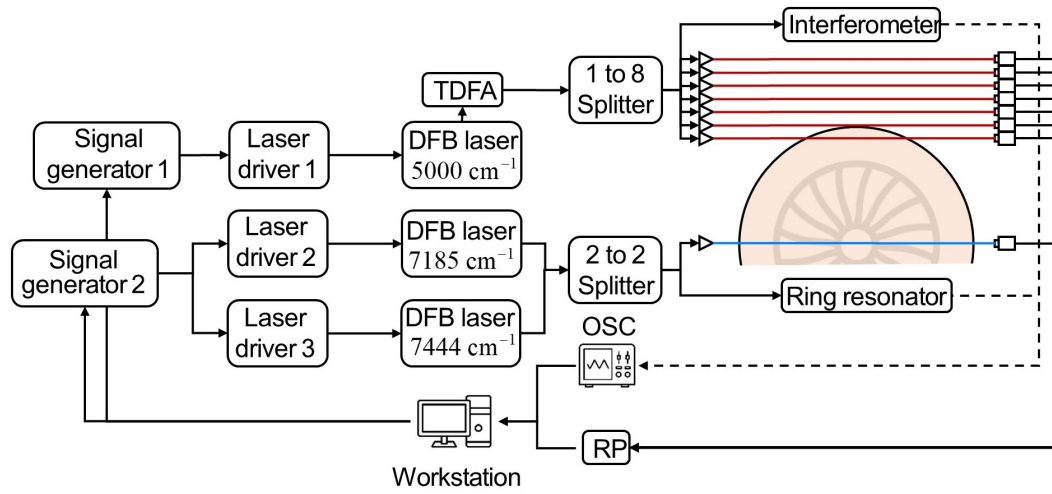


Figure 4.3: Schematic diagram of the developed 8-channel system.

The schematic diagram of the sensing system is shown in Figure 4.3, which consists of laser driving, optical distribution, optical detection, and data acquisition.

The optical signals at ν_1 , ν_2 and ν_3 are generated by three DFB laser diodes, Nanoplus 2000 nm, NEL NLK1E5EAAA and NEL NLK1B5EAAA, respectively. Each DFB laser diode is temperature- and current-controlled by a laser driver (Wavelength Electronics, LDTC 2-2E). Temperature control is used to ensure the central wavenumber of each laser output is maintained. The frequencies of driving currents of the three lasers

are shown in Table 4.2. All three lasers are scanned with $f_s = 1$ kHz sinusoidal wave. Signal generator 1 controls the injected current waveform to scan across 5000.2 cm^{-1} with a 130 kHz high-frequency modulation. The two lasers at 7185 cm^{-1} and 7444 cm^{-1} use FDM [46] to synchronise the optical signals for the same target gas. Signal generator 2 provides different modulation frequencies to the two laser controllers at 100 kHz and 130 kHz, to avoid frequency aliasing on the $1f$ and $2f$ signals.

Since the power of the laser diode at 5000.2 cm^{-1} is less than 2 mW, the output laser is amplified by a TDFA (Keopsys) and then equally split into eight beams using a 1-to-8 fused fibre splitter. As shown in Figure 4.3, seven of the eight beams are equally and closely spaced, with 6.3 mm spacing, to characterise the plume edge, whilst the eighth is passed through a Mach–Zehnder interferometer for $v(t)$ characterisation. The optical signals from the lasers at 7185 cm^{-1} and 7444 cm^{-1} are combined and then split into 2 beams using a 50:50 fibre coupler. One of the two coupler outputs penetrates the plume centre to measure H_2O and temperature, while the other is used for $v(t)$ characterisation through a ring resonator.

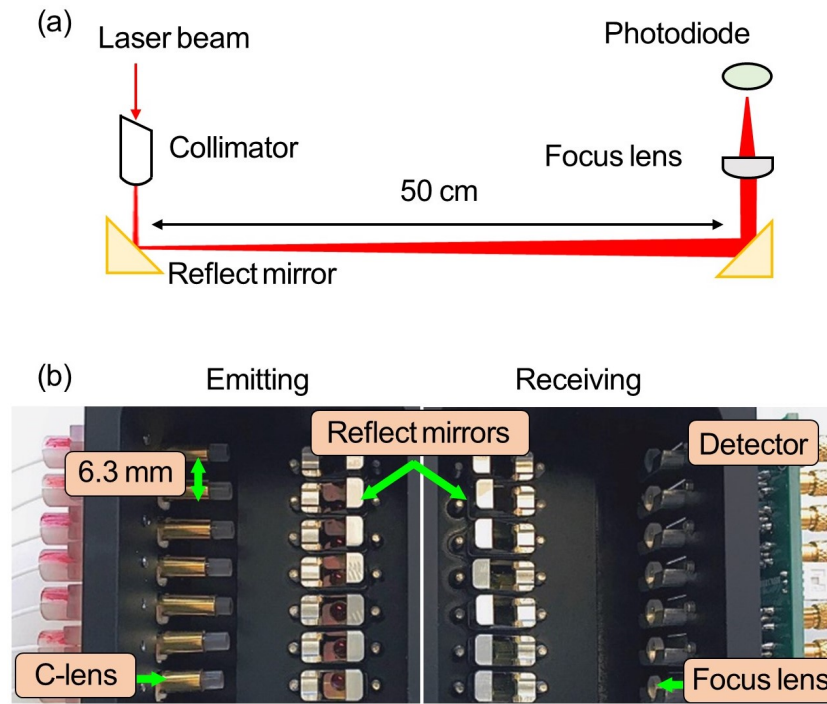


Figure 4.4: Optical layout of (a) a single-beam measurement and (b) 7 laser beams located at the plume edge.

The optics design for each laser-beam measurement is shown in Figure 4.4 (a). The optical beams are emitted using C-lens collimators. Two 5 mm gold-coated prism mirrors enable beam alignment in two dimensional on both the emitting and receiving ends. The transmitted laser beam is then focused by a 4 mm plano-convex lens and the photodiode (Hamamatsu, G12182-010K) is placed at the lens's focus. After traversing a 50 cm light path, the laser spot is about 2 mm in diameter, which underfills the photosensitive surface after being focused by the plano-convex lens. A single-ended TIA was designed based on a low-noise FET Op Amp (AD8066), converting the photodiode current output to a voltage signal with an amplification factor of 1k and a -3 dB bandwidth of 6 MHz. Both the emitting and receiving optomechanics are enclosed by aluminium cases with small apertures, allowing beams to pass through and protecting the sensor from heat radiation and turbulent disturbance. Figure 4.4 (b) shows the assembly of the 7 laser beams located at the plume edge. Since the diameter of the photodiode's TO-18 cap is 5.6 mm, the minimum manufacturing tolerance allows a beam spacing of 6.3 mm while maintaining 5° angular adjustment freedom. The small beam spacing enabled by our design greatly improves the spatial resolution for compensating the non-uniformity of the gas parameters at the plume edge, thus leading to more accurate retrieval of the H₂O and EGT.

All sensing signals are digitised by an RP-based DAQ system, detailed previously in [79]. Two parallel ADCs in each RP worked at a sampling rate of 15.625 Mega Samples/second (MSPS). Each ADC is time-division multiplexed across 4 laser-beam signals at the intervals of consecutive periods of the wavenumber scan, giving a final time resolution of 250 Hz for each of the 8 optical beams. The inputs to the RP are demodulated using SC on the RP to obtain the $1f$ and $2f$ spectra [86], which are then transferred to the workstation via ethernet.

ν (cm ⁻¹)	Sinusoidal scan	Sinusoidal modulation	Coupling	DAQ
5000.2	1 kHz	130 kHz	1×8	7 detected by RP @ 15.625 MSps 1 detected by OSC @ 500 MSps
7185.6	1 kHz	100 kHz	2×2	1 detected by RP @ 15.625 MSps
7444.4		130 kHz		1 detected by OSC @ 500 MSps

Table 4.2: Laser driving parameters of the three DFBs used in the sensor.

4.4 Validation on APU

Figure 4.5 illustrates the APU and the positioning of the developed sensor relative to the APU exhaust plume. A guide tube with a length of 30 cm and a diameter of 25 cm is attached to the rear of the APU exit, directing the flow into the exhaust system. The laser sensor is mounted on a plane 3 cm downstream of the outlet of the guide tube. A K-type TC is inserted at the inlet of the guide tube as shown in Figure 4.5(b), providing a reference EGT during the test. As the APU exhaust velocity is up to 100 m/s, the temperature difference at the inlet and outlet of the guide tube is assumed to be negligible.

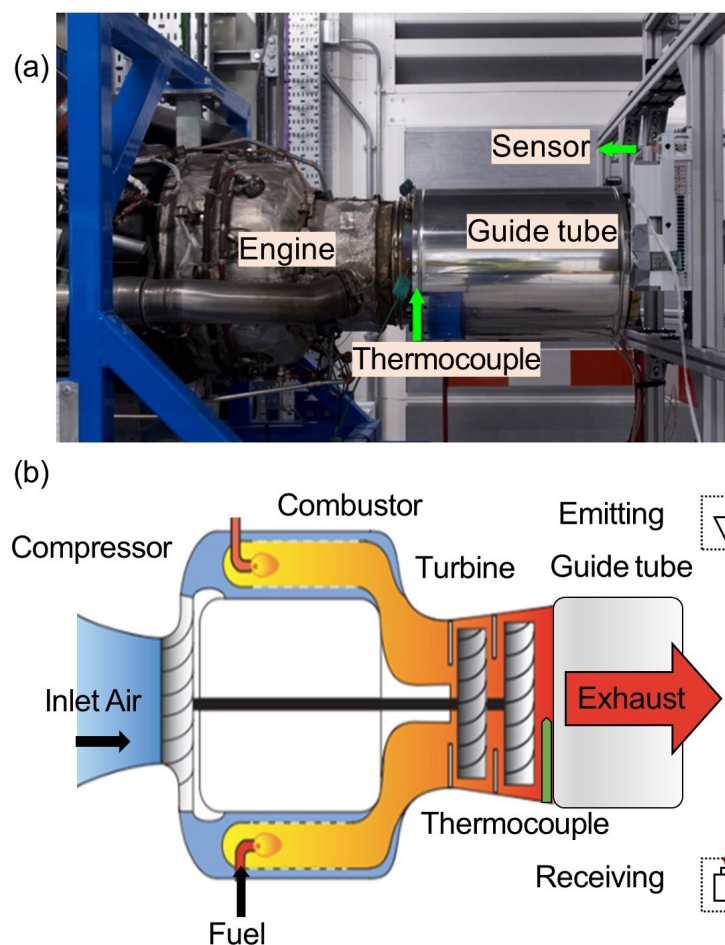


Figure 4.5: *In situ* experimental system. (a) and (b) show the picture and the schematic layout of the APU and the sensor.

4.4.1 Non-Uniformity Distribution

When the APU is operating, the hot exhaust plume mixes with cold ambient air at the guide tube outlet, resulting in non-uniform radial profiles of H_2O and EGT along the plume edge. Failing to consider this non-uniformity will cause systematic errors in LAS recovery of EGT and χ [94]. A FTIR extractive gas sampling probe and a K-type TC, shown in Figure 4.6, scanned horizontally across the centre of the plume on the same plane as the laser measurement during APU steady full-load operation to measure the non-uniformity at the plume-edge.

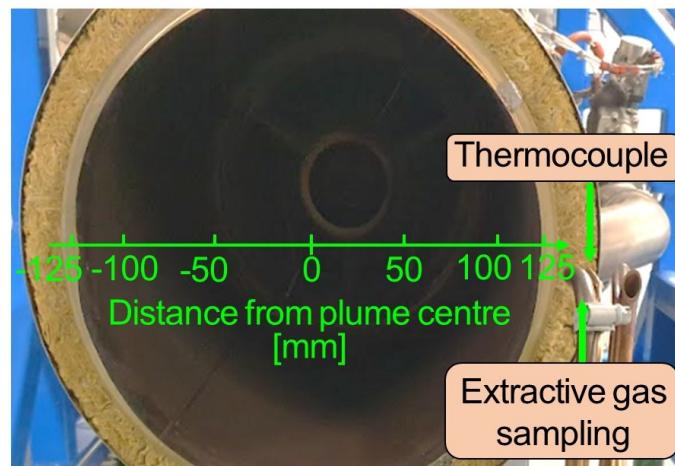


Figure 4.6: Non-uniformity characterisation at APU plume edge using scanned extractive gas sampling and TC.

Firstly, focus on the dashed line in Figure 4.7. The pointwise measurements of H_2O and EGT along the scan are shown by the black and red dashed lines, respectively, showing trapezoidal radial profiles for both measurements. The H_2O and EGT at the plateau are 3.6 % and 490°C respectively. They decrease rapidly beyond the diameter of the guide tube outlet. In principle, the plume is rotationally symmetric at the steady state. The asymmetry between the rising and falling edge of the temperature profile shown in Figure 4.7 is assumed due to the inherited lag of the TC measurement since the heat is aggregated on the TC during the scan. It is also worth noting that the profiles measured by the extractive gas sampling and TC are only valid when the APU is operating under steady-state conditions. They are not valid during APU startup, in which the dynamic process cannot be captured by the slow mechanical scan.

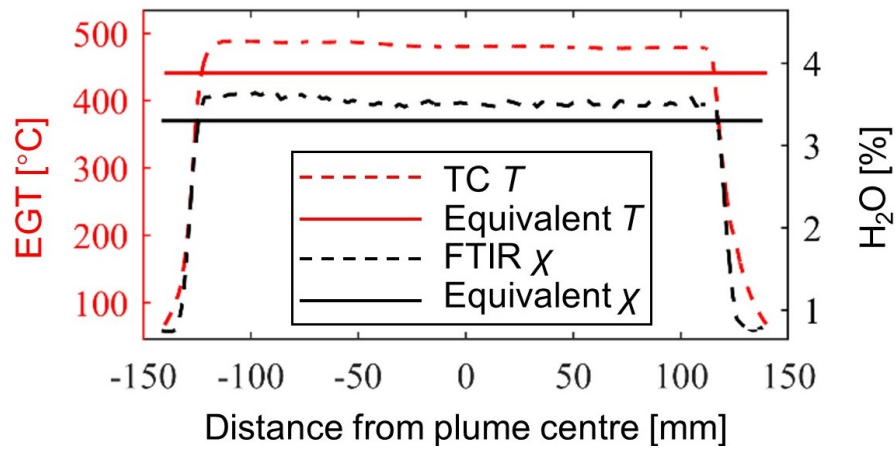


Figure 4.7: Point-wise measurement of temperature and H_2O concentration along the scan and their LAS-equivalent values under steady full-load conditions. The equivalent values for the whole plume path length are calculated via HITRAN.

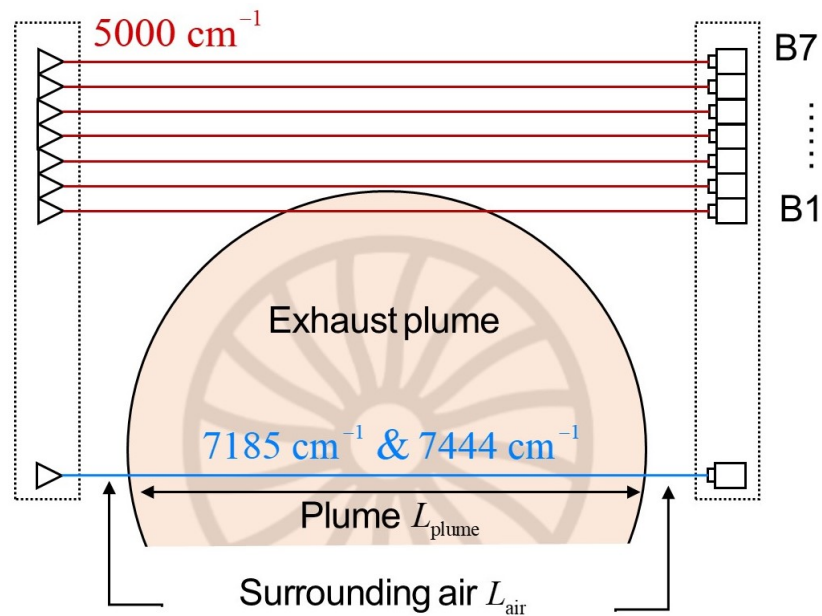


Figure 4.8: Beam layout of the multi-channel sensor at the APU exit.

Assuming rotational symmetry of the χ and EGT distributions, the above-mentioned non-uniformity can also be measured at 250 Hz using the 7 optical signals located around the plume edge, shown in Figure 4.8, with beam B2 aligned with the edge of the guide tube outlet. Figure 4.9 shows typical $2f/1f$ signals at 5000.2 cm^{-1} under steady full-load conditions, with their peak values marked by asterisks. Those values are assumed to indicate the magnitude of the path-integrated absorption. Figure 4.9 shows that the $2f/1f$ magnitudes gradually decrease from B1 to B3, indicating the decreasing absorption around the plume edge. The normalised χ , T , and asterisked values for B1-B7 are plotted on the left-hand side of Figure 4.9. The indicated gradient from B1-B3 on the plume edge agrees well with that obtained from the extractive gas sampling and TC measurements. In addition, B4-B7 consistently show very weak absorption, indicating they are measuring predominantly ambient air.

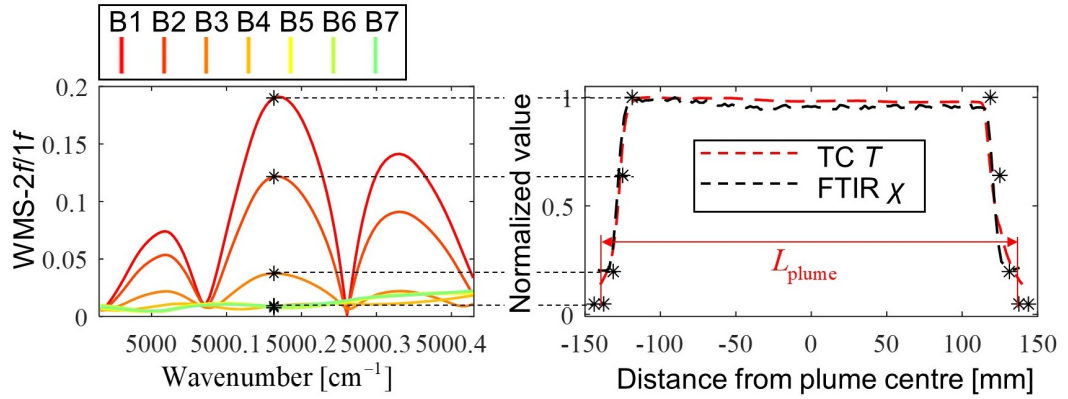


Figure 4.9: left: WMS- $2f/1f$ obtained for each of the 7 beams at the plume edge. Right: the comparison between the non-uniform profile retrieved using the LAS sensor and benchmarks.

The above radial information can be used to characterise the absorption along the beam that traverses the centre of the plume, with path length in the hot plume L_{plume} including the non-uniform plume-edge effects, whilst also defining the length of the beam-path in the ambient air L_{air} . From the LAS radial profile measurements at steady full-load condition, as shown in Figures 4.9, we define the plume radius to extend out to the radial position of B4, giving $L_{\text{plume}} = 275.2 \text{ mm}$ and $L_{\text{air}} = 224.8 \text{ mm}$. The H_2O molar fraction and EGT noted χ_{plume} , and T_{plume} , respectively, along the whole path length in the plume can be calculated by:

$$S(T_{\text{plume}})\chi_{\text{plume}}PL_{\text{plume}} = S(T_{\text{meas}})\chi_{\text{meas}}PL_{\text{meas}} - S(T_{\text{air}})\chi_{\text{air}}PL_{\text{air}}, \quad (4.1)$$

where $(\cdot)_{\text{plume}}$ and $(\cdot)_{\text{air}}$ denote the gas parameters in the plume and in the air, respectively. Here, $\chi_{\text{air}} = 0.6\%$ and $T = 24.5^\circ\text{C}$, as measured independently in the APU test cell. In the analysis below, the LAS measurements of χ_{plume} and T_{plume} are those obtained from Equation 4.1.

To facilitate the comparison between the above LAS measurements and those provided by the benchmark extractive gas sampling and the TC, we calculate the LAS path-integrated absorption that would be expected, for each spectral absorption feature at ν_2 and ν_3 in the HITRAN model [37], by applying the H_2O and EGT scanned measurements over the path length L_{plume} as defined above. Consequently, the equivalent temperature along light path, T_{eq} , can be obtained by ratio thermometry as follows:

$$R(T_{\text{eq}}) = \frac{\sum_L S_2(T_j) P \chi_j l_j}{\sum_L S_1(T_j) P \chi_j l_j}, \quad (4.2)$$

where χ_j and T_j denote the H_2O concentration and temperature in j^{th} discretised path length $l_j = 6.3$ mm along the scan. Then, the equivalent H_2O concentration, χ_{eq} , is calculated by Equation 2.40 using either of the two transitions. The black and red solid lines in Figure 4.7 show χ_{eq} and T_{eq} calculated from the non-uniform profiles. χ_{eq} and T_{eq} are 0.2% and 50°C below the extractive gas sampling and TC measurements at the plateau, respectively.

A separate test was carried out to validate the above characterisation when the APU is stabilised at the full-load condition. Table 4.3 shows the mean and variance of H_2O and EGT measured over 120 seconds during the full-load operation, generating 30,000 samples for the LAS and 1,200 samples for the FTIR (Gasment, DX4000) and TC (Omiga, K-type) at 10 Hz. The DAQ of the TC has been calibrated using cold junction compensation. Overall, the mean values of H_2O and EGT obtained using the LAS agree very well with the benchmarks, with a difference of only 0.02% and 3°C , respectively, demonstrating good accuracy of the developed sensor. In addition, the LAS measurements show excellent precision, with STD of mean values of $4.5 \times 10^{-3}\%$ in H_2O and 9.65°C in EGT. The slightly larger values of STD observed in LAS measurements of H_2O and EGT compared to those obtained using the extractive gas sampling and TC are likely to be caused by their different temporal responses, i.e., the variations introduced by the plume turbulence are more likely to be smoothed out by the slow-response benchmarks, captured at a slower sampling rate.

	LAS	Reference	LAS	Reference
	H ₂ O (%)	H ₂ O (%)	EGT (°C)	EGT (°C)
Mean	3.38	3.40	442.13	439.15
STD	4.5^{-2}	2.6^{-2}	9.65	3.57

Table 4.3: *In situ* measured H₂O and EGT at the APU full-load condition.

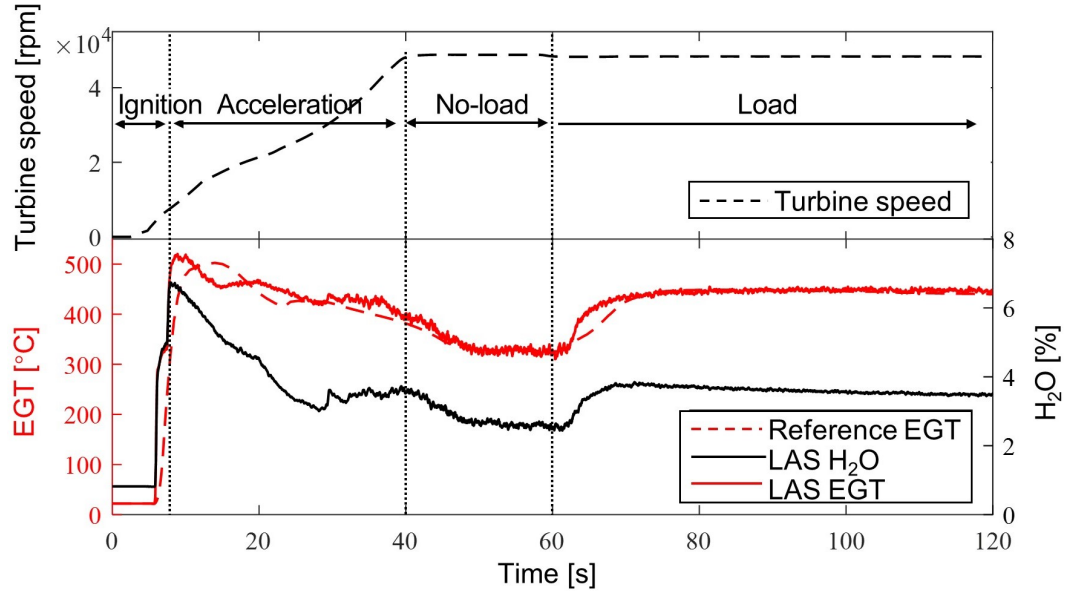


Figure 4.10: Comparison of dynamic H₂O and EGT obtained using the developed sensor and the TC under varying turbine speed for a 120-second APU experiment.

4.4.2 Dynamic Test

In this experiment, H₂O, χ_{plume} , and EGT, T_{plume} , were measured dynamically using the developed sensor from APU start-up to the steady-state conditions in a period of 120 seconds. The edge effects are quantified simultaneously with the gas measurement in the plume, enabling accurate measurement of both H₂O and EGT at any dynamic GTE working conditions. The APU was controlled by an Engine Control Unit (ECU) and went through four operating conditions: ignition, acceleration, no load, and full load. Figure 4.10 shows the comparison between the H₂O (black solid line) and EGT (red solid line) measured by LAS at 250 Hz, and the equivalent EGT based on the measurement of TC (red dashed line) at 10 Hz. The time axis is synchronised with

the turbine speed sampled at 10 Hz (black dashed line). The LAS EGT measurements match the reference EGT very closely at the two steady states, i.e., the no-load and full-load conditions. In the following, we further analyse the dynamic measurement results under each APU operating condition.

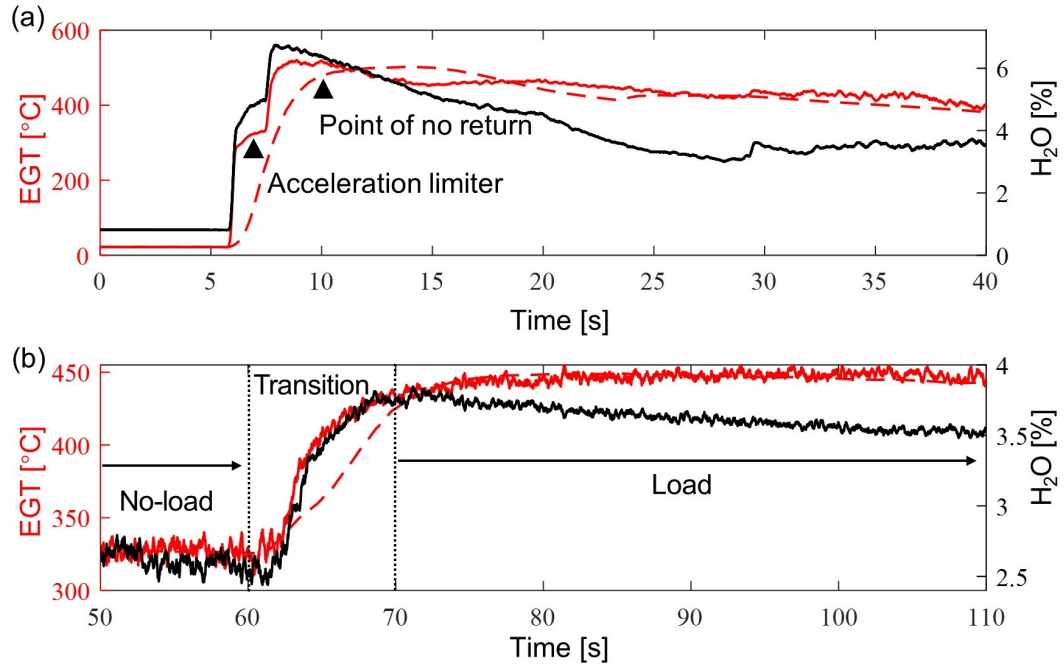


Figure 4.11: Dynamically sampled H₂O and EGT using the developed sensor under different APU operating conditions, i.e., (a) transient states for ignition and acceleration; (b) The transition period from no-load to the full-load steady-state condition.

Ignition and Acceleration

Figure 4.11 (a) shows the transient states recorded from engine start-up for a period of 40 seconds. From the time, $t = 0$ to 6 s, the motor provides initial power to spin the turbine, enabling air to flow through and mix with the Jet-A1 fuel prior to ignition. When the turbine speed reaches about 5000 rpm, the fuel-air mixture is ignited. At this point, the H₂O and EGT increase rapidly in the exhaust plume, peaking at 6.74% and 517.5°C, respectively. Following ignition, from $t = 6$ to 40 s, the fuel flow rate is increased to steadily accelerate the turbine until the APU passes the Point of No Return (PNR) at $t = 10$ s. During this process, the ECU dynamically controls the fuel injection to prevent excessive EGT that can potentially damage the engine. Beyond the PNR, the APU becomes self-sustained, and the turbine speed can be increased

with decreased fuel consumption, resulting in reduction of H_2O and EGT from their peak values. Overall, the profile of H_2O measured using the LAS sensor exhibits a strong correlation with the temperature profile. A more significant gap between the two can be observed after $t = 15\text{ s}$. Then, EGT is steady while H_2O falls due to the decreased fuel injection.

The high temporal resolution of the LAS sensor reveals at least three APU behaviours not observable using the traditional extractive sampling and in situ TC methods during this period: Firstly, the LAS measurements accurately indicate the successful ignition of the APU with an abrupt increase in H_2O and EGT at $t = 6\text{ s}$ shown in Figure 4.11 (a) above, while the TC only shows a delayed and smooth EGT increment. Secondly, the LAS measurements resolve a temporary plateau between (7-8 s). Due to the acceleration limiter, the ECU temporarily slows down the fuel injection to prevent the turbine from overheating. It can be seen that the LAS sensor reveals a higher and earlier peak EGT. Its rapidness could facilitate further improvement of the state-of-the-art mode of fuel injection.

No Load and Full Load

After reaching the required turbine speed of $4.9 \times 10^4\text{ rpm}$, the APU enters a steady no-load working condition from 40 to 60 s. Within this period, the H_2O and EGT measured by the LAS sensor are stabilised at around 2.46 % and 330°C respectively. From 60 s, more fuel is injected to feed the APU at full load, while maintaining the turbine speed at $4.8 \times 10^4\text{ rpm}$. In Figure 4.11 (b), both the H_2O and EGT increase rapidly between 60 s and 70 s before settling to 3.71% and 445.5°C in the steady state full-load condition, respectively. Similar to the condition of acceleration, a decreasing tendency can be observed for the H_2O since less fuel is needed once the turbine speed can be maintained at the full-load condition.

It is worth noting that the plume edge compensation approach, validated for one static condition in Section 4.4.1, has been used in the no-load and full-load static conditions, where no reference of H_2O and EGT were taken. The stabilised EGT at 50-60 s and 75-110 s in Figure 4.10 obtained by the LAS sensor also agrees very well with the TC measurement. This indicates good accuracy of the plume edge compensation technique for measuring varying physicochemical parameters in the highly turbulent APU exhaust.

The LAS measurements show transient responses consistent with increments in the fuel injection rate. According to Figure 4.10 (b), the step responses of H₂O and EGT can be modelled

$$\Delta\chi(t) = 1.21 \times (1 - e^{-t/2.22}), \quad (4.3)$$

$$\Delta T(t) = 109.38 \times (1 - e^{-t/3.21}), \quad (4.4)$$

where the $\Delta\chi$ and ΔT denote the responses of H₂O and EGT on the fuel injection.

However, the above-step responses cannot be revealed using the TC. As shown in Figure 4.11 (b), the EGT obtained using the TC in the transition period shows a more linear performance, which disagrees with the nature of the step increment of fuel injection. Therefore, it can be concluded that the high-speed LAS sensor working is superior to the benchmark, i.e., extractive gas sampling and TC, in terms of more accurate measurement of the dynamics of turbulent exhaust.

4.5 Summary

This chapter elucidates the design and experimental validation of a multi-channel LAS sensor. This sensor stands out due to its exceptionally minimal adjacent beam spacing compared to the existing multichannel LAS sensors and the ability for rapid *in situ* monitoring of H₂O and EGT in GTEs. This advancement enables a detailed view of the temperature distribution at the mixing zone of the APU exhaust plume during the engine's dynamic operation.

The sensor employs seven beams emitted by a DFB seven beams emitted by a DFB laser working at 5000.2 cm⁻¹ to reveal the trapezoidal absorption distribution at the plume edge with a spatial resolution of 6.3 mm. Furthermore, H₂O and EGT measurements are performed using two DFB lasers operating at 7185.6 cm⁻¹ and 7444.35 cm⁻¹, exploiting the H₂O absorption line pair. The sensor was validated by performing extractive gas sampling and TC measurements on a commercial APU. The developed sensor exhibited good accuracy during the APU steady-stage condition, demonstrating a 0.02% molar fraction and a 3°C temperature difference from those obtained by benchmarks, i.e., extractive gas sampling and TC. The sensor had much better temporal resolution (4 ms) than the intrusive measurements, which provided additional insight into underlying GTE dynamic behaviours, viz. H₂O and EGT variation during engine ignition and subsequent fuel injection increase.

Chapter 5

Size-Adaptive Hybrid Meshing Scheme

5.1 Introduction

Previous chapters have introduced compact sensors designed to decrease the spacing between adjacent beams for improving tomographic reconstruction. Once the beam arrangement is established for a particular experiment, further enhancements of the tomographic image can be achieved by optimising the reconstruction. In LAS tomography, the target is normally located at the beam-dense region, the so-called RoI during reconstruction. The choice of RoI is typically implemented in two ways: (a) covering the whole sensing region with laser beams evenly arranged in the sensing region [47; 95] or (b) covering only the location-predetermined target flow with laser beams densely arranged in this area [55; 56; 96].

For case (a), the limited optical access generally restricts the number of beams that can be deployed in industrial practice, making the LAS tomographic inverse problem inherently rank deficient. With uniform-size meshes, beam layout with limited projections worsens the ill-posed problems, resulting in significant spike noises and artefacts in image reconstruction.

For case (b), previous attempts used nitrogen to purify the out-of-RoI area [55] or assumed the small absorption out of the RoI can be neglected [56]. However, the former is less practical to be deployed on industrial combustors, while the latter suffers from reconstruction errors due to the physical existence of out-of-RoI heat dissipation and species convection.

One approach to mitigate the problems mentioned above is to apply a non-uniform meshing scheme for the alleviation of rank deficiency, which has been well-validated in Electrical Capacitance Tomography (ECT) and Electrical Impedance Tomography (EIT). For instance, Wang *et al.* [97] deployed the adaptive refinement with triangular-shaped grids in ECT, improving the efficiency of reconstruction compared with the uniform refinement, showing a more accurate boundary in the reconstructed image. Similarly, Molinari *et al.* [98] developed a self-adaptive refinement algorithm in EIT for simple head model reconstruction based on error estimation. It is essential to note that ECT and EIT, which are tomographic techniques based on electrical effects, inherently differ from LAS tomography where light travels in straight paths. Therefore, the adaptive refinement mentioned above cannot be directly applied to LAS tomography. In addition, most of the target flow fields, for example, combustion processes, in LAS tomography are diffused with their patterns changing rapidly. This characteristic is radically different from that in ECT and EIT where clear boundaries exist for inhomogeneity. Consequently, the non-uniform meshing schemes proposed in ECT and EIT are inadequate to characterise the naturally diffused flows in LAS tomography.

Although a couple of previous works reported LAS tomography with irregular sensing regions, these attempts still employed a uniform-size or nearly uniform-size meshing without customisation of the density of the grids towards the target flows. For example, Wood *et al.* [99] numerically demonstrated the reconstruction of an annular sensing region for turbofan engine's imaging, but with uniform-size meshes in the domain. Recently, Grauer *et al.* [100] applied the finite element in meshing with the Bayesian model for image reconstruction in irregular regions. Although the finite element meshing scheme enables better flexibility at the domain boundary, the mesh sizes in the sensing domain are still nearly uniform size without specific or customised discretisation of the target area.

In this chapter, we introduce a size-adaptive hybrid meshing scheme for LAS tomographic reconstruction. The new scheme has four main contributions:

1. It introduces a spatially driven strategy to determine quantitatively the mesh size.
2. It is computation-effective by prioritising detailed reconstruction of the target flow.
3. It maintains the physical integrity by fully considering the background absorption into reconstruction.

4. It mitigates the impact of noise by self-adaptive refactorisation of the sensing matrix.

This development significantly facilitates the industrial application of LAS tomography towards practical combustors without modifying the layout of the optical sensor. In case of imaging combustion zone that is bypassed by cooling flows, e.g. aero-engine exhaust imaging [30], the proposed scheme can better characterise the target combustion zone with dense meshes while maintaining the integrity of the physical model by considering the absorption in the bypass flows with sparse meshes.

5.2 Size-Adaptive Hybrid Meshing Scheme

In Chapter 2 we analyse the ill-posed problem in LAS tomographic reconstruction from the perspective of SVD. To alleviate the ill-posed problem, we propose a 5-step size-adaptive hybrid meshing scheme to highlight the reconstruction of the target flow in the RoS. The RoS is divided into two parts: RoI which contains the target and the out-of-RoI region which reflects the background. It is worth mentioning that the dimension of RoI that covers the target flame can be determined in advance in both the lab-scale test [101] and industry application [30]. Although the flow field itself is dynamic, it can be located within the RoI. Therefore, the customised mesh sizes in and out of the RoI are adaptively determined, offline, and before the experiment, according to the spatial resolution. Figure 5.1 shows the 5 steps for implementation of the proposed scheme plotted with small numbers of laser beams and pixels for a clear view of the meshes and beam arrangement. As examined later in this subsection, the proposed scheme is also suitable for practical application with more densely arranged laser beams and finer discretised sensing regions.

Step 1: Choose RoI. RoI is chosen based on the target's size, the location of the target flow, and beam arrangement. The RoI, generally located within the beam-dense region, fully covers the target flow. In Figure 5.1 (a), the RoS is defined as a square region with dimensions of $D \times D$, while the central RoI is defined by $D_{\text{RoI}} = D/2$ to cover the beam-dense region.

Step 2: Find the marginal dimension of uniform-size meshing in the RoI. This step aims at finding the minimum meshing size that enables all the pixels in the RoI to have beams passing through. The process is done by enumeration. Given the RoS is discretised into $N \times N$ pixels, the enumeration starts from $N = 1$. As N increases

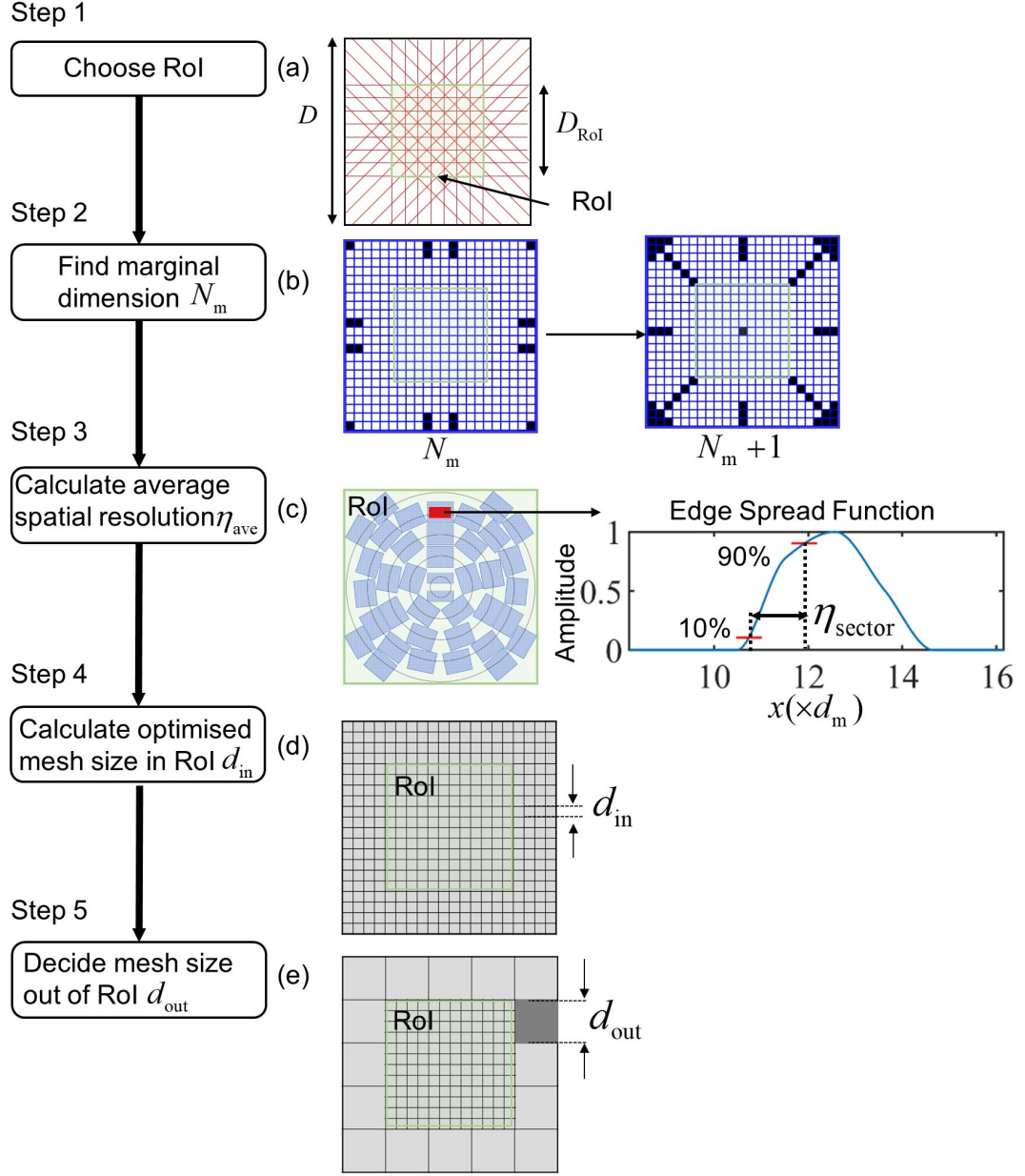


Figure 5.1: Flow chart of the proposed 5-step size-adaptive hybrid meshing scheme. (a) Sensing region and beam arrangement; (b) process of N_m determination; (c) demonstration of the edge spread function; (d) meshing with given d_{in} ; (e) finally discretised hybrid-size meshes.

with a step size of 1, the mesh size in the RoI gradually decreases. When the pixel number reaches N_m , all the pixels in the RoI have at least one beam passing through. N_m is the target marginal dimension. Given $N = N_m + 1$, it is the first time that one or more pixels in the RoI have no beam passing through. This threshold can be found by summing up the chord lengths of all the Z beams in the n^{th} pixel. Figure 5.1 (b) shows the threshold for the given beam arrangement when the discretisation of the RoI changes from $N_m \times N_m$ to $(N_m + 1) \times (N_m + 1)$. The pixels are shaded as black and white for $\sum_z \mathbf{L}_{z,n} = 0$ and $\sum_z \mathbf{L}_{z,n} \neq 0$, respectively.

Step 3: Calculate average spatial resolution in RoI, noted as η_{ave} . As demonstrated in Figure 5.1 (c), the RoI is divided into multiple sectors for evaluating the local spatial resolution, noted as η_{sector} . η_{ave} is calculated by averaging η_{sector} of all sectors. Previous studies on the spatial resolution of LAS tomographic systems [85; 102] proposed a quantified method for defining segmentation sectors in the sensing region based on theoretical estimation of spatial resolution. η_{sector} is evaluated by the “rise time”, i.e. interval between 10% and 90% maximum of the Edge Spread Function (ESF), extracted from the reconstruction of a sharp-edge inhomogeneity. For the ESF figure, the vertical axis is the normalised amplitude while the horizontal axis is the linear distance with the size of each mesh, $d_m = D/N_m$, as unit.

Step 4: Calculate optimised mesh size in the RoI, d_{in} . The averaged spatial resolution η_{ave} quantifies how fine the reconstruction can be spatially resolved in the RoI with the given beam arrangement [85]. d_{in} is derived by

$$d_{\text{in}} = \eta_{\text{ave}} \times d_m \quad (5.1)$$

Step 5: Decide mesh size out of the RoI, d_{out} . To minimise the rank deficiency of the LAS tomographic inverse problem, d_{out} should be set by (a) making all the pixels in the out-of-RoI region have laser beams passing through, (b) reflecting the potentially existing background variations. For simplicity, d_{out} can be set as an integer multiply d_{in} , e.g. $d_{\text{out}} = 4 \times d_{\text{in}}$ shown in Figure 5.1 (e).

The proposed 5-step size-adaptive hybrid meshing scheme enables three major advantages: First, the computational efficiency is maximised with a given beam arrangement by well balancing the sizes and numbers of meshes in and out of the RoI. Second, reconstruction in the RoI is highlighted with better spatial resolution, while the physical integrity of the out-of-RoI absorption is maintained. Third, the quality of the whole reconstructed image can be improved, verified later in sections, as the hybrid-

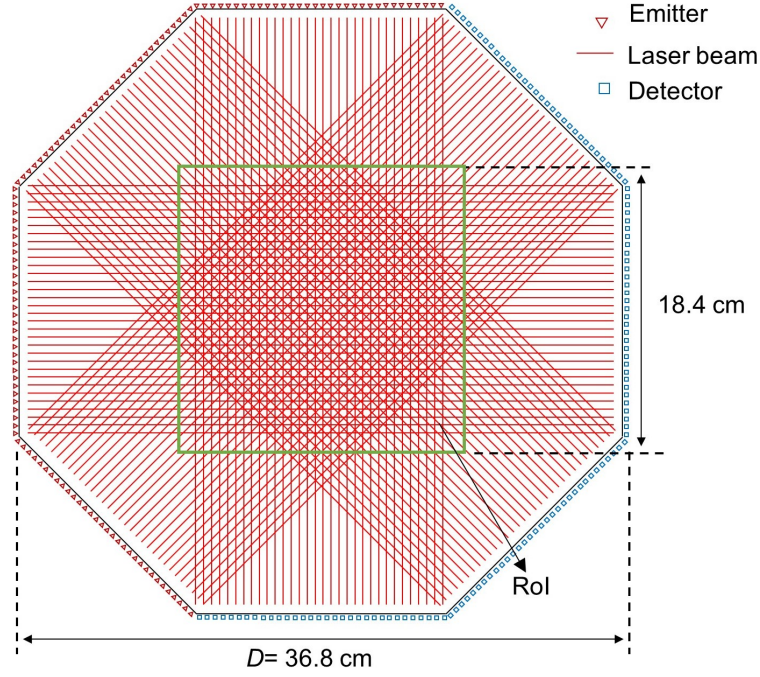


Figure 5.2: An example 128-way LAS tomographic sensor with RoI in the beam-dense region.

size meshing scheme significantly reduces the rank deficiency of the inverse problem. For some special cases where multiple flames are distanced, more segmentations may be needed in the sensing region. It is also noteworthy that the meshing scheme can be extended to three or more mesh sizes by following similar customisation. For example, we should also firstly find the RoIs (Step 1 in Figure 5.1), and then find the marginal mesh sizes (three or more) of all the RoIs for the specific given beam arrangement (Step 2). Similarly, the local spatial resolution η_{sector} and thus the averaged spatial resolution in each individual RoI η_{ave} should be quantified by following Step 3 for each individual RoI. With η_{ave} in hand, the optimised mesh size for each RoI is determined in Step 4. Finally, the mesh size for the background in Step 5 should be set to be compatible with all the dimensions of the finer meshes in the RoIs. However, this requires more prior information about the target flows and pre-determined beam arrangement. It will also introduce a more complex computation of the sensing matrix \mathbf{L} .

To mathematically validate the above-mentioned benefits, an example is introduced using a 128-way LAS tomographic sensor. As shown in Figure 5.2, a parallel beam arrangement is used with 128 laser beams arranged in 4 equiangular projection angles, each angle with 32 equispaced parallel beams. This parallel beam arrangement is a

cost-effective optical layout for LAS tomography, which has been widely adopted for the tomographic sensor design in practical applications [95; 103]. The angular spacing between each projection angle is 45° , while the beam spacing within a projection angle is 0.4 cm. The distance between each pair of laser emitter and detector noted as D , is 36.8 cm, enclosing the octagonal RoS.

For this exemplified LAS tomographic sensor, the 5-step meshing scheme is detailed as follows: (a) To cover the target flow, the side length of the RoI is set as $D_{\text{RoI}} = 18.4$ cm. (b) The enumeration starts from $N = 1$. When $N = 128$, some pixels in the RoI have no laser beam passing through, giving $N_m = 127$ and thus $d_m = 0.29$ cm. (c) As illustrated in Figure 5.1 (c), 38 rectangular sectors with dimensions of 2 cm \times 3 cm are segmented in the RoI. A small rectangular phantom perpendicular to the length of the sector with the edge of phantom cutting the middle of the sector at half-width is used to provide a sharp edge for reconstruction [85]. The calculated η_{sector} values are shown in Table 5.1. η_{ave} , equaling to 3.13, is obtained by averaging the 38 η_{sector} . (d) d_{in} is obtained by Equation 5.2, giving $d_{\text{in}} = 3.13 \times d_m = 0.91$. For simplicity, the RoS is discretised into an integer number of pixels by taking $d_m = 0.92$ cm. (e) d_{out} is chosen to be $4 \times d_{\text{in}} = 3.68$ cm for mitigating rank deficiency as well as reflecting the potentially existing background variations. As a result, dense pixels with dimensions of 0.92 cm \times 0.92 cm are deployed in the RoI, as shown in Figure 5.3 (a). Sparse pixels with dimensions of 3.68 cm \times 3.68 cm are deployed out-of-RoI region. The RoS is discretised into 628 pixels, with 576 pixels in the RoI, noted as P_{RoI}^H , and 52 pixels out of the RoI.

No.	1	2	3	4	5	6	7	8	9	10
η_{sector}	2.6	2.6	2.8	2.9	3	3	2.9	2.8	3.2	2.9
No.	11	12	13	14	15	16	17	18	19	20
η_{sector}	3.1	3.1	3.1	3.1	2.9	3.2	3	3.1	3.2	3.2
No.	21	22	23	24	25	26	27	28	29	30
η_{sector}	3	3.2	3.2	3.1	3.1	3.2	3.2	3	3.2	3.2
No.	31	32	33	34	35	36	37	38		
η_{sector}	3.1	3.6	3.6	3.5	3.5	3.6	3.5	3.6		

Table 5.1: η_{sector} values in the 38 selected sectors.

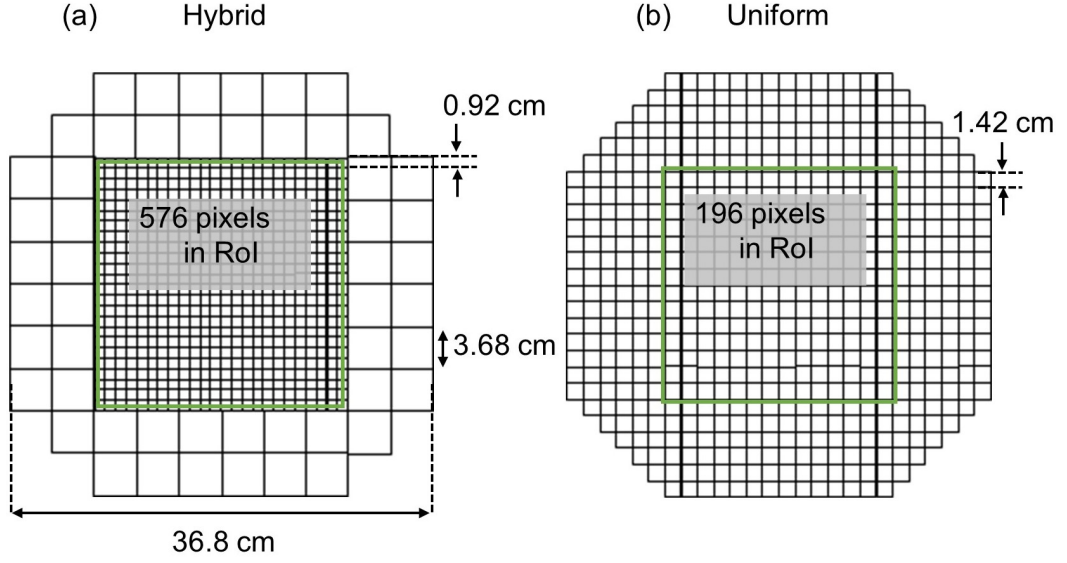


Figure 5.3: Discretised RoS with (a) hybrid-size meshes and (b) uniform-size meshes.

In comparison with the size-adaptive hybrid meshing, the RoS with uniform-size meshes is given in Figure 5.3 (b). To achieve a similar number of pixels with the hybrid-size meshing, the uniform-size meshing scheme discretises the RoS in Figure 5.3 (b) into 592 pixels with dimensions of $1.42 \text{ cm} \times 1.42 \text{ cm}$, from which 196 pixels are in the RoI, noted as $P_{\text{RoI}}^{\text{U}}$. Compared with the hybrid-size meshing, the uniform-size meshing has 36 fewer pixels in the RoS. Given the same number of laser beams, the slightly larger number of pixels actually results in more undetermined solutions compared with the uniform-size meshing scheme. However, as validated later, the improvement achieved by the proposed size-adaptive meshing on the image quality significantly outweighs this defect.

Fundamentally, the hybrid-size meshing scheme modifies the structure of the sensing matrix \mathbf{L} . Given Z laser beams, the sensing matrix for the hybrid-size meshing scheme, noted as $\mathbf{L}_{\text{hybrid}}$, is obtained by concatenating the sensing matrix in the RoI, $\mathbf{L}^{\text{in}} \in \mathbb{R}^{Z \times P_{\text{RoI}}^{\text{H}}}$, with that out of the RoI, $\mathbf{L}^{\text{out}} \in \mathbb{R}^{Z \times (N - P_{\text{RoI}}^{\text{H}})}$.

$$\mathbf{L}_{\text{hybrid}} = \begin{bmatrix} l_{1,1}^{\text{in}} & \cdots & l_{1,P_{\text{RoI}}^{\text{H}}}^{\text{in}} & l_{1,(P_{\text{RoI}}^{\text{H}}+1)}^{\text{out}} & \cdots & l_{1,N}^{\text{out}} \\ \vdots & \ddots & \vdots & \vdots & \ddots & \vdots \\ l_{Z,1}^{\text{in}} & \cdots & l_{Z,P_{\text{RoI}}^{\text{H}}}^{\text{in}} & l_{Z,(P_{\text{RoI}}^{\text{H}}+1)}^{\text{out}} & \cdots & l_{Z,N}^{\text{out}} \end{bmatrix}, \quad (5.2)$$

$$\underbrace{\mathbf{L}^{\text{in}} \in \mathbb{R}^{Z \times P_{\text{RoI}}^{\text{H}}}}_{\mathbf{L}^{\text{in}} \in \mathbb{R}^{Z \times P_{\text{RoI}}^{\text{H}}}} \quad \underbrace{\mathbf{L}^{\text{out}} \in \mathbb{R}^{Z \times (N - P_{\text{RoI}}^{\text{H}})}}_{\mathbf{L}^{\text{out}} \in \mathbb{R}^{Z \times (N - P_{\text{RoI}}^{\text{H}})}}$$

where l^{in} and l^{out} are the elements in \mathbf{L}^{in} and \mathbf{L}^{out} , denoting the chord lengths of the laser paths in a pixel in and out of the RoI, respectively. Given $P_{\text{RoI}}^{\text{H}} = 576$ for the hybrid-size meshes shown in Figure 5.3 (a), the numbers of columns in \mathbf{L}^{in} and \mathbf{L}^{out} are 576 and 52, respectively.

Similarly, the sensing matrix of the uniform-size meshing scheme noted as $\mathbf{L}_{\text{uniform}}$, can be described as:

$$\mathbf{L}_{\text{uniform}} = \begin{bmatrix} l_{1,1}^{\text{in}} & \cdots & l_{1,P_{\text{RoI}}^{\text{U}}}^{\text{in}} & l_{1,(P_{\text{RoI}}^{\text{U}}+1)}^{\text{out}} & \cdots & l_{1,N}^{\text{out}} \\ \vdots & \ddots & \vdots & \vdots & \ddots & \vdots \\ l_{Z,1}^{\text{in}} & \cdots & l_{Z,P_{\text{RoI}}^{\text{U}}}^{\text{in}} & l_{Z,(P_{\text{RoI}}^{\text{U}}+1)}^{\text{out}} & \cdots & l_{Z,N}^{\text{out}} \end{bmatrix}, \quad (5.3)$$

$$\underbrace{\mathbf{L}^{\text{in}} \in \mathbb{R}^{Z \times P_{\text{RoI}}^{\text{U}}}}_{\mathbf{L}^{\text{in}} \in \mathbb{R}^{Z \times P_{\text{RoI}}^{\text{U}}}} \quad \underbrace{\mathbf{L}^{\text{out}} \in \mathbb{R}^{Z \times (N - P_{\text{RoI}}^{\text{U}})}}_{\mathbf{L}^{\text{out}} \in \mathbb{R}^{Z \times (N - P_{\text{RoI}}^{\text{U}})}}$$

where $\mathbf{L}^{\text{in}} \in \mathbb{R}^{Z \times P_{\text{RoI}}^{\text{U}}}$ and $\mathbf{L}^{\text{out}} \in \mathbb{R}^{Z \times (N - P_{\text{RoI}}^{\text{U}})}$ are sensing matrices in and out of the RoI for the uniform-size meshing scheme, respectively. Given $P_{\text{RoI}}^{\text{U}} = 196$, the numbers of columns in \mathbf{L}^{in} and \mathbf{L}^{out} for the uniform-size meshes shown in Figure 5.3 (b) are 196 and 396, respectively.

The performance of image reconstruction using the two meshing schemes can be quantified by plotting the singular values of the sensing matrices. For simplicity, the last nontrivial rows in both matrices obtained from the two meshing schemes are duplicated and extended into the dimensions of $N \times N$. N equals 628 and 592 for the hybrid-size and uniform-size meshes, respectively. As a result, both yield N singular values in the diagonal δ . Figure 5.4 shows the singular values σ_n ($n = 1, 2, \dots, N$) in descending order obtained from each meshing scheme with the undetermined σ_j equaling zero. Given $n < 128$, σ_n obtained using the hybrid-size meshes are not only larger than those obtained using the uniform-size meshes but also perform a slower decay to zero. As indicated by the second term of Equation 2.48, the reduced number of small singular values imposes stronger suppression of the measurement noise, thus contributing to better image quality.

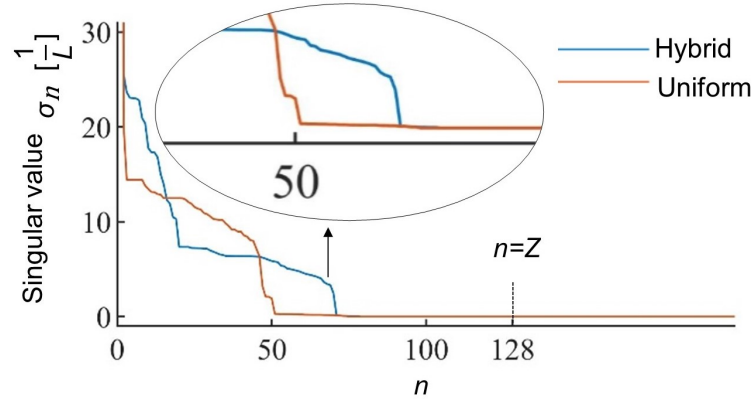


Figure 5.4: Comparison between the singular values of the sensing matrices obtained using the hybrid-size meshing scheme with 628 pixels and the uniform-size meshing scheme with 592 pixels.

5.3 Numerical Validation

Numerical simulation is first carried out to validate the proposed size-adaptive hybrid meshing scheme by reconstruction of two simulated phantoms. The reconstructed images are then quantitatively compared with those obtained using the uniform-size meshing scheme.

5.3.1 Reconstruction Algorithm

ART algorithm and smoothness regularisation mentioned in Chapter 2 are used in this chapter for reconstruction. Mathematically, the algorithm is solving a regularised minimisation problem [104]:

$$\operatorname{argmin} \left\{ \|\mathbf{B} - \mathbf{L}\mathbf{b}\|_2^2 + \varepsilon \|\mathbf{F}\mathbf{b}\|_2^2 \right\}, \text{ s.t. } \mathbf{b} \geq 0, \quad (5.4)$$

where $\|\mathbf{F}\mathbf{b}\|_2^2$ is the first-order Tikhonov regularisation term with a linear differential operator \mathbf{F} for smoothness regularisation, ε the empirically determined regularisation parameter. With \mathbf{b} in hand, the species concentration for each pixel, χ_n , can be calculated from Equation 2.40.

5.3.2 Simulation Setup

The H₂O transition centred at $\nu = 7185.6 \text{ cm}^{-1}$ is selected to reconstruct the distributions of H₂O concentration since it has appropriate line strength to give a good SNR for the LAS measurements [103].

Two phantoms of 2D distributions of the H₂O concentration are generated with one and three inhomogeneities. Each inhomogeneity is simulated by a 2D Gaussian distribution, which can be expressed as:

$$\chi(x, y) = 0.01 + 0.1 \sum_{p=1} \exp \left[-\frac{(x - x_c^p)^2 + (y - y_c^p)^2}{\xi^2} \right], \quad (5.5)$$

where x and y denote the horizontal and vertical coordinates of the RoS respectively. (x_c^p, y_c^p) is the central coordinate of the p^{th} Gaussian distribution. ξ is the standard deviation. Two high-resolution phantoms with $0.07 \text{ cm} \times 0.07 \text{ cm}$ pixel dimensions are generated for the tomographic forward problem to provide accurate modelling. The detailed parameters are shown in Table 5.2.

	$(x_c, y_c) [\text{cm}]$	$\xi [\text{cm}]$
Phantom 1	(0, 0)	3.68
Phantom 2	(-2.3, 4)	2.2
	(-2.3, -4)	2.2
	(4.6, 0)	2.2

Table 5.2: Simulation parameters of the two phantoms in Figure 5.6.

5.3.3 Metrics for Image Quality Quantification

Three metrics are used to quantitatively evaluate the quality of the tomographic image [59].

Image Error (IE): IE is defined as the normalised root mean square error between the reconstructed and the true images:

$$\text{IE} = \frac{1}{N} \sum_{n=1}^N \frac{\sqrt{(\chi_n^{\text{rec}} - \chi_n^{\text{true}})^2}}{\chi_n^{\text{true}}}, \quad (5.6)$$

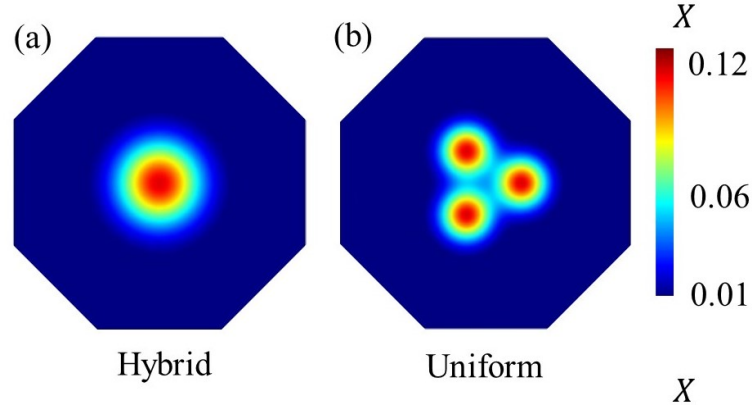


Figure 5.5: Simulated phantoms of 2D distributions of H₂O concentration with (a) one homogeneity (b) three homogeneities, respectively.

where χ_n^{rec} and χ_n^{true} refer to the reconstructed and true H₂O concentration at n^{th} pixel, respectively.

DisLoCation (DLC): DLC characterises the relative error of the centroid locations between the reconstructed inhomogeneity (x_r, y_r) and that of true inhomogeneity (x_c, y_c). The centroid of the Gaussian-shaped inhomogeneity in the phantoms coincides with its centre.

$$\text{DLC} = \sqrt{(x_r - x_c)^2 + (y_r - y_c)^2}, \quad (5.7)$$

Centroid Value Error (CVE): CVE calculates the relative difference of concentration values at the centroids of the reconstructed inhomogeneity $\chi^{\text{rec}}(x_r, y_r)$ and that of the true inhomogeneity $\chi^{\text{true}}(x_c, y_c)$.

$$\text{CVE} = \frac{|\chi^{\text{rec}}(x_r, y_r) - \chi^{\text{true}}(x_c, y_c)|}{|\chi^{\text{true}}(x_c, y_c)|} \quad (5.8)$$

For phantoms with multiple inhomogeneities, CVE is calculated by the mean value of each Gaussian-shaped inhomogeneity.

5.3.4 Simulation Results and Discussion

In the simulation, the phantoms shown in Figure 5.5 are reconstructed using both the proposed size-adaptive hybrid meshing scheme and the uniform-size meshing scheme.

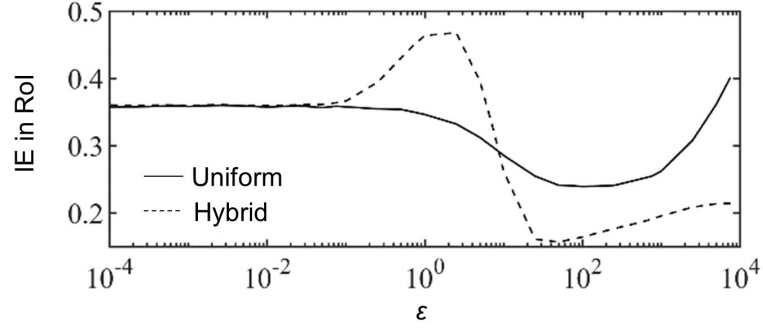


Figure 5.6: Dependence of IE on ε in the RoI for the uniform-size and hybrid-size meshing schemes.

Since the regularisation parameter ε in Equation 5.4 plays an important role in image reconstruction [59; 105], the optimal ε is selected for each phantom based on quantification of IE in the RoI. Figure 5.6 shows the dependence of IE on ε for the uniform-size and hybrid-size meshing schemes, respectively. The IE value is obtained by averaging the results from 50 repetitive reconstructions of each simulated phantom with the SNR of the line-of-sight LAS measurements set to 40 dB. When ε varies from 10^{-4} to 10^4 with 32 uniform steps of logarithmic increment, the value of the IEs for each given ε is interpolated as the curve shown in Figure 5.6. As ε varies, when $\varepsilon < 1$, the IEs from both methods are almost the same. Nevertheless, within the range of ε from 1 to 10, the IE in hybrid reconstruction surpasses that obtained from using the uniform method. This divergence is essentially due to an uneven distribution of the hybrid meshing. Since the IE during this range is sufficiently high to be considered erroneous reconstruction, ε would not be utilised for either method. The optimal ε is selected where the minimum values of the mean IEs are obtained. The minimum mean IEs, i.e., $IE = 0.24$ and $IE = 0.15$, are obtained for the uniform-size and the hybrid-size meshing schemes given $\varepsilon = 100$ and $\varepsilon = 50$, respectively.

Figure 5.7 shows the reconstructed images of the two phantoms in Figure 5.5 with the two meshing schemes. Overall, the hybrid-size meshing scheme significantly outperforms the uniform-size meshing scheme in the following two aspects: (a) finer details of the inhomogeneities; (b) better retrieval accuracy of the pixel-wised concentration. Moreover, the performances of the two meshing schemes are quantified using simulated LAS measurements contaminated with different levels of noise. Figure 5.8 (a)-(c) show the average IEs, DLCs and CVEs of reconstructed distributions of H_2O concentration at different SNRs, respectively. The value of each IE, DLC and CVE at a given SNR is the average of values obtained from the reconstruction of the above-

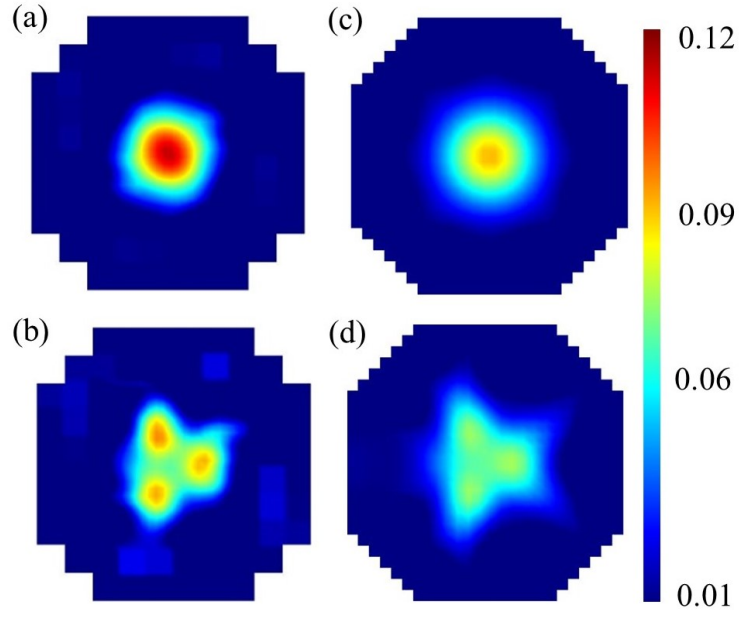


Figure 5.7: Reconstructions of the phantoms in Figure 5.5 using (a, b) the proposed size-adaptive hybrid meshing scheme and (c, d) uniform-size meshing scheme.

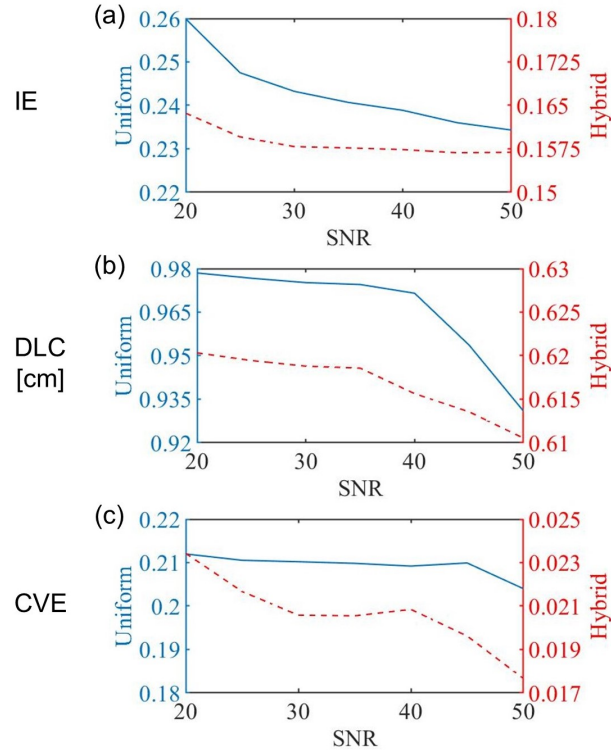


Figure 5.8: Comparison of (a) IE in RoI (b) DLC (c) CVE with uniform-size and hybrid-size meshing schemes at different measurement SNRs.

mentioned two phantoms. The difference in the dual y-axis indicates that the hybrid-size meshing scheme gives significantly lower values at all three metrics. For practical LAS measurements with SNRs better than 35 dB [95], the hybrid-size meshing lowers IE by 35%. In addition, hybrid-size meshing lowers the DLC by about 38% at any given SNRs, compared with those obtained by uniform-size meshing. As shown in Figure 5.8 (c), the hybrid-size meshing gives CVE values one order of magnitude lower than those obtained using the uniform-size meshing, indicating better accuracy of the retrieved peak values [59].

5.4 Experimental Validation

The effectiveness of the proposed size-adaptive hybrid meshing scheme is further examined by reconstructions of practical H₂O evaporation processes. The practical distributions of H₂O concentration in diffusion flows are acquired by LES via Fire Dynamic Simulator (FDS) [106; 107]. The experimental domain is a $36.8 \times 36.8 \times 10 \text{ cm}^3$ rectangular space discretised into $280 \times 280 \times 20$ pixels. The domain is filled with air with its top and four side boundaries opened. The temperature and H₂O mole fraction in the background are considered uniform with 294.15 K and 0.01, respectively. To generate the inhomogeneous H₂O distributions, H₂O is jetted from a circular inlet at the bottom of the domain with a constant velocity. The cross-section for tomography is set at 1 cm above the inlet. In this work, two scenarios are considered, one with the inlet located at the centre, the other with the inlet located at the bottom right of the centre. Table 5.3 details the inlet radius, r [cm], central location of the inlet, (x, y) [cm], and the jet velocity, v [m/s] for each scenario. To obtain high-accuracy path integrated absorption, two sets of high-resolution phantoms are generated with 10,136 pixels in the RoS, each with $0.13 \text{ cm} \times 0.13 \text{ cm}$. Measurements are taken with 35 dB SNR to consider practical noise [95]. For both scenarios, the videos in Media 1 and Media 2, shown in Appendix A, start by jetting the H₂O from the inlet and recording a total of consecutive 50 frames sampled at an interval of 0.2 s. Two instantaneous distributions of H₂O concentration, the 35th frame of the first scenario and 15th of the second scenario are shown in Figure 5.9 (a) and (d), as representative demonstrations.

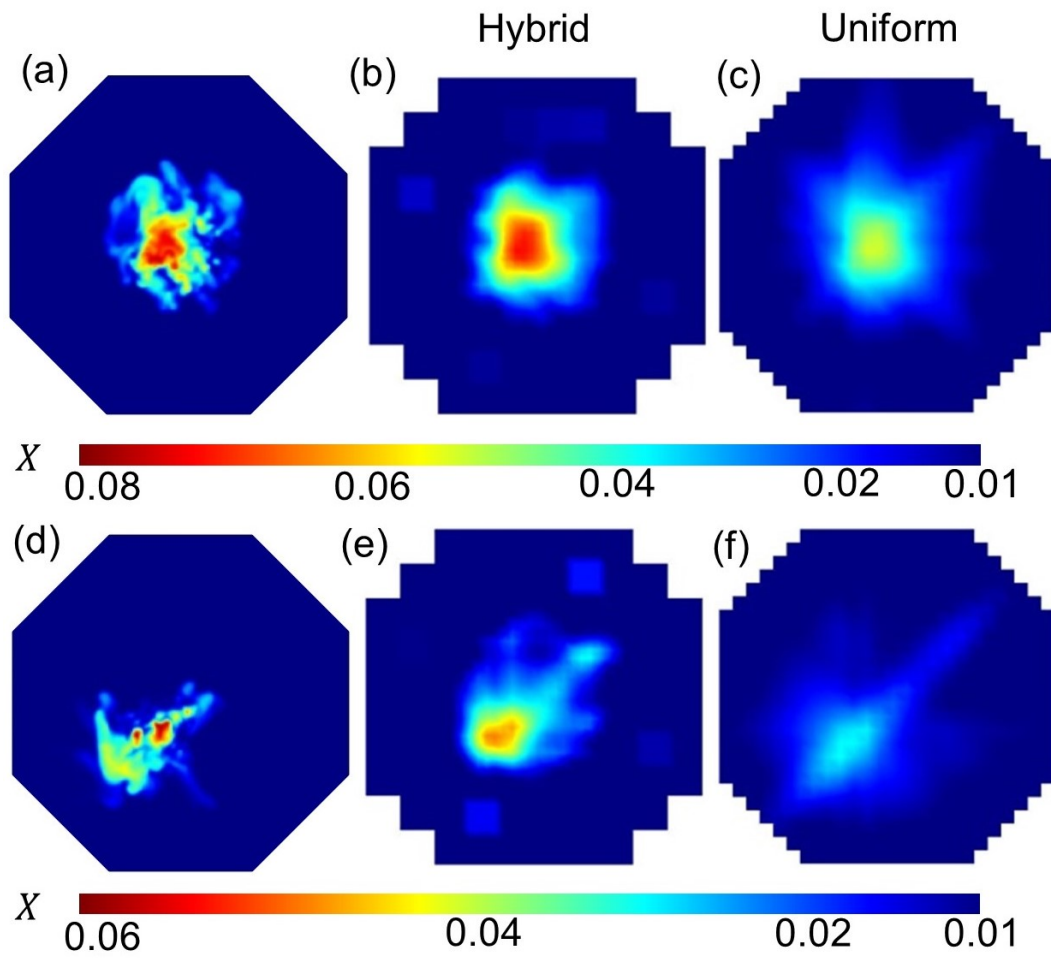


Figure 5.9: Reconstruction of (a, d) two experimental H_2O phantoms simulated via FDS using the (b, e) hybrid-size and (c, f) uniform-size meshing schemes.

	r [cm]	(x, y) [cm]	v [m/s]
Scenario 1	5	(0, 0)	0.25
Scenario 2	4	(-3, -3)	0.25

Table 5.3: Simulation parameters of the two scenarios.

	Meshing	IE	DLC [cm]	CVE
Scenario 1	Uniform	0.32	1.13	0.27
	Hybrid	0.28	0.54	0.12
Scenario 2	Uniform	0.50	1.23	0.45
	Hybrid	0.46	0.68	0.20

Table 5.4: Quantitative comparison between the hybrid-size and uniform-size meshing schemes for two scenarios.

As detailed previously, the optimal regularisation parameters ε in Equation 5.4 are set as 100 and 50 for the uniform-size and hybrid-size meshing schemes, respectively. As shown in Figure 5.9 (b) and (e), reconstructed H_2O distributions using the hybrid-size meshing scheme reveal more details of the H_2O jet diffusion in the RoI and have fewer artefacts in the background, compared with those obtained using the uniform-size meshing scheme. For scenario 1, the peak value in Figure 5.9 (b), 0.07, is closer to the true value of 0.072 in Figure 5.9 (a), indicating a more convincing retrieval of the H_2O concentration. The finer resolved pixels in the RoI also enable a much clearer boundary of the inhomogeneity, compared with the over-diffused boundary in Figure 5.9 (c). For scenario 2, the hybrid-size meshing scheme is superior for revealing the profile of the H_2O inhomogeneity, with the diffusion towards the upper right of the sensing region clearly observed in Figure 5.9 (e). In contrast, the uniform-size meshing can only give a blur and expanded shape of the target inhomogeneity in Figure 5.9 (f) with the absolute H_2O concentration values severely deviated from the truth. Both cases indicate that the reconstructed images using the hybrid-size meshing can characterise the gradient of H_2O concentration around the vapour injector, while those

reconstructed using the uniform-size meshing suffer from a much lower peak value and a severely blurred boundary of the inhomogeneity. Therefore, the experimental results show the adapted hybrid mesh size for LAS tomography is better at detailing the profiles of the target flows with improved quality of reconstructed images.

As shown in Media 1 and Media 2, the consecutively reconstructed images using the proposed hybrid-size meshing scheme can reveal more structural information about the cross-sectional variation of H_2O concentration. For the whole H_2O evaporation process, the absolute concentration of the inhomogeneity retrieved by the hybrid-size meshing scheme is closer to the truth. Table 5.4 shows the quantitative performance evaluation, e.g., IE, DLC, CVE, of the two scenarios averaged for 50 frames using the proposed hybrid-size meshing and uniform-size meshing schemes, respectively. For both scenarios, the hybrid-size meshing gives about 8% lower IE, and halves DLC and CVE than the uniform-size meshing, which indicates better accuracies for pixel-wised reconstruction, target location and peak value.

5.5 Summary

A size-adaptive hybrid meshing scheme was proposed to bridge the research gap in the reconstruction of regions outside the RoI. Driven by the required spatial resolution, 5 steps were proposed in this work to quantitatively customise the mesh size in and out of the RoI. This customisation approach mitigates the rank deficiency in the tomographic inverse problem by minimising undetermined solutions and ensuring smoother singular value distribution, thus enhancing the accuracy of tomographic reconstruction while preserving physical integrity during the process.

The 5-step size-adaptive hybrid meshing scheme was numerically demonstrated by applying it to a 128-beam LAS tomographic sensor. It was firstly validated by reconstructing phantoms of 2D Gaussian distributions of H_2O concentration using both the proposed hybrid-size and the traditionally uniform-size meshing schemes. The numerical results show the superiority of the size-adaptive hybrid meshing scheme with 35% lower image error and 38% less significant dislocation at typical 35 dB SNR, as well as the more accurate peak values, compared with the uniform-size meshing. Furthermore, experimental validation was carried out by consecutive reconstruction

of practical transpiration-introduced H_2O , which is generated by FDS. The reconstruction using the size-adaptive hybrid meshing scheme significantly outperformed the uniform-size meshing, with finer details, clearer boundaries and more accurate concentration of the target flow fields.

Chapter 6

Conclusion and Future Work

6.1 Conclusion

The LAS technology has demonstrated significant advantages in the field of industrial combustion diagnosis due to its non-invasive, accurate, fast, and robust characteristics. However, utilisation of LAS technology for tomographic reconstruction encounters limitations arising from the dimensions of fibre optics and optical access in specific application scenarios. Insufficient measurements present a primary challenge in LAS tomographic reconstruction. To further enhance the applicability of the LAS technique and improve the reconstruction quality of LAS tomography, this thesis developed tomographic systems and reconstruction methods that can adapt the spatial resolution of the reconstruction to different requirements. The detailed contributions of this thesis are summarised as follows.

The fundamentals of LAS tomography, the existing LAS tomographic systems, and the state-of-the-art LAS tomographic reconstruction algorithms were first reviewed. The review helped to build an understanding of recent developments in LAS tomographic systems and provided the background for the innovative work demonstrated in this thesis.

The primary objective of this thesis revolved around the design of a LAS tomographic sensor, which begins with an overview of the principal components and design considerations. Additionally, a sample design of a 32-channel laboratory sensor was presented as an illustrative example. Expanding upon the laboratory sensor design, a modular design for the emitter and receiver of the optical sensor was proposed. By reducing the beam spacing to 1 cm, the spatial resolution of the detection was enhanced, resulting in greater reconfigurability of the system. This modular design facilitated increased flexibility and adaptability across various applications. The performance of the prototype sensor was evaluated through measurements of temperature and H₂O

concentration in the ambient. The obtained results exhibited consistent and accurate measurements, validating the reliability of the sensor design. These findings affirmed the effectiveness of the proposed modular design. Additionally, by adapting the design principles and adjusting the sensor count, the tomographic system can be expanded to accommodate more beam counts for large measurement areas.

The sensor design was further verified through its application in simultaneously detecting H_2O concentration and temperature in the exhaust of commercial APU. A LAS sensor was developed using 8 laser beams targeting 3 transitions of H_2O . The sensor was validated via *in situ* test on a commercial APU. Seven parallel laser beams at 5000.2 cm^{-1} were 6.3 mm spaced at the plume boundary to characterise the edge effect between the hot exhaust plume and cold surrounding flow. One beam, operating at the dual wavenumbers of 7185.6 cm^{-1} and 7444.36 cm^{-1} penetrated the plume through the plume centre to measure temperature via ratio thermometry and then uses this temperature information to obtain the concentration of H_2O . A temporal resolution of 4 milliseconds was achieved for the 8-beam measurement, enabling high-speed and simultaneous quantification of the edge effects and the exhaust parameters. Results indicated that H_2O concentration and temperature in the exhaust measured by the developed sensor were highly consistent with the traditional benchmarks, e.g., extractive sampling and thermocouples, with a difference of 0.02% and 3°C , respectively. Enabled by its continuous millisecond-level measurements, the sensor, for the first time, revealed hidden engine behaviours and combustion dynamics that were unable to be observed by the traditional methods, thus facilitating next-generation real-time gas turbine engine control towards low emissions.

Beyond sensor design, driven by the customised spatial resolution of the sensing region, a size-adaptive hybrid grid scheme for LAS tomography was proposed to improve the quality of the reconstruction. Traditionally, the entire sensing region for LAS tomography was uniformly discretised with the empirically determined density of the meshes. Such a discretisation results in a) waste of computational efforts on the less spatially resolved location, and b) much severer rank deficiency. To solve the above-mentioned issues, we introduced, for the first time, a size-adaptive hybrid meshing scheme for LAS tomography. Dense meshes were deployed in the RoI to detail the target flow field while sparse ones were deployed out of the RoI to fully consider the physically existing laser absorption. The proposed scheme was numerically validated using a LAS tomographic sensor with 128 laser beams. The visual and quantitative metric comparisons showed that the proposed hybrid-size meshing

scheme outperforms the traditionally uniform-size meshing scheme, giving 35% lower image error and 38% less significant dislocation at a typical 35 dB signal-to-noise ratio in the RoI. The proposed hybrid-size meshing scheme significantly facilitated the reconstruction of the industrial combustion processes where the combustion zone is bypassed by cooling flows. In these scenarios, the proposed scheme could adapt a finer resolution to detail the combustion zone, while maintaining the integrity of the physical model by less resolved reconstruction of the bypass flows.

In conclusion, the system and the methods developed in this thesis realised the customisation of the reconstruction spatial resolution and improvement of reconstruction quality based on different requirements. There are also many further extensions and potential applications of these systems and methods, which will be discussed in the next section.

6.2 Future Work

Although this thesis has significantly improved the performance of LAS tomographic imaging with the developed techniques, investigations are still necessary to further advance this work in the following areas.

Based on the principles of modular design and the 128-way tomographic system discussed in Chapter 3, additional efforts are needed to develop a prototype of a 128-way LAS tomographic sensor. This sensor will enable the capture of high-resolution images of larger objects, expanding the range of objects that can be measured and analysed using LAS tomography. This capability is particularly valuable in industrial applications where the examination of large-scale objects is required. Additionally, the flexibility of the sensor allows for customisation and adaptation to specific measurement needs.

In future endeavours, the 128-way sensor can be effectively utilised for detecting and analysing the exhaust gas properties of APUs. By employing this sensor, it becomes feasible to reconstruct the distribution of temperature and the concentration of H_2O and CO_2 in the exhaust gas. The measurement and analysis of these gas properties hold great significance in analysing the combustion behaviour of the engine, especially under various fuel conditions. Through obtaining the temperature distribution,

researchers can gain valuable insights into the thermal characteristics of the combustion process and evaluate the efficiency of the APU. This application of the 128-way sensor contributes to a deeper understanding of APU performance and assists in optimising its operation.

To capture the complete combustion behaviour, it is recognised in the thesis that LAS sensors are capable of detection in three-dimensional. While the sensor described in the thesis effectively performs tomographic reconstruction in the radial direction of the flame, it is crucial to consider the combustion phenomena that occur in the axial direction of the flame as well. Therefore, there is a need for the development of a 3D LAS sensor to address this challenge.

Incorporating spatial detection capabilities in a 3D LAS sensor, the development of new 3D reconstruction algorithms becomes crucial. These algorithms allow for the reconstruction of temperature and gas properties' distributions not only in the radial direction but also in the axial direction of the flame. This three-dimensional perspective provides a more accurate and detailed representation of the combustion process. The utilisation of these new 3D reconstruction algorithms, along with the spatial detection capabilities of the LAS sensor, opens up possibilities for in-depth analysis of combustion phenomena, such as flame structure and mixing patterns in a three-dimensional space. It enhances our understanding of the complex dynamics of combustion and facilitates the development of more efficient and cleaner combustion technologies.

Appendix A

Reconstruction of FDS-Simulated Water Vapour

For both scenarios, videos start by jetting the H_2O from the inlet. Both videos recorded a total of consecutive 50 frames sampled at an interval of 0.2 s.

The full videos are download available from:

Media 1: <http://10.1109/JSEN.2022.3176116/mm1>

Media 2: <http://10.1109/JSEN.2022.3176116/mm2>

5 snapshots of the first frame in each second from both videos are given below.

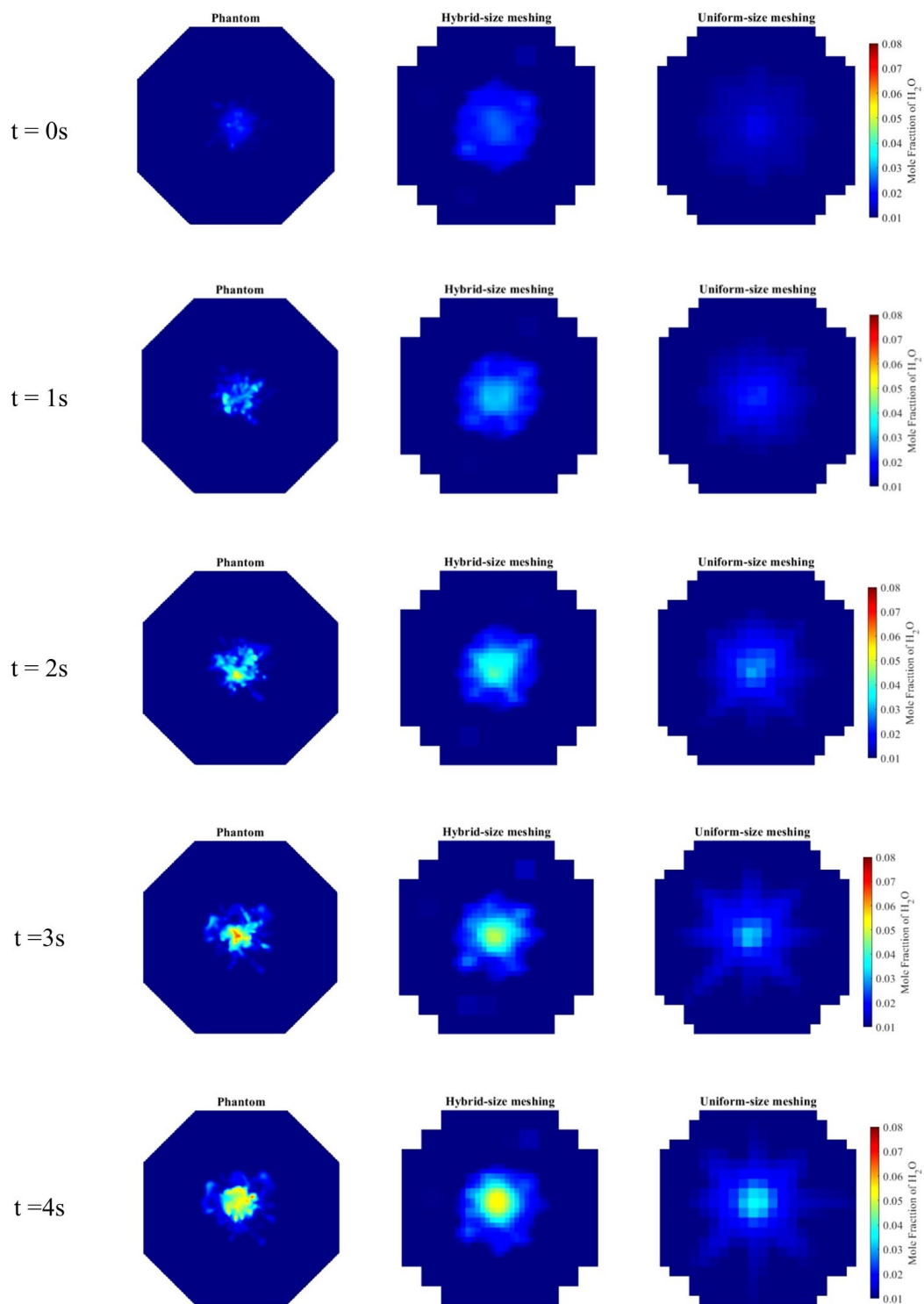


Figure A.1: Snapshots for Media 1.

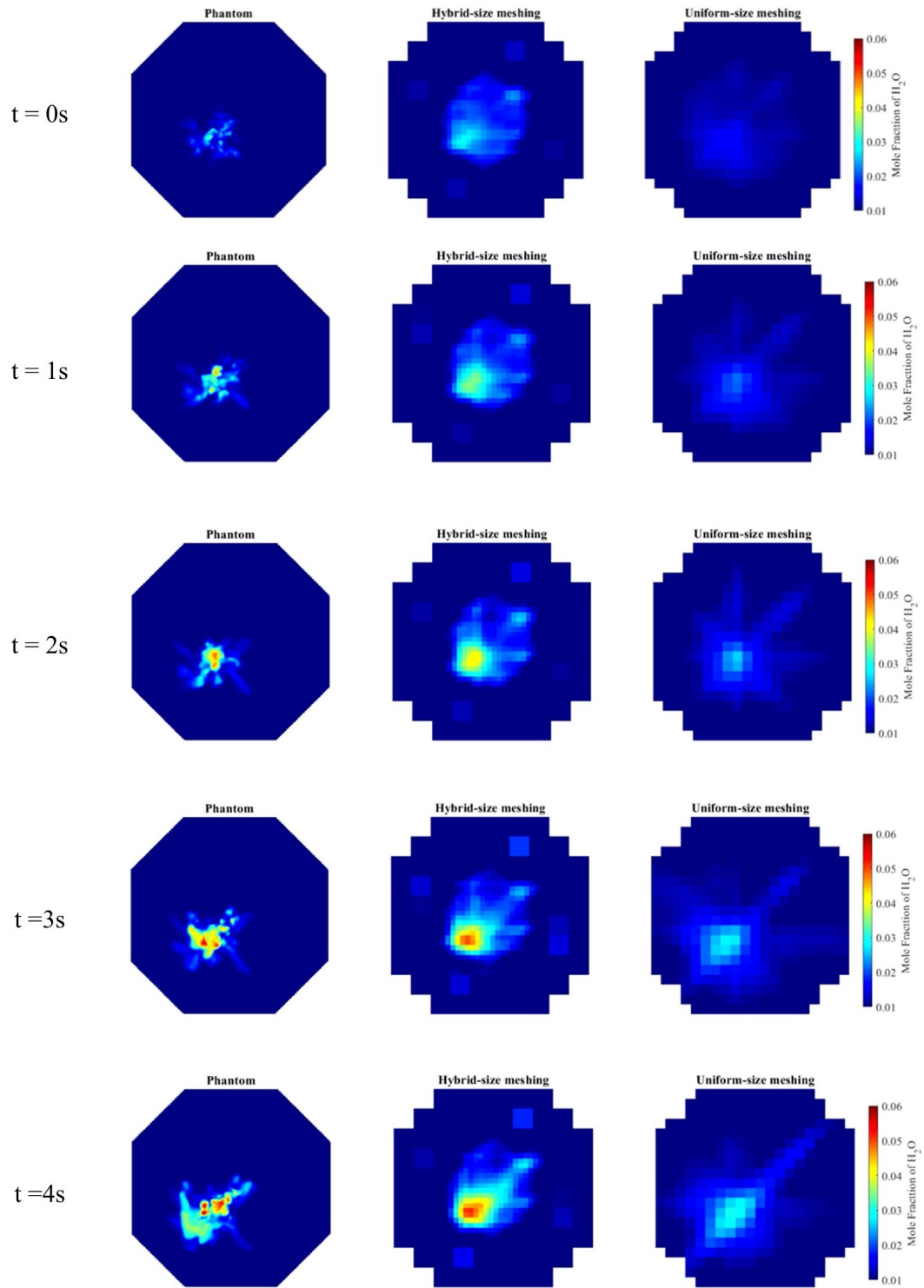


Figure A.2: Snapshots for Media 2.

Bibliography

- [1] Y. Liu, X. Sun, V. Sethi, D. Nalianda, Y.-G. Li, and L. Wang, "Review of modern low emissions combustion technologies for aero gas turbine engines," *Progress in Aerospace Sciences*, vol. 94, pp. 12–45, 2017.
- [2] D. Burnes and A. Camou, "Impact of fuel composition on gas turbine engine performance," *Journal of Engineering for Gas Turbines and Power*, vol. 141, no. 10, p. 101006, 2019.
- [3] B. George and N. Muthuveerappan, "Life assessment of a high temperature probe designed for performance evaluation and health monitoring of an aero gas turbine engine," *International journal of turbo & jet-engines*, 2020.
- [4] B. Giechaskiel and M. Clairotte, "Fourier transform infrared (ftir) spectroscopy for measurements of vehicle exhaust emissions: A review," *Applied Sciences*, vol. 11, no. 16, p. 7416, 2021.
- [5] A. Rafoth, S. Gabriel, F. Sacher, and H.-J. Brauch, "Analysis of isothiazolinones in environmental waters by gas chromatography–mass spectrometry," *Journal of Chromatography A*, vol. 1164, no. 1-2, pp. 74–81, 2007.
- [6] Z. Liu, Y. Zhang, J. Fu, and J. Liu, "Multidimensional computational fluid dynamics combustion process modeling of a 6v150 diesel engine," *Journal of Thermal Science and Engineering Applications*, vol. 14, no. 10, p. 101009, 2022.
- [7] D. H. Shin, M. Kim, J. S. Kim, B. J. Lee, and J. Lee, "Precise infrared thermometry with considering background radiation for gas turbine air cooling application," *International Journal of Thermal Sciences*, vol. 158, p. 106534, 2020.
- [8] T. A. Mcmanus, I. T. Monje, and J. A. Sutton, "Experimental assessment of the tenti s6 model for combustion-relevant gases and filtered rayleigh scattering applications," *Applied Physics B*, vol. 125, no. 1, p. 13, 2019.
- [9] S. Li, Y. Li, R. Yi, L. Liu, and J. Qu, "Coherent anti-stokes raman scattering microscopy and its applications," *Frontiers in Physics*, vol. 8, p. 598420, 2020.

- [10] W. Weng, M. Alden, and Z. Li, "Quantitative so₂ detection in combustion environments using broad band ultraviolet absorption and laser-induced fluorescence," *Analytical chemistry*, vol. 91, no. 16, pp. 10849–10855, 2019.
- [11] C. Liu and L. Xu, "Laser absorption spectroscopy for combustion diagnosis in reactive flows: A review," *Applied Spectroscopy Reviews*, vol. 54, no. 1, pp. 1–44, 2019.
- [12] J. Emmert, H. Schneider, B. Böhm, A. Dreizler, and S. Wagner, "Phase-locked absorption tomography for retrieving 5 khz time-resolved tracer profiles in solid fuel combustion," *Applications in Energy and Combustion Science*, vol. 12, p. 100093, 2022.
- [13] F. Wang, K. Cen, N. Li, J. B. Jeffries, Q. Huang, J. Yan, and Y. Chi, "Two-dimensional tomography for gas concentration and temperature distributions based on tunable diode laser absorption spectroscopy," *Measurement Science and Technology*, vol. 21, no. 4, p. 045301, 2010.
- [14] K. Daun, "Infrared species limited data tomography through tikhonov reconstruction," *Journal of Quantitative Spectroscopy and Radiative Transfer*, vol. 111, no. 1, pp. 105–115, 2010.
- [15] T. Yu, W. Cai, and Y. Liu, "Rapid tomographic reconstruction based on machine learning for time-resolved combustion diagnostics," *Review of Scientific Instruments*, vol. 89, no. 4, p. 043101, 2018.
- [16] D. M. Pelt, K. J. Batenburg, and J. A. Sethian, "Improving tomographic reconstruction from limited data using mixed-scale dense convolutional neural networks," *Journal of Imaging*, vol. 4, no. 11, p. 128, 2018.
- [17] M. G. Allen, "Diode laser absorption sensors for gas-dynamic and combustion flows," *Measurement Science and technology*, vol. 9, no. 4, p. 545, 1998.
- [18] E. Hinkley, "Laser spectroscopic instrumentation and techniques: long-path monitoring by resonance absorption," *Optical and Quantum Electronics*, vol. 8, pp. 155–167, 1976.
- [19] R. Hanson, P. Kuntz, and C. Kruger, "High-resolution spectroscopy of combustion gases using a tunable ir diode laser," *Applied Optics*, vol. 16, no. 8, pp. 2045–2048, 1977.

- [20] X. Zhou, "Diode laser absorption sensors for combustion control," 2005.
- [21] R. K. Hanson, R. M. Spearrin, and C. S. Goldenstein, *Spectroscopy and optical diagnostics for gases*, vol. 1. Springer, 2016.
- [22] R. R. Gamache, R. Lynch, and S. P. Neshyba, "New developments in the theory of pressure-broadening and pressure-shifting of spectral lines of h₂O: the complex robert-bonamy formalism," *Journal of Quantitative Spectroscopy and Radiative Transfer*, vol. 59, no. 3-5, pp. 319–335, 1998.
- [23] W. G. Vincenti, C. H. Kruger Jr, and T. Teichmann, "Introduction to physical gas dynamics," 1966.
- [24] A. C. Mitchell and M. W. Zemansky, "Resonance radiation and excited atoms," *Resonance Radiation and Excited Atoms*, 2009.
- [25] J. J. Olivero and R. Longbothum, "Empirical fits to the voigt line width: A brief review," *Journal of Quantitative Spectroscopy and Radiative Transfer*, vol. 17, no. 2, pp. 233–236, 1977.
- [26] F. Mayinger, *Optical measurements: techniques and applications*. Springer Science & Business Media, 2013.
- [27] S. T. Sanders, J. Wang, J. B. Jeffries, and R. K. Hanson, "Diode-laser absorption sensor for line-of-sight gas temperature distributions," *Applied Optics*, vol. 40, no. 24, pp. 4404–4415, 2001.
- [28] X. Liu, J. Jeffries, R. Hanson, K. Hinckley, and M. Woodmansee, "Development of a tunable diode laser sensor for measurements of gas turbine exhaust temperature," *Applied Physics B*, vol. 82, pp. 469–478, 2006.
- [29] X. Liu, J. B. Jeffries, and R. K. Hanson, "Measurement of non-uniform temperature distributions using line-of-sight absorption spectroscopy," *AIAA journal*, vol. 45, no. 2, pp. 411–419, 2007.
- [30] A. Upadhyay, M. Lengden, G. Enemali, G. Stewart, W. Johnstone, D. Wilson, G. Humphries, T. Benoy, J. Black, A. Chighine, *et al.*, "Tomographic imaging of carbon dioxide in the exhaust plume of large commercial aero-engines," *Applied Optics*, vol. 61, no. 28, pp. 8540–8552, 2022.

- [31] H. Li, G. B. Rieker, X. Liu, J. B. Jeffries, and R. K. Hanson, "Extension of wavelength-modulation spectroscopy to large modulation depth for diode laser absorption measurements in high-pressure gases," *Applied optics*, vol. 45, no. 5, pp. 1052–1061, 2006.
- [32] A. P. Nair, N. Q. Minesi, C. Jelloian, N. Kuenning, and R. M. Spearrin, "Rf-waveform optimization for mhz-rate dfb laser absorption spectroscopy in dynamic combustion environments," in *AIAA Scitech 2022 Forum*, p. 2373, 2022.
- [33] G. B. Rieker, J. B. Jeffries, and R. K. Hanson, "Calibration-free wavelength-modulation spectroscopy for measurements of gas temperature and concentration in harsh environments," *Applied optics*, vol. 48, no. 29, pp. 5546–5560, 2009.
- [34] C. S. Goldenstein, C. L. Strand, I. A. Schultz, K. Sun, J. B. Jeffries, and R. K. Hanson, "Fitting of calibration-free scanned-wavelength-modulation spectroscopy spectra for determination of gas properties and absorption lineshapes," *Applied optics*, vol. 53, no. 3, pp. 356–367, 2014.
- [35] W. Wei, W. Y. Peng, Y. Wang, J. Shao, C. L. Strand, and R. K. Hanson, "Two-color frequency-multiplexed ims technique for gas thermometry at elevated pressures," *Applied Physics B*, vol. 126, no. 3, p. 51, 2020.
- [36] C. S. Goldenstein, I. A. Schultz, J. B. Jeffries, and R. K. Hanson, "Two-color absorption spectroscopy strategy for measuring the column density and path average temperature of the absorbing species in nonuniform gases," *Applied optics*, vol. 52, no. 33, pp. 7950–7962, 2013.
- [37] I. E. Gordon, L. S. Rothman, C. Hill, R. V. Kochanov, Y. Tan, P. F. Bernath, M. Birk, V. Boudon, A. Campargue, K. Chance, *et al.*, "The hitran2016 molecular spectroscopic database," *Journal of Quantitative Spectroscopy and Radiative Transfer*, vol. 203, pp. 3–69, 2017.
- [38] R. R. Gamache, B. Vispoel, M. Rey, A. Nikitin, V. Tyuterev, O. Egorov, I. E. Gordon, and V. Boudon, "Total internal partition sums for the hitran2020 database," *Journal of Quantitative Spectroscopy and Radiative Transfer*, vol. 271, p. 107713, 2021.

- [39] P. Wright, C. A. Garcia-Stewart, S. J. Carey, F. P. Hindle, S. H. Pegrum, S. M. Colbourne, P. J. Turner, W. J. Hurr, T. J. Litt, S. C. Murray, *et al.*, "Toward in-cylinder absorption tomography in a production engine," *Applied optics*, vol. 44, no. 31, pp. 6578–6592, 2005.
- [40] Y. Deguchi, T. Kamimoto, Z. Wang, J. Yan, J. Liu, H. Watanabe, and R. Kurose, "Applications of laser diagnostics to thermal power plants and engines," *Applied Thermal Engineering*, vol. 73, no. 2, pp. 1453–1464, 2014.
- [41] Z. Wang, W. Zhou, J. Yan, T. Kamimoto, K. Tsujimoto, Y. Li, Y. Deguchi, N. A. Sani, S. H. Samsuri, and M. F. Zulkifli, "Application of 2d temperature measurement to a coal-fired furnace using ct-tdlas," *Measurement Science and Technology*, vol. 31, no. 3, p. 035203, 2019.
- [42] F. Wang, Q. Wu, Q. Huang, H. Zhang, J. Yan, and K. Cen, "Simultaneous measurement of 2-dimensional h₂o concentration and temperature distribution in premixed methane/air flame using tdlas-based tomography technology," *Optics Communications*, vol. 346, pp. 53–63, 2015.
- [43] L. Xu, C. Liu, W. Jing, Z. Cao, X. Xue, and Y. Lin, "Tunable diode laser absorption spectroscopy-based tomography system for on-line monitoring of two-dimensional distributions of temperature and h₂o mole fraction," *Review of Scientific Instruments*, vol. 87, no. 1, p. 013101, 2016.
- [44] C. Liu, Z. Cao, Y. Lin, L. Xu, and H. McCann, "Online cross-sectional monitoring of a swirling flame using tdlas tomography," *IEEE Transactions on Instrumentation and Measurement*, vol. 67, no. 6, pp. 1338–1348, 2018.
- [45] W. Zhao, L. Xu, A. Huang, X. Gao, X. Luo, H. Zhang, H. Chang, and Z. Cao, "A wms based tdlas tomographic system for distribution retrievals of both gas concentration and temperature in dynamic flames," *IEEE Sensors Journal*, vol. 20, no. 8, pp. 4179–4188, 2019.
- [46] A. Huang, Z. Cao, W. Zhao, H. Zhang, and L. Xu, "Frequency-division multiplexing and main peak scanning wms method for tdlas tomography in flame monitoring," *IEEE Transactions on Instrumentation and Measurement*, vol. 69, no. 11, pp. 9087–9096, 2020.
- [47] P. Wright, N. Terzija, J. L. Davidson, S. Garcia-Castillo, C. Garcia-Stewart, S. Pegrum, S. Colbourne, P. Turner, S. D. Crossley, T. Litt, *et al.*, "High-speed chemical species tomography in a multi-cylinder automotive engine," *Chemical Engineering Journal*, vol. 158, no. 1, pp. 2–10, 2010.

- [48] F. Stritzke, S. van der Kley, A. Feiling, A. Dreizler, and S. Wagner, "Ammonia concentration distribution measurements in the exhaust of a heavy duty diesel engine based on limited data absorption tomography," *Optics express*, vol. 25, no. 7, pp. 8180–8191, 2017.
- [49] N. Terzija, J. Davidson, C. Garcia-Stewart, P. Wright, K. Ozanyan, S. Pegrum, T. Litt, and H. McCann, "Image optimization for chemical species tomography with an irregular and sparse beam array," *Measurement Science and Technology*, vol. 19, no. 9, p. 094007, 2008.
- [50] P. C. Hansen, *Rank-deficient and discrete ill-posed problems: numerical aspects of linear inversion*. SIAM, 1998.
- [51] K. J. Daun, S. J. Grauer, and P. J. Hadwin, "Chemical species tomography of turbulent flows: Discrete ill-posed and rank deficient problems and the use of prior information," *Journal of Quantitative Spectroscopy and Radiative Transfer*, vol. 172, pp. 58–74, 2016.
- [52] W. Cai and C. F. Kaminski, "Tomographic absorption spectroscopy for the study of gas dynamics and reactive flows," *Progress in energy and combustion science*, vol. 59, pp. 1–31, 2017.
- [53] T. Yu and W. Cai, "Benchmark evaluation of inversion algorithms for tomographic absorption spectroscopy," *Applied Optics*, vol. 56, no. 8, pp. 2183–2194, 2017.
- [54] A. Guha and I. M. Schoegl, "Tomographic imaging of flames: assessment of reconstruction error based on simulated results," *Journal of Propulsion and Power*, vol. 30, no. 2, pp. 350–359, 2014.
- [55] M.-G. Jeon, Y. Deguchi, T. Kamimoto, D.-H. Doh, and G.-R. Cho, "Performances of new reconstruction algorithms for ct-tdlas (computer tomography-tunable diode laser absorption spectroscopy)," *Applied Thermal Engineering*, vol. 115, pp. 1148–1160, 2017.
- [56] C. Liu, L. Xu, J. Chen, Z. Cao, Y. Lin, and W. Cai, "Development of a fan-beam tdlas-based tomographic sensor for rapid imaging of temperature and gas concentration," *Optics Express*, vol. 23, no. 17, pp. 22494–22511, 2015.

- [57] Z.-T. Niu, H. Qi, Z.-Y. Zhu, K.-F. Li, Y.-T. Ren, and M.-J. He, "A novel parametric level set method coupled with tikhonov regularization for tomographic laser absorption reconstruction," *Applied Thermal Engineering*, vol. 201, p. 117819, 2022.
- [58] W. Cai, X. Li, F. Li, and L. Ma, "Numerical and experimental validation of a three-dimensional combustion diagnostic based on tomographic chemiluminescence," *Optics express*, vol. 21, no. 6, pp. 7050–7064, 2013.
- [59] Y. Bao, R. Zhang, G. Enemali, Z. Cao, B. Zhou, H. McCann, and C. Liu, "Relative entropy regularized tdlas tomography for robust temperature imaging," *IEEE Transactions on Instrumentation and Measurement*, vol. 70, pp. 1–9, 2020.
- [60] Z. Wang, N. Zhu, W. Wang, and X. Chao, "Y-net: a dual-branch deep learning network for nonlinear absorption tomography with wavelength modulation spectroscopy," *Optics Express*, vol. 30, no. 2, pp. 2156–2172, 2022.
- [61] J. Si, A. Wang, and Y. Cheng, "Temperature imaging network based on swin transformer for tdlas tomography," in *Fourteenth International Conference on Digital Image Processing (ICDIP 2022)*, vol. 12342, pp. 796–803, SPIE, 2022.
- [62] J. Si, G. Fu, X. Liu, Y. Cheng, R. Zhang, J. Xia, Y. Fu, G. Enemali, and C. Liu, "A spatially progressive neural network for locally/globally prioritized tdlas tomography," *IEEE Transactions on Industrial Informatics*, 2023.
- [63] J. P. Molnar and S. J. Grauer, "Flow field tomography with uncertainty quantification using a bayesian physics-informed neural network," *Measurement Science and Technology*, vol. 33, no. 6, p. 065305, 2022.
- [64] C. Shui, J. Huang, H. Liu, W. Cai, and S. T. Sanders, "Tomographic absorption spectroscopy based on dictionary learning," *Optics Express*, vol. 29, no. 22, pp. 36400–36416, 2021.
- [65] U. Hartmann and J. R. Seume, "Combining art and fbp for improved fidelity of tomographic bos," *Measurement Science and Technology*, vol. 27, no. 9, p. 097001, 2016.
- [66] S. Junling, H. Yanji, X. Mingyuan, W. Guangyu, and L. Zhaoran, "Tomography system for measurement of gas properties in combustion flow field," *Chinese Journal of Aeronautics*, vol. 30, no. 5, pp. 1697–1707, 2017.

- [67] J. Huang, H. Liu, J. Dai, and W. Cai, "Reconstruction for limited-data nonlinear tomographic absorption spectroscopy via deep learning," *Journal of Quantitative Spectroscopy and Radiative Transfer*, vol. 218, pp. 187–193, 2018.
- [68] S. Schilt, L. Thevenaz, and P. Robert, "Wavelength modulation spectroscopy: combined frequency and intensity laser modulation," *Applied optics*, vol. 42, no. 33, pp. 6728–6738, 2003.
- [69] Keysight, "33522B Waveform Generator." <https://www.keysight.com/gb/en/product/33522B/waveform-generator-30-mhz-2-channel-arb.html>, 2023.
- [70] WavelengthElectronics, "LDTC 2-2 E Laser Diode Driver." <https://www.teamwavelength.com/product/ldtc-series-2-2-amp-laser-driver-thermal-control/>, 2023.
- [71] NEL, "NEL Laser Diodes NLK1E5EAAA." <https://www.ntt-electronics.com/en/products/photonics/pdf/NLK1E5EAAA.pdf>, 2005.
- [72] NEL, "NEL Laser Diodes NLK1E5GAAA." <https://www.ntt-electronics.com/en/products/photonics/pdf/NLK1E5GAAA.pdf>, 2005.
- [73] Opneti, "Single Mode Standard Coupler." <http://www.opneti.com/uploadfile/20160922/20160922022156211.pdf>, 2016.
- [74] Opneti, "1x N PLC Splitter." <http://www.opneti.com/uploadfile/20210629/20210629112046479.pdf>, 2016.
- [75] Thorlabs, "f = 4.6 mm Adjustable Aspheric Collimators." <https://www.thorlabs.com/thorproduct.cfm?partnumber=CFC5-C>, 2023.
- [76] Hamamatsu, "InGaAs PIN photodiode G12182-010K." <https://www.hamamatsu.com/jp/en/product/optical-sensors/infrared-detector/ingaas-photodiode/G12182-010K.html>, 2023.
- [77] AnalogDevices, "AD8065, High Performance, 145 MHz FastFET Op Amps." <https://www.analog.com/en/products/ad8065.html>, 2023.
- [78] R. M. Gray and D. L. Neuhoff, "Quantization," *IEEE transactions on information theory*, vol. 44, no. 6, pp. 2325–2383, 1998.

- [79] G. Enemali, R. Zhang, H. McCann, and C. Liu, "Cost-effective quasi-parallel sensing instrumentation for industrial chemical species tomography," *IEEE Transactions on Industrial Electronics*, vol. 69, no. 2, pp. 2107–2116, 2021.
- [80] RedPitaya, "Stemlab-125-10." <https://redpitaya.com/stemlab-125-10/>, 2023.
- [81] Analog, "Stabilize Your Transimpedance Amplifier." <https://www.analog.com/en/technical-articles/stabilize-transimpedance-amplifier-circuit-design.html>, 2023.
- [82] K. Sun, X. Chao, R. Sur, C. Goldenstein, J. Jeffries, and R. Hanson, "Analysis of calibration-free wavelength-scanned wavelength modulation spectroscopy for practical gas sensing using tunable diode lasers," *Measurement Science and Technology*, vol. 24, no. 12, p. 125203, 2013.
- [83] M. Dentan and B. de Cremoux, "Numerical simulation of the nonlinear response of a pin photodiode under high illumination," *Journal of Lightwave Technology*, vol. 8, no. 8, pp. 1137–1144, 1990.
- [84] Sensirion, "Sht31-smart-gadget." <https://sensirion.com/products/catalog/SHT31-Smart-Gadget/>, 2023.
- [85] C. Liu, S.-A. Tsekenis, N. Polydorides, and H. McCann, "Toward customized spatial resolution in tdlas tomography," *IEEE Sensors Journal*, vol. 19, no. 5, pp. 1748–1755, 2018.
- [86] J. Xia, G. Enemali, R. Zhang, Y. Fu, H. McCann, B. Zhou, and C. Liu, "Fpga-accelerated distributed sensing system for real-time industrial laser absorption spectroscopy tomography at kilo-hertz," *IEEE Transactions on Industrial Informatics*, 2023.
- [87] U. Ahmed, F. Ali, and I. Jennions, "A review of aircraft auxiliary power unit faults, diagnostics and acoustic measurements," *Progress in Aerospace Sciences*, vol. 124, p. 100721, 2021.
- [88] K. S. Ng, D. Farooq, and A. Yang, "Global biorenewable development strategies for sustainable aviation fuel production," *Renewable and Sustainable Energy Reviews*, vol. 150, p. 111502, 2021.

- [89] W. Zhang, D. J. Webb, L. Lao, D. Hammond, M. Carpenter, and C. Williams, "Water content detection in aviation fuel by using pmma based optical fiber grating," *Sensors and Actuators B: Chemical*, vol. 282, pp. 774–779, 2019.
- [90] S. Manigandan, A. Atabani, V. K. Ponnusamy, and P. Gunasekar, "Impact of additives in jet-a fuel blends on combustion, emission and exergetic analysis using a micro-gas turbine engine," *Fuel*, vol. 276, p. 118104, 2020.
- [91] L. Liu, Q. Guo, L. Wang, and D. Liu, "In-situ remaining useful life prediction of aircraft auxiliary power unit based on quantitative analysis of on-wing sensing data," *Advances in Mechanical Engineering*, vol. 12, no. 3, p. 1687814020911475, 2020.
- [92] R. Otero Jr, K. T. Lowe, W. F. Ng, L. Ma, and C.-Y. Kim, "Nonintrusive gas-turbine engine-exhaust characterization using acoustic measurements," *Journal of Propulsion and Power*, vol. 34, no. 3, pp. 730–738, 2018.
- [93] Honeywell, "131 Series APUs." <https://aerospace.honeywell.com/us/en/products-and-services/product/hardware-and-systems/auxiliary-power-units/131-series-apus>, 2023.
- [94] N. A. Malarich and G. B. Rieker, "Resolving nonuniform temperature distributions with single-beam absorption spectroscopy. part i: Theoretical capabilities and limitations," *Journal of Quantitative Spectroscopy and Radiative Transfer*, vol. 260, p. 107455, 2021.
- [95] Z. Wang, T. Kamimoto, Y. Deguchi, W. Zhou, J. Yan, K. Tainaka, K. Tanno, H. Watanabe, and R. Kurose, "Two dimensional temperature measurement characteristics in pulverized coal combustion field by computed tomography-tunable diode laser absorption spectroscopy," *Applied Thermal Engineering*, vol. 171, p. 115066, 2020.
- [96] S.-A. Tsekenis, K. G. Ramaswamy, N. Tait, Y. Hardalupas, A. Taylor, and H. McCann, "Chemical species tomographic imaging of the vapour fuel distribution in a compression-ignition engine," *International Journal of Engine Research*, vol. 19, no. 7, pp. 718–731, 2018.
- [97] H. Wang, L. Tang, and Z. Cao, "An image reconstruction algorithm based on total variation with adaptive mesh refinement for ect," *Flow Measurement and Instrumentation*, vol. 18, no. 5-6, pp. 262–267, 2007.

- [98] M. Molinari, S. Cox, B. Blott, and G. J. Daniell, "Adaptive mesh refinement techniques for electrical impedance tomography," *Physiological Measurement*, vol. 22, no. 1, p. 91, 2001.
- [99] M. P. Wood and K. B. Ozanyan, "Simultaneous temperature, concentration, and pressure imaging of water vapor in a turbine engine," *IEEE Sensors Journal*, vol. 15, no. 1, pp. 545–551, 2014.
- [100] S. J. Grauer, P. J. Hadwin, T. A. Sipkens, and K. J. Daun, "Measurement-based meshing, basis selection, and prior assignment in chemical species tomography," *Optics express*, vol. 25, no. 21, pp. 25135–25148, 2017.
- [101] Y. Jiang, J. Si, R. Zhang, G. Enemali, B. Zhou, H. McCann, and C. Liu, "Cstnet: A dual-branch convolutional neural network for imaging of reactive flows using chemical species tomography," *IEEE Transactions on Neural Networks and Learning Systems*, 2022.
- [102] S. Tsekenis, N. Tait, and H. McCann, "Spatially resolved and observer-free experimental quantification of spatial resolution in tomographic images," *Review of Scientific Instruments*, vol. 86, no. 3, p. 035104, 2015.
- [103] C. Liu, L. Xu, Z. Cao, and H. McCann, "Reconstruction of axisymmetric temperature and gas concentration distributions by combining fan-beam tdlas with onion-peeling deconvolution," *IEEE Transactions on Instrumentation and Measurement*, vol. 63, no. 12, pp. 3067–3075, 2014.
- [104] N. Polydorides, A. Tsekenis, E. Fisher, A. Chighine, H. McCann, L. Dimiccoli, P. Wright, M. Lengden, T. Benoy, D. Wilson, *et al.*, "Constrained models for optical absorption tomography," *Applied optics*, vol. 57, no. 7, pp. B1–B9, 2018.
- [105] N. Li and C. Weng, "Modified adaptive algebraic tomographic reconstruction of gas distribution from incomplete projection by a two-wavelength absorption scheme," *Chinese Optics Letters*, vol. 9, no. 6, p. 061201, 2011.
- [106] K. McGrattan, S. Hostikka, R. McDermott, J. Floyd, C. Weinschenk, and K. Overholt, "Fire dynamics simulator users guide nist special publication 1019," 2013.
- [107] S. J. Grauer, J. Emmert, S. T. Sanders, S. Wagner, and K. J. Daun, "Multiparameter gas sensing with linear hyperspectral absorption tomography," *Measurement Science and Technology*, vol. 30, no. 10, p. 105401, 2019.